RUMBLE STRIP DESIGN ANALYSIS TO CONTRIBUTE TO LOW EXTERIOR NOISE USING FINITE ELEMENT MODELING

Final Report

PROJECT SPR 829

Oregon Department of Transportation

RUMBLE STRIP DESIGN ANALYSIS TO CONTRIBUTE TO LOW EXTERIOR NOISE USING FINITE ELEMENT MODELING

Final Report

PROJECT SPR 829

by

Jinta Zheng
Yue Zhang

for

Oregon Department of Transportation
Research Section
555 13th Street NE, Suite 1
Salem OR 97301

and

Federal Highway Administration
1200 New Jersey Avenue SE
Washington, DC 20590

August 2022

Technical Report Documentation Page

1. Report No. FHWA-OR-RD-22-14	2. Government Accession No.	3. Recipient’s Catalog No.

4. Title and Subtitle Rumble Strip Design Analysis to Contribute to Low Exterior Noise Using Finite Element Modeling	5. Report Date August 2022
	6. Performing Organization Code
7. Author(s) Jinta Zheng, 0000-0003-1405-9479 Yue Zhang, 0000-0002-8467-2781	8. Performing Organization Report No.
9. Performing Organization Name and Address Oregon Department of Transportation Research Section 555 13th Street NE, Suite 1 Salem, OR 97301	10. Work Unit No. (TRAIS)
	11. Contract or Grant No.
12. Sponsoring Agency Name and Address Oregon Dept. of Transportation Research Section 555 13th Street NE, Suite 1 Salem, OR 97301 Federal Highway Admin. 1200 New Jersey Avenue SE Washington, DC 20590	13. Type of Report and Period Covered Final Report
	14. Sponsoring Agency Code

15. Supplementary Notes

16. Abstract:

Optimal rumble strips/stripes are critical to ensure traffic safety and simultaneously avoid disturbance to the surrounding environment. In this project, we have utilized a commercial Finite Element modeling tool to calculate the amount of noise in the tires while rolling over the rumble strips. The sound level is determined within the tire cavity. We have evaluated three types of designs: conventional, sinusoidal, and sawtooth. In total, we have simulated 19 conventional designs, 21 sinusoidal designs, and 6 sawtooth designs at 3 varying vehicle speeds for a passenger car and a truck tire. We have observed that the sinusoidal designs produced lower sound outputs than the conventional designs, and the sawtooth designs with a longer wavelength produced similar sound outputs to a sinusoidal design at the same depth. Furthermore, we have developed a non-zero angle of landing for different conventional and sinusoidal designs. Overall, our numerical simulations produced expected trends in the sound outputs for different rumble strip dimensions. Furthermore, when a chosen sound output level is determined, a specific dimension can be found among the simulated cases to guide the construction.

17. Key Words Finite Element Method, Exterior noise, Rumble strips/stripes	18. Distribution Statement Copies available from NTIS, and online at www.oregon.gov/ODOT/TD/TP_RES/

19. Security Classification (of this report) Unclassified	20. Security Classification (of this page) Unclassified	21. No. of Pages 110	22. Price

Technical Report Form DOT F 1700.7 (8-72) Reproduction of completed page authorized Printed on recycled paper

SI* (MODERN METRIC) CONVERSION FACTORS

APPROXIMATE CONVERSIONS TO SI UNITS					APPROXIMATE CONVERSIONS FROM SI UNITS				
Symbol	When You Know	Multiply By	To Find	Symbol	Symbol	When You Know	Multiply By	To Find	Symbol
		LENGTH					**LENGTH**		
in	inches	25.4	millimeters	mm	mm	millimeters	0.039	inches	in
ft	feet	0.305	meters	m	m	meters	3.28	feet	ft
yd	yards	0.914	meters	m	m	meters	1.09	yards	yd
mi	miles	1.61	kilometers	km	km	kilometers	0.621	miles	mi
		AREA					**AREA**		
in^2	square inches	645.2	millimeters squared	mm^2	mm^2	millimeters squared	0.0016	square inches	in^2
ft^2	square feet	0.093	meters squared	m^2	m^2	meters squared	10.764	square feet	ft^2
yd^2	square yards	0.836	meters squared	m^2	m^2	meters squared	1.196	square yards	yd^2
ac	acres	0.405	hectares	ha	ha	hectares	2.47	acres	ac
mi^2	square miles	2.59	kilometers squared	km^2	km^2	kilometers squared	0.386	square miles	mi^2
		VOLUME					**VOLUME**		
fl oz	fluid ounces	29.57	milliliters	ml	ml	milliliters	0.034	fluid ounces	fl oz
gal	gallons	3.785	liters	L	L	liters	0.264	gallons	gal
ft^3	cubic feet	0.028	meters cubed	m^3	m^3	meters cubed	35.315	cubic feet	ft^3
yd^3	cubic yards	0.765	meters cubed	m^3	m^3	meters cubed	1.308	cubic yards	yd^3
~NOTE: Volumes greater than 1000 L shall be shown in m^3.									
		MASS					**MASS**		
oz	ounces	28.35	grams	g	g	grams	0.035	ounces	oz
lb	pounds	0.454	kilograms	kg	kg	kilograms	2.205	pounds	lb
T	short tons (2000 lb)	0.907	megagrams	Mg	Mg	megagrams	1.102	short tons (2000 lb)	T
		TEMPERATURE (exact)					**TEMPERATURE (exact)**		
°F	Fahrenheit	(F-32)/1.8	Celsius	°C	°C	Celsius	1.8C+32	Fahrenheit	°F

*SI is the symbol for the International System of Measurement

ACKNOWLEDGEMENTS

We would like to thank the Technical Advisory Committee: Xiugang Li, Michael Kimlinger, Frank Belleque, Brendan Baggett, Natalie Liljenwall, Daniel Burgin and Nick Fortey for their guidance. Xiugang Li of ODOT Research Section managed this project.

We also would like to thank Jon Lazarus (Research Coordinator) for his guidance on designing the project and on developing the literature survey on the existing roadside measurements. In addition, we wish to thank Kira Glover-Cutter (Research Coordinator) for her support to start the project.

Lastly, we thank Zixuan Feng, a graduate student at Oregon State University for his contribution to Appendix A of this report.

DISCLAIMER

TABLE OF CONTENTS

LIST OF TABLES

LIST OF FIGURES

1.0 INTRODUCTION

Milled rumble strips/stripes are effective devices to alert distracted and drowsy drivers through in-cabin sound and vibration. There are two kinds of rumble strips/stripes depending on the placement on the pavement: centerline and shoulder. In addition, when the pavement marking is placed throughout the line of the rumble strip as shown in the left image of Figure 1.1 (A: Spacing (conventional)/wavelength (sinusoidal); B: Width (conventional); C: Length; D: Depth; E: Wavelength (sinusoidal)), in which dimensions of the strips are defined, it becomes a rumble stripe. National Cooperative Highway Research Program in 2009 reported that centerline rumble strips/stripes could provide crash reduction statistically from 40 to 60 percent on urban two-lane roads and 9 to 44 percent on rural two-lane roads, and shoulder rumble strips/stripes could provide crash reduction statistically from 13 to 18 percent on urban freeways, 11 to 16 percent on rural freeways and 15 to 29 percent on rural two-lane roads (Torbic et al., 2009). Federal Highway Administration in 2019 reported that centerline rumble strips could provide crash reduction at 64 percent on urban two-lane roads and 45 percent on rural two-lane roads, and shoulder rumble strips could provide crash reduction at 36 percent on rural two-lane roads and 17 percent on rural freeways (FHWA, 2019).

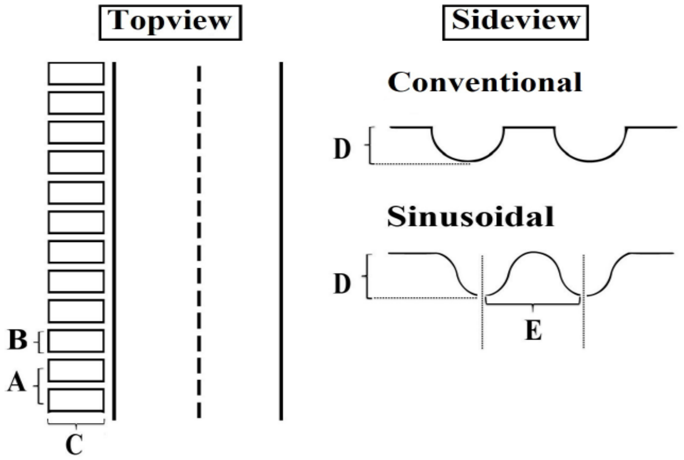

Figure 1.1: The geometric dimension of rumble strips (Torbic et al., 2009; Donavan and Buehler, 2018).

However, high magnitude interior acoustic and tactile signals (the vibration when the car rolls across rumble strips) from the rumble strips/stripes can cause overreactions or discomfort of the drivers (Fitzpatrick, 2000; Bahar et al., 2001; Nadeau, 2009; Makarla, 2009; Smets et al., 2010; Terhaar and Braslau, 2015; Tufuor et al., 2017; Ning et al., 2018). Furthermore, Soares et al. have stated that traffic noise is one of the most concerning environmental noises that impact human health (Soares et al., 2017), and is a potential source of increase in health issues for nearby residences. Some complaints against the traffic noise (exterior noise) are established by the residents as the growing road network in the U.S. puts rumble strips/stripes installation close to some residential neighborhoods (SAE, 2000; Torbic et al., 2009; Mathew et al., 2018; Donavan and Buehler, 2018). There is also reporting on nearby wildlife being disturbed (Torbic et al., 2009; Rys et al., 2010; Donavan and Buehler, 2018).

An increased amount of research is seen to optimize designs of rumble strips/stripes to reduce exterior noise levels while maintaining the desired level of interior acoustics and tactile signal. One of such recent efforts supported by Oregon Department of Transportation is SPR800 by Hurwitz et al. (2019), where interior and exterior acoustic levels over conventional and sinusoidal patterns were measured with microphone devices. Results from this report subsequently enabled two other publications: Horne et al. (2019 and 2020). To develop further understanding on how the exterior sounds are created by the tires so that optimization over existing rumble strip designs and generation of new designs can be achieved, we use numerical modeling approaches that can reveal the underlying Physics. We conduct simulation-based FEM (Finite Element Method) modeling, statistical data analysis, and data visualization to detect the correlations among geometrical dimensions of the rumble strips, vehicle types, and vehicle speeds using the acoustic outputs in the tires.

1.1 OUR METHODOLOGY

We first survey existing reports on roadside measurements for interior and exterior sound outputs over the rumble strips/tripes and document some of the findings in Appendix A. This survey provides information on some conclusions and limitations from the measurements. Then we conduct a survey over related work on numerical modeling and document some of the findings and applications in Appendix B. To leverage on the current advances in numerical modeling, we utilize a commercial software, SIMULIA by the Dassault System that is widely accepted in automotive industries (Kelsey, 2000). We study two different tire types: passenger car tire and truck tire due to the differences in their geometric dimension, polymer material rigidity, and the use of reinforcing inserts such as plys and belts. Furthermore, we include comparisons among numerical results of the landing angle of the tires on the rumble strips. As the tires land on the rumble strips at an angle in practice, we compare the effect of the tire rolling at zero-degree and 10 degrees, respectively. Only the zero-degree landing angle, i.e., parallel with the strips has been included in roadside measurements due to driver safety reasons; however, typically the tires land on and exit from the rumble strips at an angle. We have chosen 10 degrees as a numerical example here. Different angles should be included to conduct a detailed numerical study in the future. In addition, vehicle speeds affect the pavement noise level. We quantify the amount of change in acoustic responses from tire rolling for vehicle speeds at respectively 45 mph, 55 mph, and 65 mph, which are speeds chosen by the Oregon Department of Transportation and chosen in some of the literature that we have surveyed.

Concerning the rumble strip designs, we have studied three families: conventional, sinusoidal, and sawtooth. We selected conventional and sinusoidal rumble strip designs with dimensions that are used in the roadside measurements by either the California Department of Transportation (CalTrans) or the Oregon State Department of Transportation (ODOT). The sawtooth design is a new design introduced to ODOT by Dr. Zhang, the faculty member on the project. Existing conventional and sinusoidal designs are symmetrical along the tire rolling direction while the sawtooth groove has an asymmetric groove profile. We evaluate and compare the performances of these designs. Furthermore, we only focus on shoulder rumble strips in this report.

Figure 1.2 shows the flow of our simulation pipeline. There are five key steps enumerated in the middle column and the intermediate results from each step are visualized in the left column. The first step is the generation of the tires and the rumble strips through digitizing the geometries using published dimensions and material parameters. The second step is to set up the static contact between the tires and the rumble strips. The inflation pressures of the tires influence the final acoustic output and are estimated from general descriptions of vehicle weights. The third step is to set the tires into rolling. We have adopted steady state rolling which assumes the vehicles driving at a constant speed. This is an accepted baseline model to differentiate the performances of the rumble strips. A dynamic model is needed to further approximate real-life driving. The fourth and the fifth steps are developed to calculate the acoustic output, the Sound Pressure Level (SPL). These acoustic levels span over a range of frequencies. We have focused on frequencies between 0 Hz and 250 Hz as this range contains the most noticeable noises (An et al., 2017). Moreover, we select some representative locations in the tires and on the rumble strips and accumulate the outputs at these locations to approximate the overall acoustic outputs. The final values are in A-weighted decibels as what's done in (Donavan and Buehler, 2018). This numerical scheme involves complicated contact between the tire and rumble strip; thus requires fine enough resolution that incurs computation overhead.

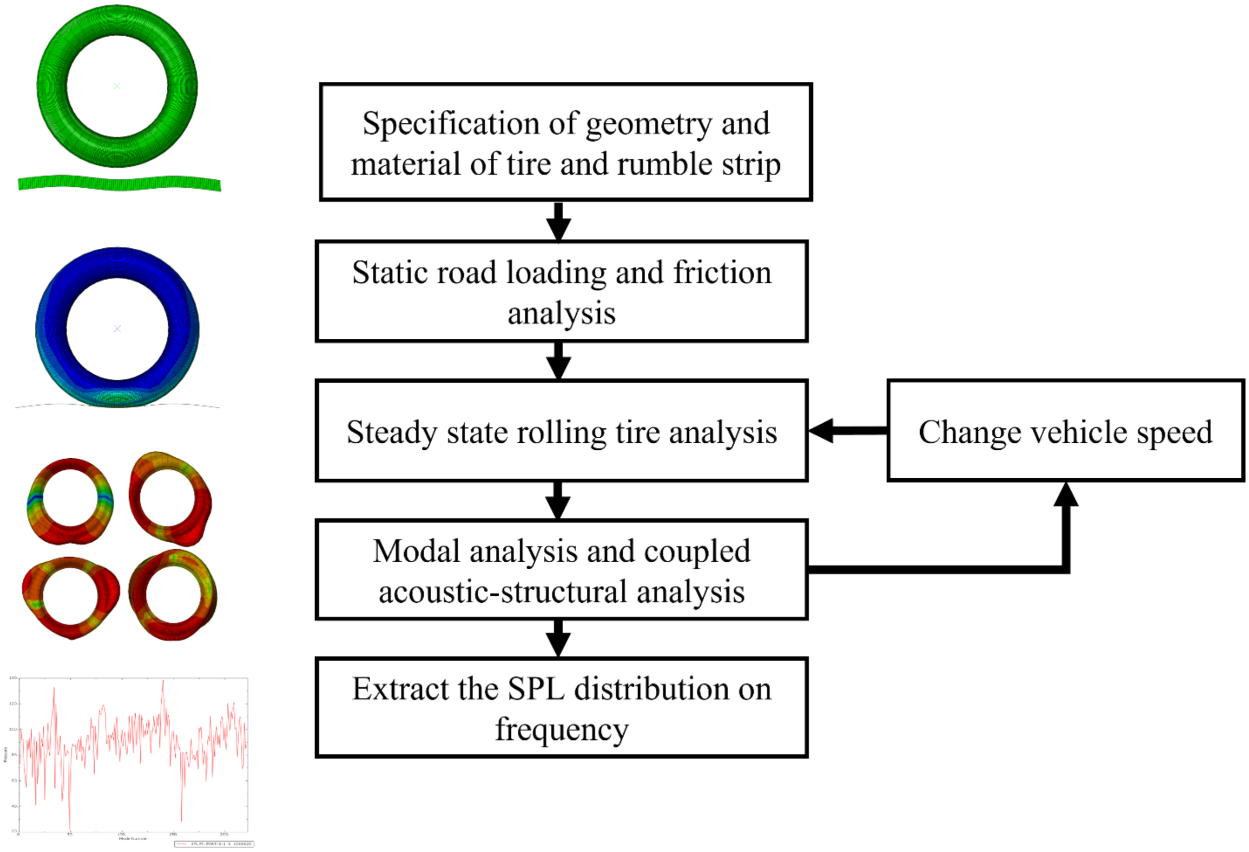

Figure 1.2: The flow of our simulation pipeline.

To verify our results, we compare our acoustic outputs to existing published roadside measurements. We match the trends from our calculations to those in CalTrans/CTHWANP-RT-18-365.01.2 in (Donavan and Buehler, 2018) and ODOT/SPR800 in (Hurwitz et al., 2019). To compare the performance of the different rumble strip designs, we create visualizations that rank the different designs using the tire SPL outputs to facilitate dimension selection in practice.

1.2 OUR OBSERVATIONS

Given a set of rumble strip designs with different geometric dimensions (depths, widths, and wavelengths of rumble strips), we analyze the SPL responses from each rumble strip dimension. We have observed that varying the depth and wavelength of the rumble strip designs changes the SPL responses. Such changes are also documented in roadside measurements that have been published.

Our simulated results agree in general with roadside measurements. Specifically,

1. Comparing to CalTrans/CTHWANP-RT-18-365.01.2, the SPL values from our numerical simulations are within the same range as what was reported. Furthermore, we observe that the first two peaks occur at similar frequency values to those reported.

2. Comparing to ODOT/SPR800, we also observe that conventional designs have a higher SPL response than sinusoidal designs, and the truck tire SPL is higher than the passenger car tire SPL. Our calculated values are higher than those reported as we measure in the tires and the roadside measurements are at a distance away.

In addition, we used existing dimensions published in the ODOT/TLM and ODOT/SPR800 reports to build our evaluation studies where we made variations over depths and wavelengths for comparison. Over the forty design dimensions with respect to two tire types and three vehicle speeds, we observe that

1. For conventional designs, the SPL increases with increasing depth and increasing speed for both the passenger and the truck tires, and the SPL decreases with increasing width in general. For the passenger car tire, there is one exception at the smallest width value at the deeper depth. For the truck tire, the overall differences in the SPL values are smaller than those for the passenger car tires. The smallest two width values at the deeper groove again were exceptions to the expected trends. Our sampling scheme over the grooves is likely the cause as only 4 positions were used to represent these deep grooves. Among the dimensions simulated, the design with a depth of 0.2628 inches and a spacing of 12 inches has the lowest SPL outputs.

2. For sinusoidal designs, the SPL increases with increasing depth and increasing speed, and decreases with increasing wavelength. In addition, the design with a depth of 0.375 inches and a wavelength of 22 inches has the lowest SPL output among sinusoidal designs that we simulated.

3. For the sawtooth designs, which have an asymmetric side profile, we propose 2 variations, and each design includes three different wavelengths. By comparing the results to one representative sinusoidal design dimension, we observe that a longer

wavelength of the sawtooth design at the same depth and length as the sinusoidal design can produce similar levels of SPL responses.

Moreover, we evaluated the angle of landing effect for a reduced number of conventional and sinusoidal designs

1. For our angle of landing results, out of the 96 cases, 86 cases show that the SPL of 10 degrees angle of landing is higher than that of the zero-degree. In addition, the SPL differences for the passenger car tire are higher than those for the truck tire.

2.0 TIRE AND RUMBLE STRIPS MODELING

We have chosen two contrasting tire types: passenger car and truck. We have purchased one passenger car tire and one truck tire from the vehicles that were used to measure both exterior and interior noise levels in ODOT/SPR800. We obtained cross sections of these tires by having the tires cut, made measurements of the thickness along with the tire profiles, and digitized the tires with meshes for numerical modeling.

We have modeled the tire materials using parameters published in the literature (Chae, 2006; Wang et al., 2010; Wang et al., 2011; Smith, M, 2016). However, these published parameters are just approximations to the materials that are used in the tires that we purchased. In this section, we list the material settings from the reference and the values we used in our simulations.

2.1 GEOMETRY MODELLING OF TIRES

We start with the mesh of the tire and then include an air cavity to be used in the coupled acoustic-structural analysis. The air cavity is the space that is enclosed by the interior surface of the tire and a cylindrical surface of the wheel hub. This air cavity is modeled with acoustic elements while the tire is modeled with the structural element. As the tire is deformed during each revolution, the air mesh needs to be updated seamlessly. The updated nodal locations are derived from adaptive remeshing. For modeling rumble strips, we digitize rumble strips with rigid elements.

In the following Table 2.1, we show the recommended element types used to discretize each component of the geometry (Smith, M, 2016).

Table 2.1: Element Type of the Tire Construction

Portion	Element types
Tread	CGAX4H, CGAX3H
Sidewall	CGAX4H
Belt	CGAX4H
Rebar belt	SFMGAX1
Rebar carcass	SFMGAX1
Rim	RAX2
Air	ACAX4

The different element types produce different degrees of freedom for the portion of the tires and the air. These degrees of freedom enable physics-based modeling. One component of the tire that constrains the movement is the metal cords that are under the treads, which are called the belts; and the textile cords that are next to the tire's inner surface, the plys. The belts and plys hold the tire together when rolling on the road. They are included individually as Rebar belt and Rebar carcass in Table 2.1. We show a schematic sketch of one-quarter of a tire cross-section in Figure 2.1. The gray cells are the acoustic material and the air, and the blue cells are the tire materials including the belts in red color. For the tire in Figure 2.1, the geometry and material parameters are obtained from the manuals (Smith, M, 2016). This tire is a simplified description of a Continental car tire, and the mesh is coarse. We have created much more refined meshing and included tread grooves for the tires that we purchased and simulated.

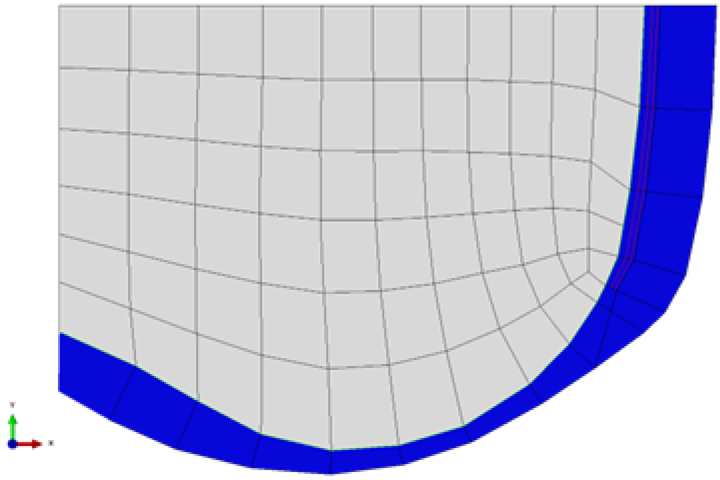

Figure 2.1: Meshing of the tire and air cross-section given in SIMULIA.

2.2 MATERIAL MODELLING OF TIRES

Table 2.2 shows the radius and vehicle weight information (total load on one tire) on the simulated passenger car and truck tires that we have simulated. The mesh refinement of these two tires is different due to the different construction and size.

Table 2.2: Names of the Passenger Car and Truck Tire Used

Tire Type	Radius (inch)	Weight (N)
Continental ContiProContact (215/55R/16, passenger car tire)	12.8	3300
BridgeStone M854 (385/65R/22.5, truck tire)	21.1	18000

The material properties are shown in Table 2.3 for the passenger car tire and Table 2.4 for the truck tire. The middle columns of these tables show the references that we used to extract the material properties. For the passenger car tire, we used most of the existing material descriptions from the SIMULIA tool and adjusted a few values to increase the stiffness as our tire is a stronger tire than the simplified Continental tire given in the tool. For the Bridgestone truck tire, we used the literature references listed in Table 2.4.

Table 2.3: Material Properties for the Passenger Car Tire

Material	Property (references)	Property (we used)
Tread	Hyperelastic, N=1, 1.0E+6 Density = 1100 kg/m3 Damping, Beta = 1.0E-8 (Smith, M, 2016)	Hyperelastic, N=1, 3.0E+6 Density = 1100 kg/m3 Damping, Beta = 1.0E-8
Sidewall	Hyperelastic, N=1, 1.0E+6 Density = 1100 kg/m3 Damping, Beta = 1.0E-8 (Smith, M, 2016)	Hyperelastic, N=1, 2.0E+6 Density = 1100 kg/m3 Damping, Beta = 1.0E-8
Rebar belt	Elastic, type=ISO, 1.72E+11, 0.3 Density = 5900 kg/m3 Rebar Layer 1, Orientation Angle = 70, Spacing = 0.00116 Rebar Layer 2, Orientation Angle = 110, Spacing = 0.00116 (Smith, M, 2016)	Hyperelastic, N=1, 3.0E+6 Density = 1100 kg/m3 Damping, Beta = 1.0E-8 Rebar Layer 1, Orientation Angle = 70, Spacing = 0.00116 Rebar Layer 2, Orientation Angle = 110, Spacing = 0.00116
Rebar carcass	Elastic, type=ISO, 9.87E+09, 0.3 Density = 1500 kg/m3 Rebar Layer 1, Orientation Angle = 0, Spacing = 0.001 (Smith, M, 2016)	Elastic, type=ISO, 9.87E+09, 0.3 Density = 1500 kg/m3 Rebar Layer 1, Orientation Angle = 0, Spacing = 0.001 (Smith, M, 2016)
Bead	Elastic, type=ISO, 3.45E+12, 0.2 Density = 5900 kg/m3 (Wang et al., 2011)	Elastic, type=ISO, 1.72E+11, 0.3 Density = 5900 kg/m3
Bead filler	Elastic, type=ISO, 1.2e+08, 0.49 Density = 1100 kg/m3 (Wang et al., 2010)	Elastic, type=ISO, 1.2e+09, 0.4 Density = 1500 kg/m3
Air	Bulk modulus = 426 kPa Density = 3.6 kg/m3 (Smith, M, 2016)	Bulk modulus = 426 kPa Density = 3.6 kg/m3 (Smith, M, 2016)

Table 2.4: Material Properties for the Truck Tire

Material	Property (references)	Property (we used)
Tread/Shoulder	Hyperelastic, MOONEY-RIVLINI 0.67e6, 2.46e6, 1e-05 Density = 628 kg/m3 (Chae, 2006)	Hyperelastic, MOONEY-RIVLINI 0.67e6, 2.46e6, 1e-05 Density = 628 kg/m3 (Chae, 2006)
Sidewall	Elastic, type=ISO, 3.92e+08, 0.3 Density = 655 kg/m3 (Chae, 2006)	Elastic, type=ISO, 3.92e+08, 0.3 Density = 655 kg/m3 (Chae, 2006)
Rebar belt	Elastic, type=ISO, 3.45E+12, 0.2 Density = 5900 kg/m3 (Wang et al., 2011) Rebar Layer 1, Orientation Angle = 70, Spacing = 0.00116 Rebar Layer 2, Orientation Angle = 110, Spacing = 0.00116 (Smith, M, 2016)	Elastic, type=ISO, 3.45E+12, 0.2 Density = 5900 kg/m3 (Wang et al., 2011) Rebar Layer 1, Orientation Angle = 70, Spacing = 0.00116 Rebar Layer 2, Orientation Angle = 110, Spacing = 0.00116 (Smith, M, 2016)
Rebar carcass	Elastic, type=ISO, 3.92e+08, 0.3 Density = 655 kg/m3 (Chae, 2006) Rebar Layer 1, Orientation Angle = 0, Spacing = 0.001 (Smith, M, 2016)	Elastic, type=ISO, 3.92e+08, 0.3 Density = 655 kg/m3 (Chae, 2006) Rebar Layer 1, Orientation Angle = 0, Spacing = 0.001 (Smith, M, 2016)
Rebar nylon	Elastic, type=ISO, 1.98e+08, 0.3 Density = 961 kg/m3 (Chae, 2006)	Rebar Layer 1, Orientation Angle = 120, Spacing = 0.00116
Bead	Elastic, type=ISO, 3.45E+12, 0.2 Density = Density = 5900 kg/m3 (Wang et al., 2011)	Elastic, type=ISO, 3.45E+12, 0.2 Density = Density = 5900 kg/m3 (Wang et al., 2011)
Bead filler	Hyperelastic, MOONEY-RIVLINI 0.392e6, 1.268e6, 1e-05 Density = 800 kg/m3 (Chae, 2006)	Hyperelastic, MOONEY-RIVLINI 0.392e6, 1.268e6, 1e-05 Density = 800 kg/m3 (Chae, 2006)
Air	Bulk modulus = 426 kPa Density = 3.6 kg/m3 (Smith, M, 2016)	Bulk modulus = 426 kPa Density = 3.6 kg/m3 (Smith, M, 2016)

To model the tire-pavement contact, each node on the tire surface is projected onto the road surface in the normal direction to enable contact modeling. In this case, the normal direction affects the convergence of the simulations. Figure 2.2 shows the displacement magnitude of the full three-dimensional tire model when pushed by the sinusoidal rumble strip. The pavement contact zone and the top of the tire have different displacements. The distribution of the displacement magnitude is shown with different colors, blue (low) vs. green (high).

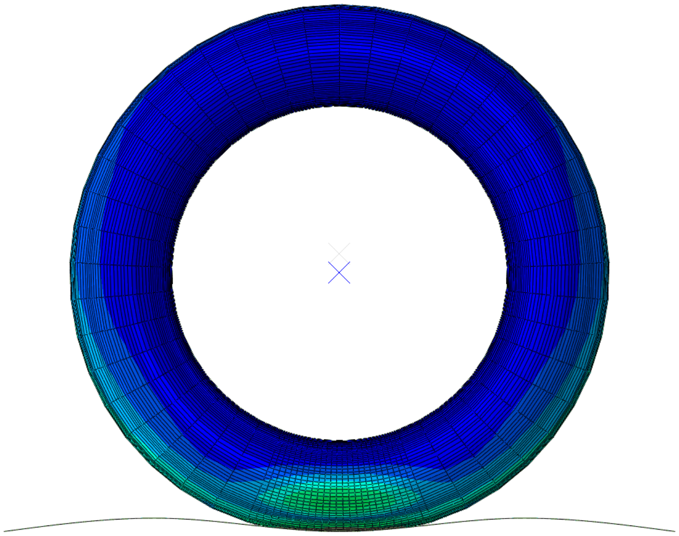

Figure 2.2: Deformation in the tire. The rumble strip is pushed up to the tire to create contact and cause deformation in the tire.

The interaction between the tire and the rumble strip is modeled by pushing the rumble strip to the tire. To demonstrate that the acoustic elements are sensitive to the push from the rumble strips, we show in Figure 2.3 the displacement magnitude of the full three-dimensional air cavity elements under inflation. The elements in green (high) are close to the tire inner liner and the ones in blue (low) are close to the rigid rim. The displacement of the acoustic elements gradually changes from high at the interface with the tire inner liner to low at the interface with the wheel hub.

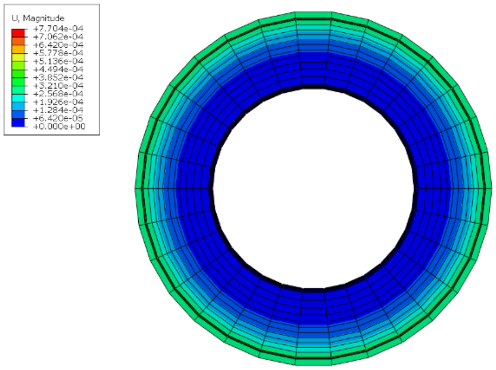

Figure 2.3: Displacement magnitudes of the air cavity inside the tire.

To extract the Sound Pressure Levels (SPL) from the air cavity, we first find the natural modes for the rolling tires. We choose the LANCZOS eigen solvers that have proven robustness in research and application domains. Each mode number corresponds to a fundamental frequency. We assume the air inside is rotating with the same angular velocity as the tire. Furthermore, we choose some sampling locations in the air and accumulate the SPL outputs at these locations to determine the overall output for the tires. Figure 2.4 shows a sampling position, a red-colored dot inside the air. We have chosen different numbers of these sample positions for the passenger and the truck tires used due to the difference in the tire sizes, thus the air volumes. At each position, the SPLs are calculated for each frequency and one example of this distribution is shown in Figure 2.5.

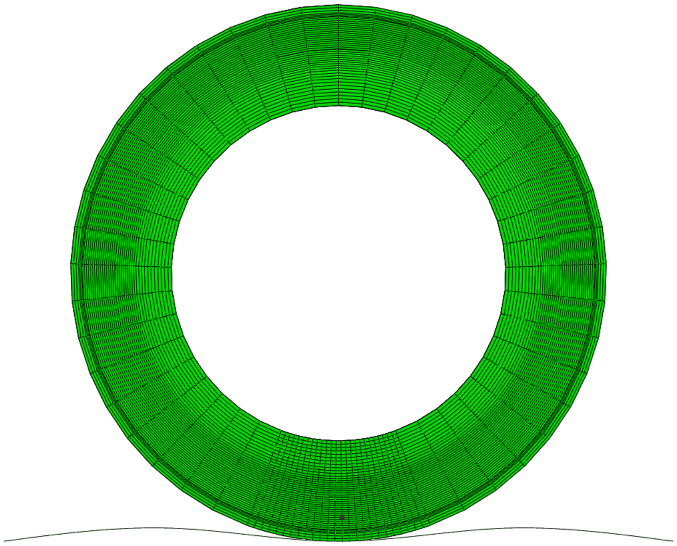

Figure 2.4: One sample position inside the air cavity to measure sound pressure levels.

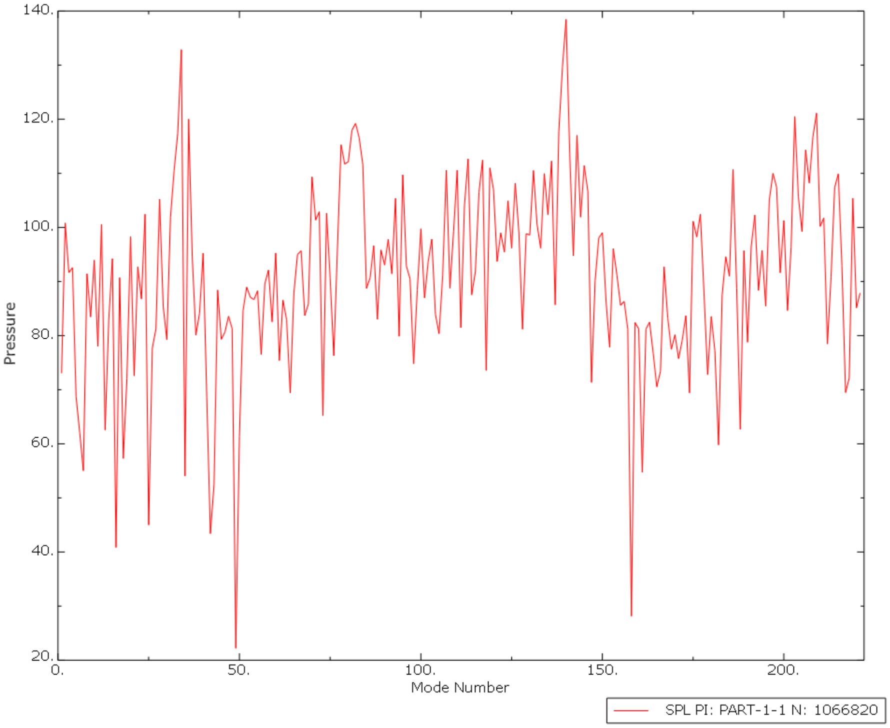

Figure 2.5: The SPL (dB) of the sampled position inside the air cavity.

2.3 RUMBLE STRIP DESIGNS

For the rumble strips, we vary the depth, wavelength, and length to compare the overall SPL. In this subsection, we show a 2D discretization and a side profile of each rumble strip design. Figure 2.6 shows the discretized version of a conventional rumble strip, and Figure 2.7 the sinusoidal rumble strip. For the asymmetric groove pattern, we have created two variations: one has a long climb and quick drop profile (Figure 2.8), and the other has a short climb and slow drop profile (Figure 2.9). The driver seat vibration generated by the asymmetric profile of sawtooth design along with vehicle modeling is not included in this study.

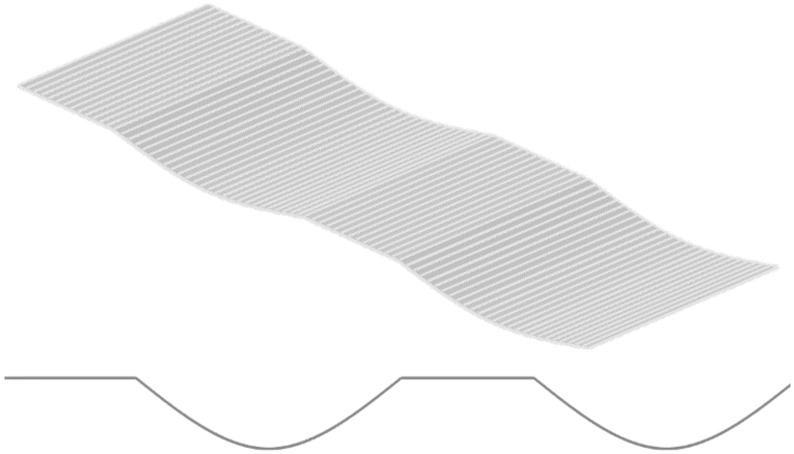

Figure 2.6: Conventional rumble strip.

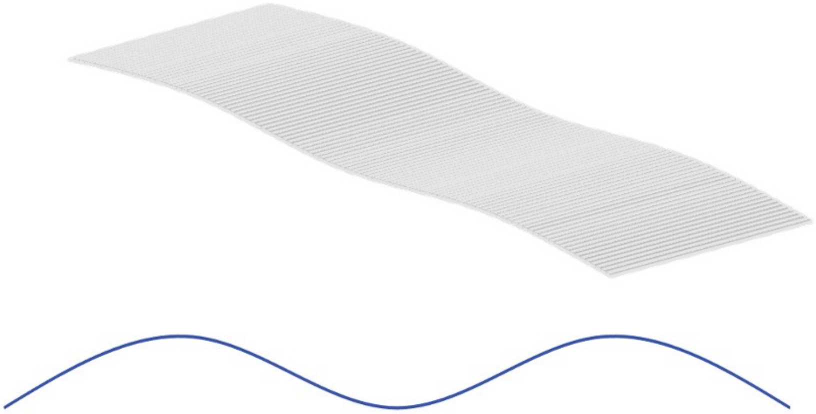

Figure 2.7: Sinusoidal rumble strip.

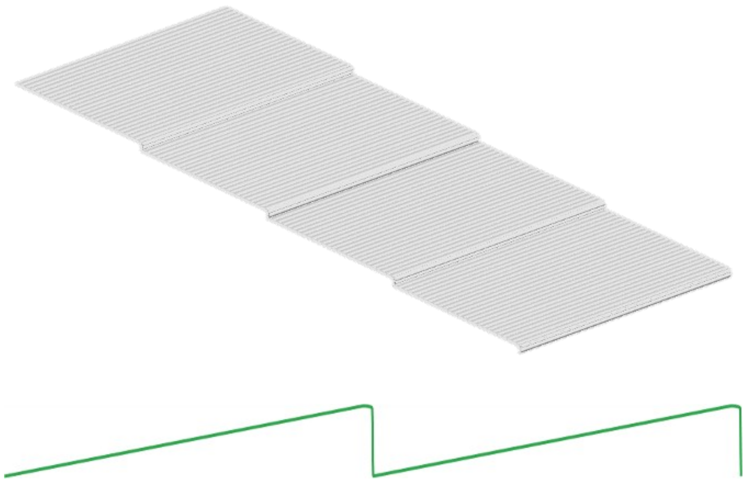

Figure 2.8: Sawtooth-long-climb-quick-drop rumble strip.

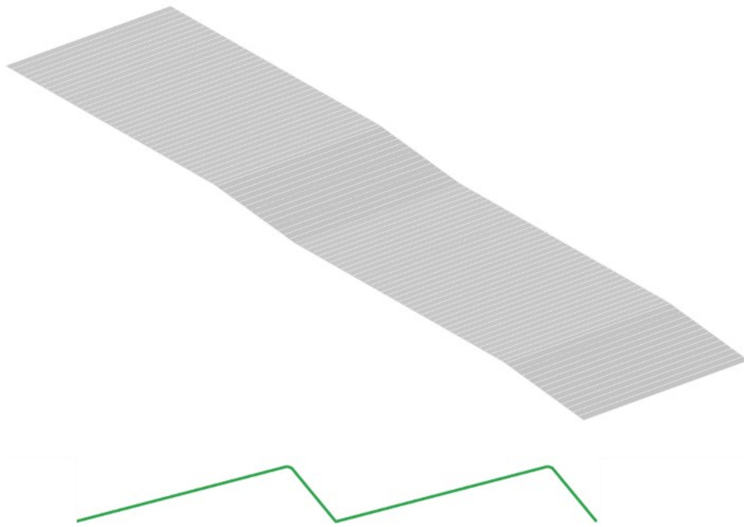

Figure 2.9: Sawtooth-short-climb-slow-drop rumble strip.

We have built over 276 scenarios by varying the rumble strip dimensions defined by ODOT (ODOT/TLM, 2018; ODOT/SPR800, 2019) to compare their performances. In total, we have simulated 19 conventional designs, 21 sinusoidal designs, and 6 sawtooth designs for three different vehicle speeds and two vehicle types.

3.0 SOUND MODELING

In this section, we present our scheme to calculate the final SPL output from each scenario, i.e., a tire rolling over a specific rumble strip dimension. To rank the effects of the different rumble strip designs and their dimensions, we assume the tires have traveled a fixed time period, i.e., 0.1 seconds as reported in (CalTrans/CTHWANP-RT-18-365.01.2, 2018). Instead of solving a dynamic rolling problem whose computation overhead is beyond the allocated resources for this project, we have chosen the steady state rolling for the tires and sampled the SPLs at a number of locations on the rumble strips. We sample the same number of locations on the rumble strips for all the designs. For each wavelength, the sample locations are evenly distributed.

3.1 CONTRIBUTIONS FROM RUMBLE STRIPS

The conventional and sinusoidal rumble strips are sampled for the half-length of the spacing or wavelength as these patterns have symmetric profiles. Figure 3.1, Figure 3.2, and Figure 3.3 show the sample locations that we have used for the conventional, sinusoidal, and sawtooth designs along with one spacing (conventional) or one wavelength (sinusoidal and sawtooth), respectively. We sample 7 locations for one conventional and sinusoidal design dimension in the two top drawings. For the sawtooth designs, we sample 14 locations along the tire rolling direction as shown in the two bottom drawings. These numbers of locations were chosen to best represent the geometries and at the same time not to incur high computation overhead.

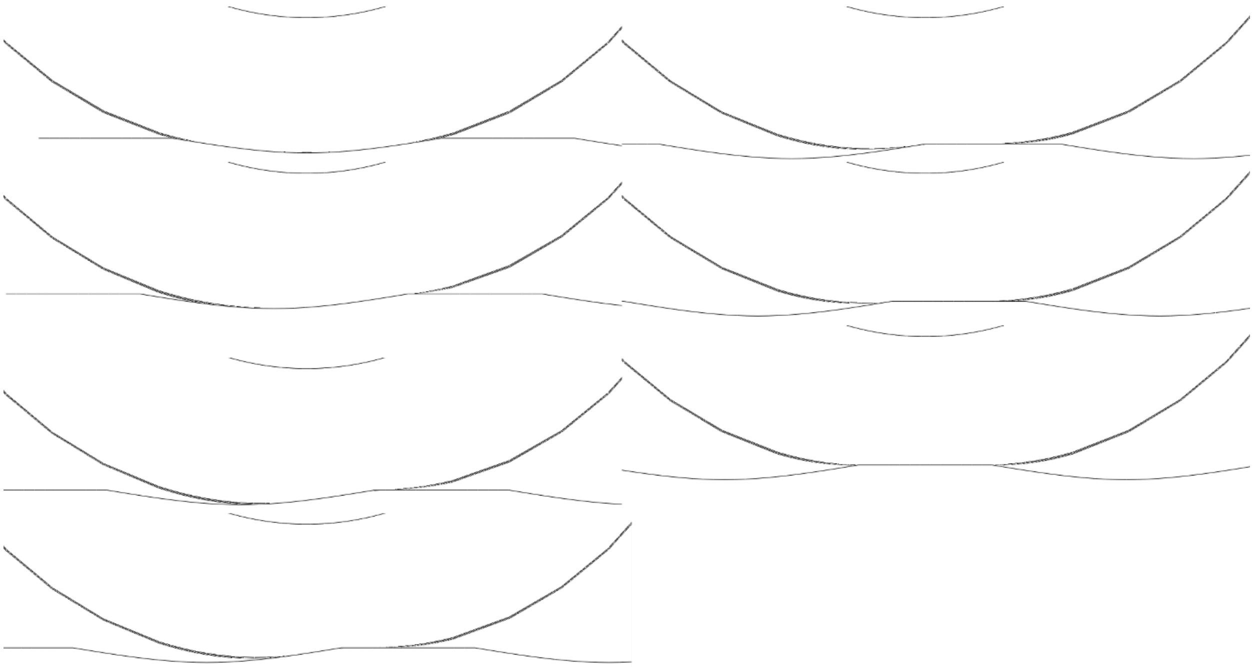

Figure 3.1: Sample locations shown on side profiles of one conventional design dimension.

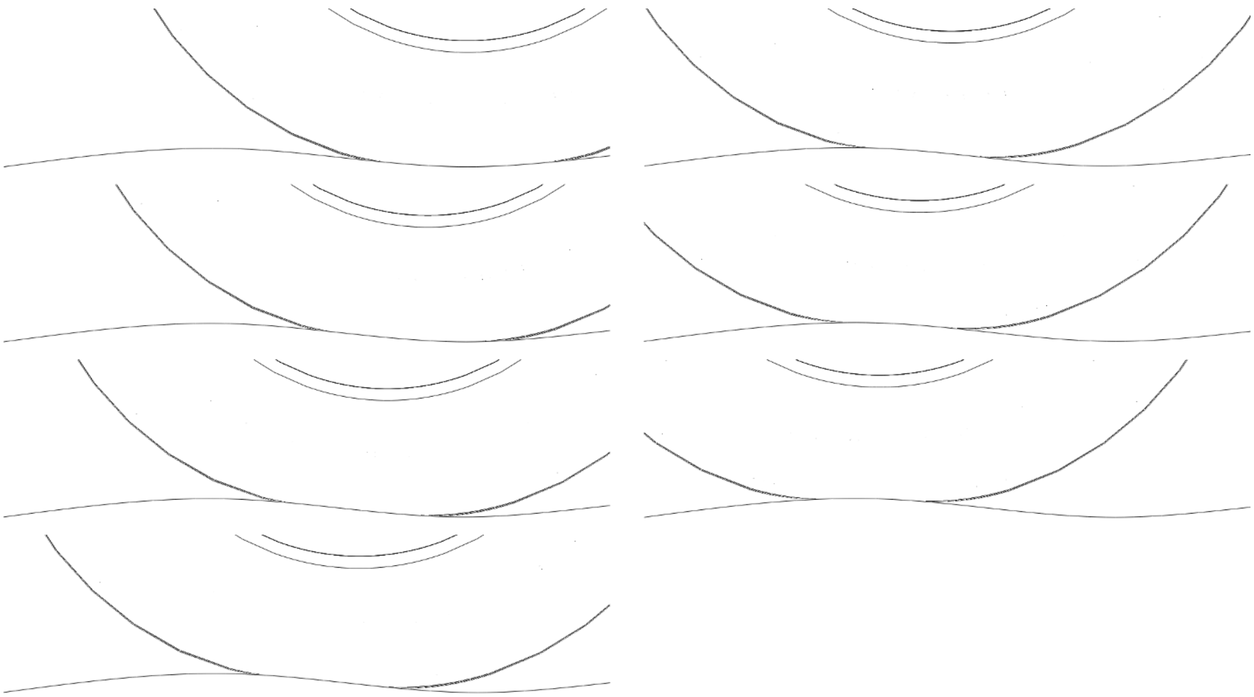

Figure 3.2: Sample locations shown on side profiles of one sinusoidal design dimension.

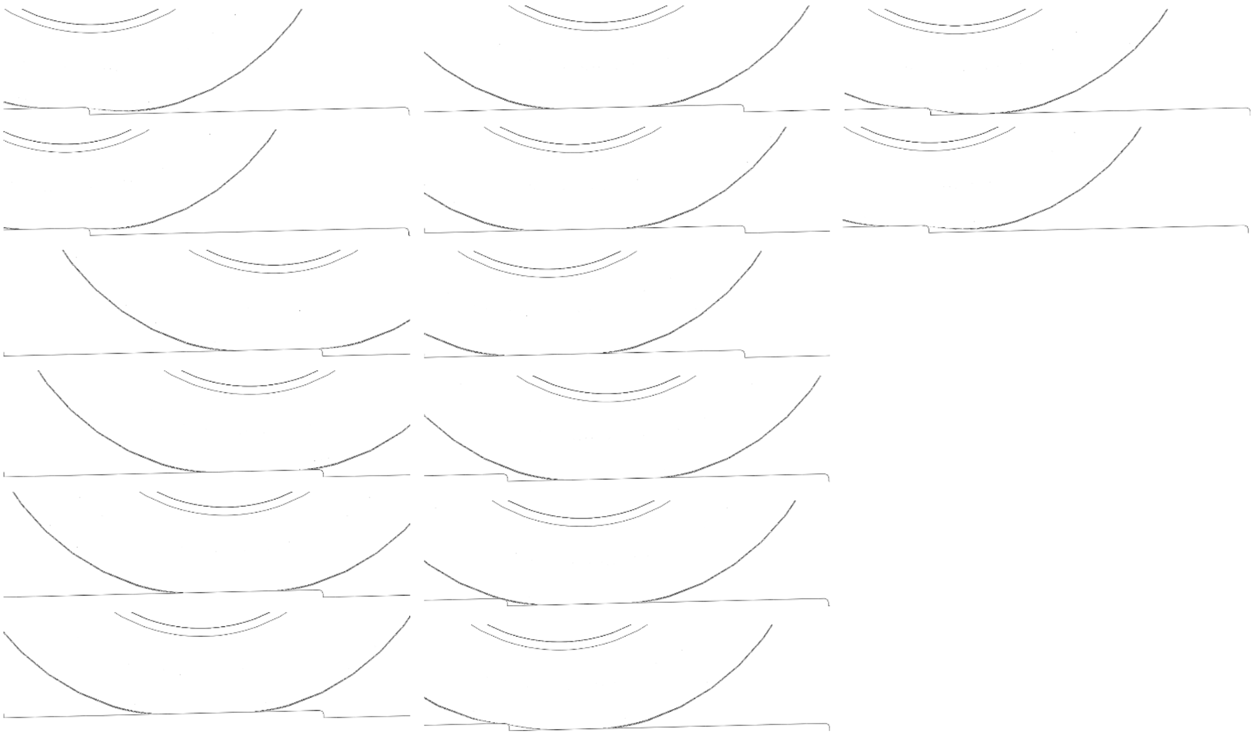

Figure 3.3: Sample locations shown on side profiles of sawtooth-long-climb-quick-drop.

For each rumble strip design, by sampling uniformly over the given pattern, we can ensure that the main features such as troughs, flat portions, and peaks are included in the tire-pavement contact modeling. Another scheme is to use one particular rumble strip design as a reference for sampling and sample the other designs at the same locations. We conjecture that the latter scheme would require many more sampling points to capture all features of each design. Due to the computation cost, we have chosen our fixed number of the sampling scheme. In future work, this number of samplings will be increased to more precisely represent the rumble strip geometries.

3.2 CONTRIBUTIONS FROM AIR INSIDE TIRE

At each location on the rumble strip, to calculate the contribution from the air volume inside the tires, we have chosen positions that have the highest SPL at each frequency. We first convert the SPL into A-weighting SPL for each frequency at each position. For each location $j = 1 \ldots P$ on the rumble strip, we have averaged the SPLs in each frequency band, $i = 1 \ldots n$, by equation (1), when the frequencies are close together. We use the log sum operation for noise source addition within each frequency band. We denote the SPL in each frequency band, i, at each location, j, on the rumble strip as $SPL_i(j)$. The total SPL at a location on the rumble strip is:

$$\boldsymbol{SPL}\,(\mathbf{j}) = \frac{\sum_{i=1}^{n} \boldsymbol{SPL_i(j)}}{\boldsymbol{n}}$$

(3-1)

Finally, for a tire rolling at the speed of s [meter/second] and rolling at the time of t [seconds] on the rumble strip with the wavelength/spacing of w [meters], the overall SPL of the rolling tire is calculated by the following equation (2):

$$\boldsymbol{SPL} = \mathbf{10}\,\boldsymbol{log_{10}}\left(\mathbf{10}^{\frac{\frac{\sum_{j=1}^{P} \boldsymbol{SPL}\,(\mathrm{j})}{\boldsymbol{P}} * \left(\frac{\boldsymbol{s*t}}{\boldsymbol{2*w}}\right)}{\mathbf{10}}}\right)$$

(3-2)

The same sampling positions and SPL calculation scheme are used for all the designs in our verification and sensitivity studies described in the next two sections.

4.0 VERIFICATION

We first verify our schemes by evaluating deformations in the tires on the rumble strips visually. When the peak points of the rumble strip designs push into the tire treads, we expect high stress and high displacement at the contact regions. When the grooves of the rumble strip design cup the tire treads, we expect low stress and low displacement in the tires that fall into the very center of the grooves. Visualizations of the stress and displacement are shown in Section 4.1. Then, we compare our simulated results to some roadside measurements reported in (CalTrans/CTHWANP-RT-18-365.01.2, 2018) and (ODOT/SPR800, 2019). In total, we compared two conventional and two sinusoidal designs for the passenger car tire; and one conventional and one sinusoidal design dimension for the truck tire. We have observed that our calculated sound levels are within the expected ranges and have similar trends as those reported in the roadside measurements. The details of our comparisons are in Section 4.2 and Section 4.3.

4.1 VISUAL VERIFICATION OF MAGNITUDES OF STRESSES AND DISPLACEMENTS

We present the visualizations of the Von Misses stress, a yield criterion, in Figure 4.1. We choose one representative dimension for each design pattern to create the visualization. The stress in the tire on the conventional design is in the top image, sinusoidal in the middle, and sawtooth at the bottom. We display the portion of the tire that is in contact with the rumble strips so that where the tire is flattened is in the view. We also add an inset, under the legend, to each image to show where the tire is on the rumble strip. We note that the stresses are distributed over the tires continuously as expected. The high stresses are near the contact areas with the rumble strips. Specifically for the conventional design, in the contact area, the color coding for the stress values is not symmetric as expected. The right portion is on the flat part of the rumble strip while the left is falling into the groove. For the sinusoidal design dimension, the color coding is symmetric, also as expected. For the sawtooth design dimension, we see some high stress values colored in red due to the pointy peaks in this design.

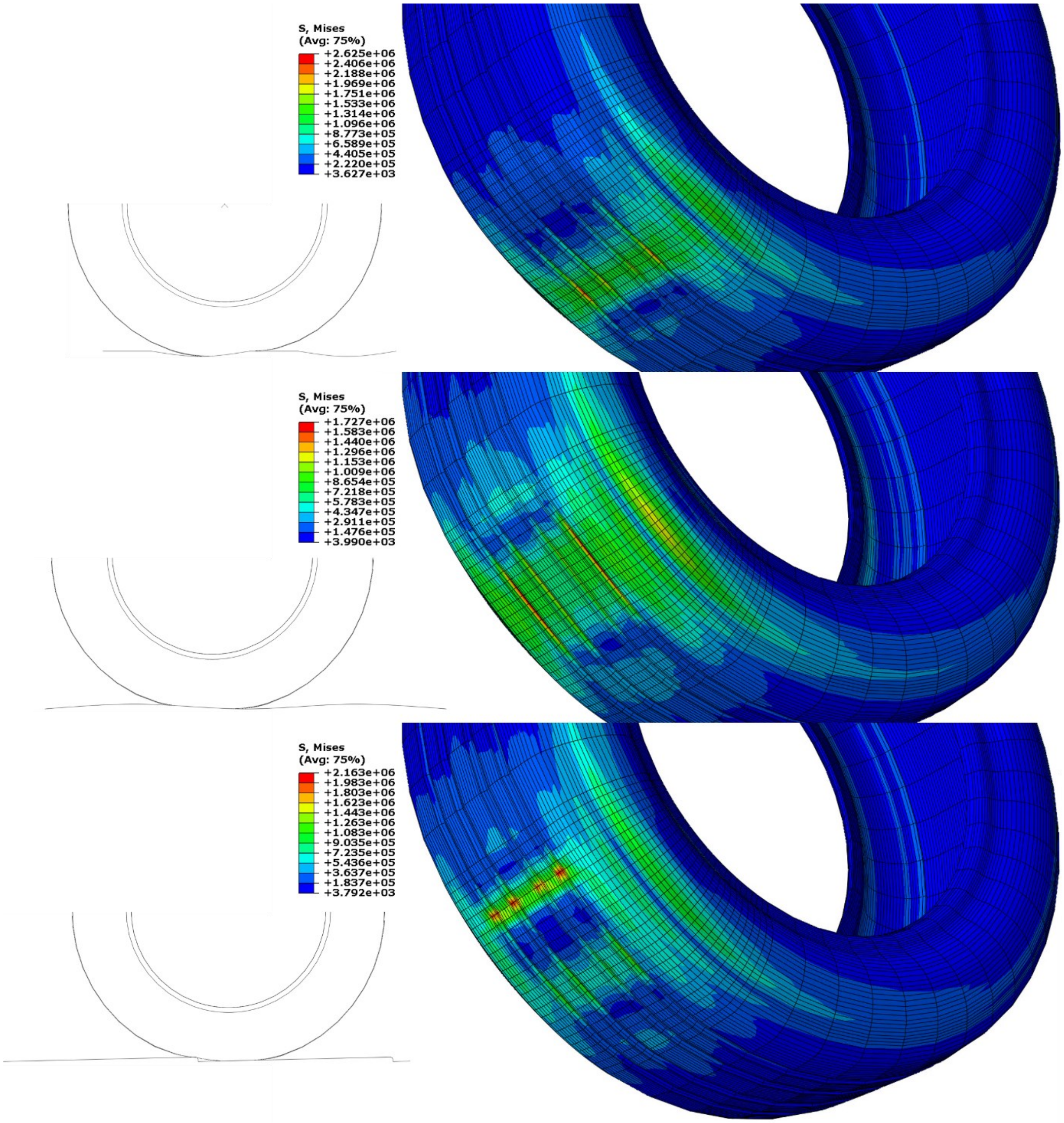

Figure 4.1: Von Mises Stress comparison. For the passenger car tire (tread and sidewall), Von Mises Stresses are shown for one conventional design (top), one sinusoidal design (middle), and one sawtooth-long-climb-quick-drop design (bottom).

These visualizations confirm the modeling is effective in capturing the features in the geometric profiles of the rumble strip designs. The different contact areas on the tread cause different stress responses in the tires, which in turn impose different displacements in the air cavity. These displacements produce different acoustic pressures.

In Figure 4.2, we only show the air elements, i.e., tire carcass and tread are removed from the view, to demonstrate the different displacement distributions for each rumble strip dimension.

For the conventional design, left image of this figure, there is a small rectangular shaped high displacement area (red) due to the overall contact with the rumble strip and the contact area in the tire tread is rectangular in general. The magnitude of the displacement falls off with increasing distance to the center of the contact area as expected. Moreover, there is an oblong shaped region at the tire shoulder that has medium high displacement values (yellowish green). This oblong shape also has a high magnitude value at its center and the magnitude drops off towards its boundary.

Comparing the high displacement regions (rectangular shape in red) in the tread contact area and the medium high displacement regions (oblong shape in yellowish green) in the tire shoulder area for all three rumble strip designs, we observe that the conventional design and the sinusoidal design have similar size of the high displacement region (red) while the sawtooth has the lowest size. The conventional design has the highest value among the three designs. The sawtooth design has the lowest values among the three designs. For the medium high displacement region (oblong shape in yellowish green), the conventional and sinusoidal designs have similar sizes and values while the sawtooth design has the smallest size and the lowest value.

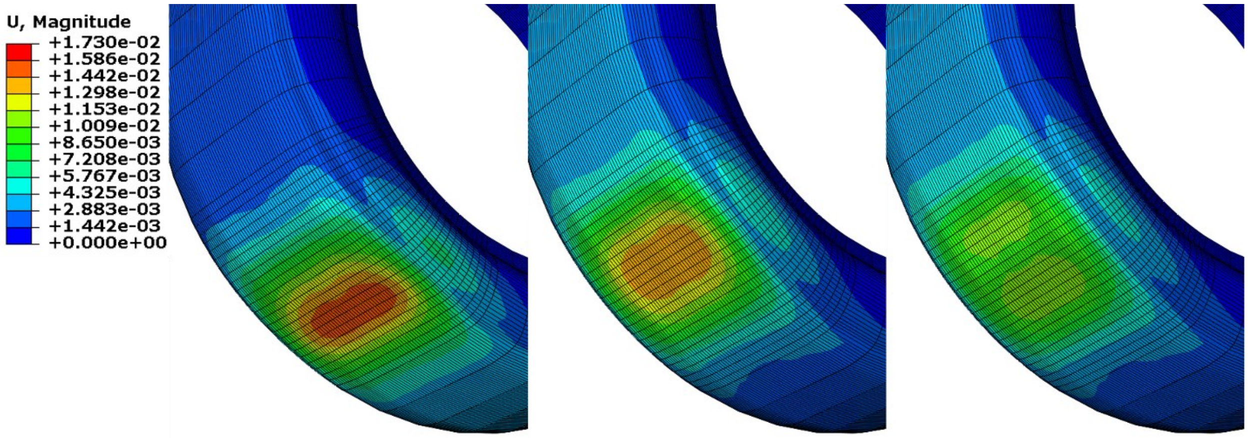

Figure 4.2: Displacement magnitude comparison. For the air cavity inside the passenger car tire, displacement magnitudes are shown for one conventional design (left), one sinusoidal design (middle), and one sawtooth-long-climb-quick-drop design (right).

These visualizations indicate that even though the sharp peaks in the rumble strips are no longer visible in the air cavity as the tire treads have absorbed these sharp stresses, the acoustic pressures are distributed non-uniformly near the tread contact areas. The sizes of the high and medium high displacement regions are different for these three designs. Knowing the sizes of these zones can potentially facilitate the creation of new rumble strip designs to reduce the high acoustic pressures generated from these high displacements.

4.2 VERIFICATION USING CALTRANS/CTHWANP-RT-18-365.01.2, 2018

In 2018, the California Department of Transportation conducted roadside measurements and investigated the noise response of different rumble strips (CalTrans/CTHWANP-RT-18-365.01.2). In their results, two dominant peaks of exterior noise levels over a range of frequencies are revealed. These two peaks are near 80 Hz and 160 Hz. These peaks are within the ranges that could cause noise complaints and could be created from the structural vibrations of the tires.

In their report, the authors took measurements at two different locations on the vehicles: the first one has a microphone next to the tire, i.e., on-board; and the second has a microphone at 25 feet away, i.e., pass-by. The measurements were done by using the 2-channel Larson Davis 3000 Real-Time Analyzers (RTAs). The RTAs were set for 1/8 second exponential averaging and sampled every 1/10 of a second. The on-board sound intensity (OBSI) measurements were consistent with the AASHTO TP 76 procedure (American Association of State Highway and Transportation Officials 2012b). The pass-by measurements were consistent with the American Association of State Highway Officials (AASHTO) test procedure TP 98 for Statistical Isolated Pass-by (SIP) measurements (American Association of State Highway and Transportation Officials 2012a).

Table 4.1 shows the four vehicle types and the corresponding weights used for the measurements CalTrans/CTHWANP-RT-18-365.01.2. In our simulations, we used the vehicle weight for the Malibu vehicle. As the tires used in this report were not accessible to us, we used the passenger car tire that we purchased since it had a radius of 12.8 inches, which is close to the tire radius used for the Malibu car (13.2 inches). The construction and material properties are not the same between the tire reported and the ones we purchased. Thus, we only report on the trends in the noise outputs.

Table 4.1: Testing Vehicles used by CalTrans

Vehicle type	Vehicle weight (kg)
Honda Civic	1253-1365
Malibu	1417-1461
Ford Fusion	1547-1730
Ford Expedition	2468-2582

The rumble strip dimensions for comparison are defined in Table 4.2, and we used these dimensions in our simulations. In this subsection, we also follow the naming convention used in CalTrans/CTHWANP-RT-18-365.01.2, and term the conventional rumble strip as the ground rumble strip, and the sinusoidal rumble strip as the mumble strip to avoid confusion.

Table 4.2: Rumble Strip Dimension Defined by CalTrans

Length (inch)	Width (inches)	Depth (inches)	Wavelength/Spacing (inches)	Type
8	N/A	0.3125	14	Sinusoidal
8	4	0.3125	12	Conventional

We first show the simulated results of the conventional (gray) and sinusoidal (dark blue) designs in the top row of Figure 4.3. The conventional (ground) rumble strip has a depth of 0.3125 inches, a width of 4 inches, and spacing of 12 inches, and the sinusoidal (mumble) strip has a depth of 0.3125 inches and wavelength of 14 inches. We note that the ground rumble strip results (gray) are for most of the frequencies higher than the mumble strip results (dark blue). This is a confirmation that our modeling has created expected results while comparing to the reported observations from the roadside measurements.

In the bottom row for Figure 4.3, we included the on-board and pass-by measurements from the roadside measurements. The results plotted with the dashed curves (cyan for conventional and blue for sinusoidal) were measured from microphones anchored on the tire wheels, and the solid curve results were measured from microphones placed at 25 feet from the vehicles. We performed the same 1/3 octave frequency band averaging as what was documented in CalTrans/CTHWANP-RT-18-365.01.2. Our results, which are in gray for conventional and dark blue for sinusoidal, are higher in the magnitudes than both types of the reported measurements at high frequencies. This is expected as currently our modeling omits polymer noise absorption and sound level loss through air propagation. Our simulation results more consistently show that the conventional rumble strip creates a higher noise level than the sinusoidal and the roadside measurements.

We also highlight the two peaks of the SPL shown in the roadside measurements. We have added dashed orange vertical lines for the on-board results and solid orange vertical lines for the pass-by results. We note that these peaks are not at the same frequencies as the two roadside measurements. Our simulation results also have two peaks and have the same first peak as the pass-by measurement and the same second peak as the on-board measurement. Due to the lack of knowledge of the actual tire used for the roadside measurements, we conjecture that our first peak would be closer to that of the on-board roadside measurement once we model the same tire.

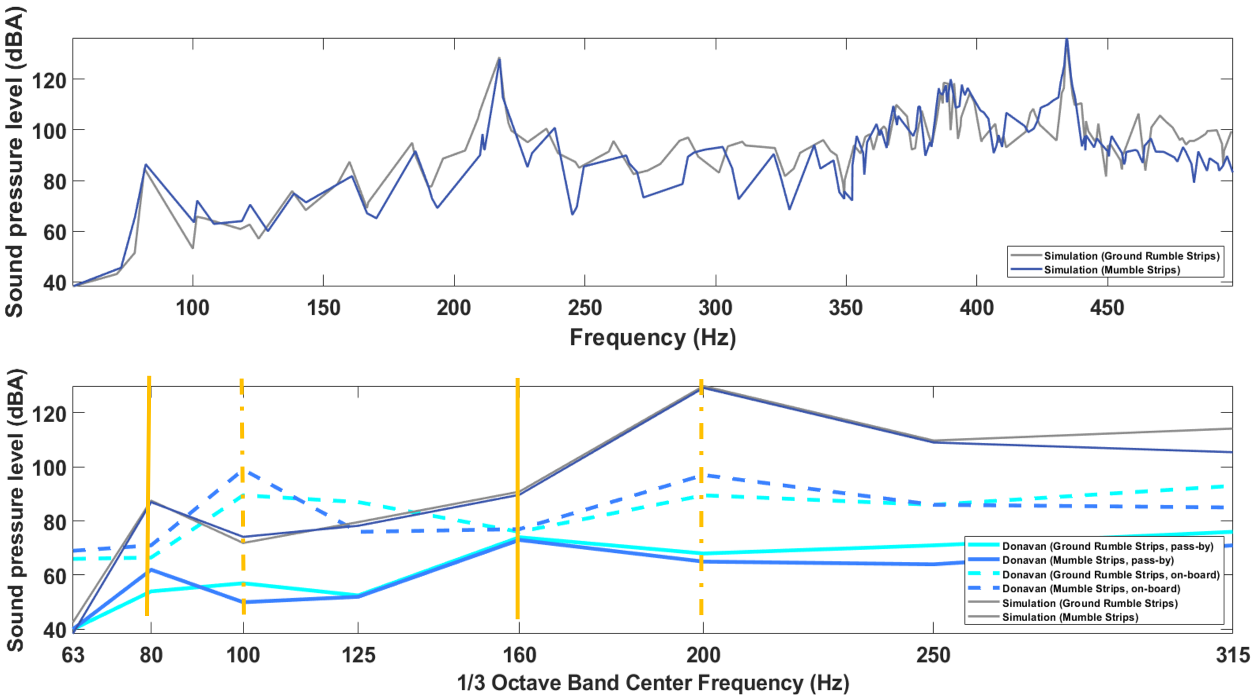

Figure 4.3: SPL comparison. The pass-by and on-board from CalTrans/CTHWANP-RT-18-365.01.2 are compared to the simulation results for the air cavity. Each pair contains the conventional and sinusoidal designs.

4.3 VERIFICATION USING ODOT/SPR800, 2019

In this subsection, we compare our results to those reported in ODOT/SPR800, in which the roadside measurements were presented as overall values for some conventional and sinusoidal rumble strips. There are two vehicles tested as shown in Table 4.3 and we purchased one tire from each vehicle to create our numerical models. The vehicles were driven at 60 mph. We show in Table 4.4 the rumble strip designs and dimensions used in the report.

Table 4.3: Testing Vehicles used in ODOT/SPR800

Vehicle type	Vehicle weight (kg)
2017 Ford Focus Hatchback	1331-1385
Volvo VHD dump truck	13244-36287

Table 4.4: Rumble Strip Geometric Dimensions used in ODOT/SPR800

Length (inches)	Width (inches)	Depth (inches)	Spacing/Wavelength (inches)	Type
14	N/A	0.375	16	Sinusoidal
9.5	8	0.438	12	Conventional

To approximate the reported measurements, we calculated the overall average of the SPL from the frequency range [0, 500] Hz inside the tire and our results are shown in the right column of Table 4.5.

Table 4.5: Comparison of SPLs from ODOT/SPR800 and our Simulations

Vehicle Type	Type	Distance from the microphone to the vehicle (ft)	Roadside measurements (avg dBA)	Simulated results (avg dBA)
Passenger Car	Sinusoidal	25 and 50	87.1	92.9
Passenger Car	Conventional	25 and 50	90.3	94.3
Heavy Vehicle	Sinusoidal	25 and 50	94.5	105.8
Heavy Vehicle	Conventional	25 and 50	95.0	107.2

Our calculated values are higher than those reported in ODOT/SPR800 and follow the same trends in terms of conventional designs having higher outputs than sinusoidal designs and the truck tire having higher outputs than the passenger car tire. The roadside measurements were done at 25 feet and 50 feet from the vehicles, while our values were measured inside the air volume of the tires.

This comparison confirms that our modeling can capture the overall noise outputs of the conventional and sinusoidal rumble strips. In the next section, we numerically evaluate different variations of the dimensions from those published in ODOT/TLM and ODOT/SPR800 for the conventional and sinusoidal patterns. We also include results for the sawtooth designs, whose dimensions are chosen based on one sinusoidal design used in ODOT/SPR800. Our goal is to find sawtooth designs that produce a similar level of SPL output as sinusoidal designs but at a higher wavelength, in an attempt to reduce road surface damage from construction.

5.0 COMPARISON OF EXTERIOR NOISE LEVELS AMONG RUMBLE STRIP DESIGNS AND DIMENSIONS

To analyze the relationship between the tire noise from rolling on the rumble strips and the geometry of the rumble strips, we compare the tire SPL responses over different rumble strip designs. In our simulations, we assume that the tires roll for 0.1 seconds as mentioned in CalTrans/CTHWANP-RT-18-365.01.2, and we compare the accumulated SPLs for this time period. In addition, as both CalTrans/CTHWANP-RT-18-365.01.2 and ODOT/SPR800 show that the dominant frequency ranges are the first peak at around 80 Hz, and the second peak at around 160 Hz, we mainly focus on the frequency range [0, 250] Hz, which covers these two dominant peaks.

We varied the dimensions published by ODOT/TLM (2018) and ODOT/SPR800 (2019) which are shown in Table 5.1 (L: length, W: width, D: depth; S/W: Spacing/Wavelength), and created simulations for each variation as shown in Table 5.2 and the original dimensions for comparison. We developed scatter plots to facilitate the comparisons, and the results are shown in Section 5.1. There are a total of 19 conventional designs and 21 sinusoidal designs that we have simulated. For each case, we simulate the passenger car and truck tires (Table 4.3) at three vehicle speeds. We group our plots of the results into categories of the design type, i.e., sinusoidal designs or conventional designs; tire type, i.e., passenger or truck; and speeds, i.e., 45 mph, 55 mph, or 65 mph.

Table 5.1: Geometric Dimensions from ODOT/TLM and ODOT/SPR800

Report	L (inches)	W (inches)	D (inches)	S/W (inches)	Type
ODOT/TLM	8	7	0.5	12	Conventional
ODOT/TLM	8	N/A	0.5	12	Sinusoidal
ODOT/SPR800	9.5	8	0.438	12	Conventional
ODOT/SPR800	14	N/A	0.375	16	Sinusoidal

Table 5.2: Variations of the Geometric Dimensions for Comparison

L (inches)	W(inches)	D (inches)	S/W (inches)	Type
8	7	0.3, 0.4, 0.5, 0.6, 0.625	12	Conventional
8	5,6,8,9	0.5	12	Conventional
8	N/A	0.3, 0.4, 0.5, 0.6, 0.625	12	Sinusoidal
8	N/A	0.5	8, 10, 14, 16, 18	Sinusoidal
9.5	8	0.2628, 0.3504, 0.438, 0.53, 0.6132, 0.625	12	Conventional
9.5	6,7,9,10	0.438	12	Conventional
14	N/A	0.225, 0.3, 0.375, 0.45, 0.525, 0.625	16	Sinusoidal
14	N/A	0.375	12, 14, 18, 20, 22	Sinusoidal

In addition, we have developed dimensions for the sawtooth designs using one existing sinusoidal dimension, i.e., depth at 0.375 inches and wavelength at 16 inches that was used in ODOT/SPR800. Table 5.3 presents the geometric dimensions for the sawtooth design. As the sawtooth designs have asymmetric side profiles, there can be different cases for each design by moving the troughs in the profiles (Figure 5.1 and Figure 5.2). For the sawtooth designs, we use one depth value, 0.375 inches, and increase the wavelength. Furthermore, we keep the side profile to have straight edges.

Table 5.3: Geometric Dimensions for Sawtooth Designs

L (inches)	D (inches)	W (inches)	Cases	Type
8/long-enough	0.375	16	Long climb quick drop	Sawtooth
8/long-enough	0.375	20	Long climb quick drop	Sawtooth
8/long-enough	0.375	25	Long climb quick drop	Sawtooth
14	0.375	16	Short climb slow drop	Sawtooth
14	0.375	20	Short climb slow drop	Sawtooth
14	0.375	25	Short climb slow drop	Sawtooth

Figure 5.1: Side profiles of the sawtooth-long-climb-quick-drop design.

Figure 5.2: Side profiles of the sawtooth-short-climb-slow-drop design.

In Section 5.1, we first examine conventional designs for the passenger car tire and the truck tire. In Section 5.2, we examine sinusoidal designs. In Section 5.3, we further compare one conventional and sinusoidal design dimension only at the 55-mph speed using dimensions with the lowest SPL outputs from the two designs. In Section 5.4, we compare the sawtooth designs to one reference sinusoidal design. All SPLs are calculated within the frequency range [0, 250] Hz. In Section 5.5, we create visualizations to show the ranking of conventional and sinusoidal designs over SPL levels.

5.1 SPL COMPARISON OF DIFFERENT DIMENSIONS FOR CONVENTIONAL DESIGNS

SPL responses over different frequencies were analyzed in the MATLAB software package (version 2021). We show our results for the passenger car SPL responses over 19 conventional designs in Figure 5.3 and for the truck tire SPL responses over the same 19 conventional designs in Figure 5.4. Along the horizontal axis, we increase the depth and along the vertical axis, we increase the width/wavelength. Thus, we expect the values to go from low to high horizontally and from high to low vertically. Dark blue is low value and dark red is high value. We further differentiate the results by using circle dots for the variations from ODOT/SPR800 and triangle dots for the results from the ODOT/TLM in Table 5.2. The vehicle speeds are 45 mph (left), 55 mph (middle), and 65 mph (right) in these figures.

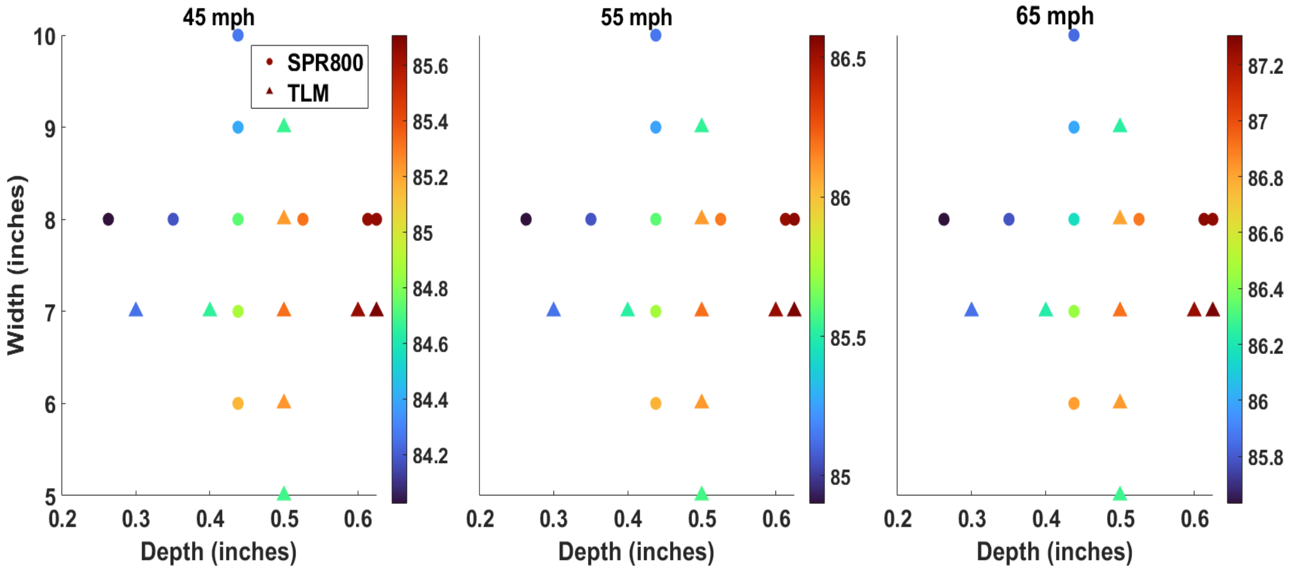

Figure 5.3: SPL comparison of conventional designs for the passenger car tire. For each speed 45 mph (left), 55 mph (middle), and 65 mph (right), circle dots are for variations to ODOT/SPR800, and triangle dots are for variations to ODOT/TLM. The horizontal axis shows the depth variation, and the vertical axis shows the width variation.

For the horizontal line of circle dots at a width of 8 inches, we note the deeper groove of the rumble strip causes higher SPL. The color of the dots changes from dark blue to dark red. A similar trend is noted for the horizontal line of triangle dots that indicate the variations from ODOT/TLM for the width at 7 inches. This trend is expected.

For the vertical line for the depth at 0.438 inches, we note the larger width of the rumble strip causes a smaller SPL. The color changes from orange to light blue. A similar trend is noted for the vertical line of triangle dots above the width of 7 inches. When the width is at 5 inches, we observe a low SPL value for all three speeds, i.e., cyan color triangle dots at the bottom of the three images. We conjecture that our sampling of the groove at this width was not refined enough as the curvature of this narrowest groove is the highest. In our current studies, we evenly allocate 7 sampling locations for the half-spacing, which includes the features of the half groove and flat portion. In future work, we will allocate more sampling for the curved grooves. Furthermore, the SPL value at 6 inches is slightly lower than that at 7 inches, i.e., a slightly lighter orange color for the triangle dot at 6 inches. We expected the SPL value at 6 inches to be higher. More refined sampling should also alleviate this discrepancy.

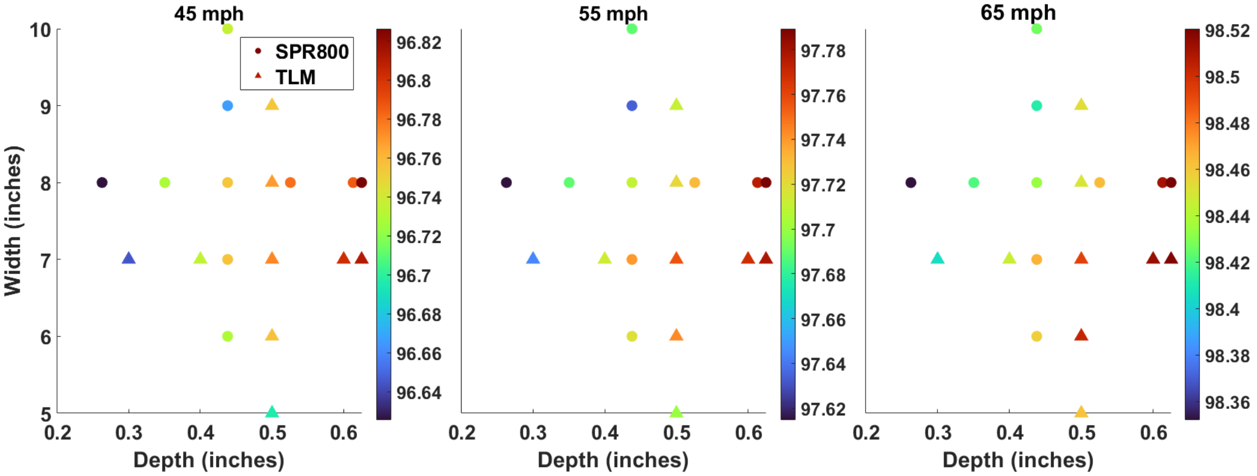

Figure 5.4: SPL comparison of conventional designs for the truck tire. For each speed 45 mph (left), 55 mph (middle), and 65 mph (right), the horizontal axis shows the depth variation, and the vertical axis shows the width variation.

We compare in Figure 5.4 the truck tire SPL responses over conventional rumble strip designs with different widths and depths. The dimensions of the designs are the same as those for the passenger car tire.

Very similar to the passenger car tire, for the horizontal line of circle dots at the width of 8 inches, we note the deeper groove of the rumble strip causes higher SPL. The color of the dots changes from dark blue to dark red. This trend is also noted for the horizontal line of triangle dots at the width of 7 inches.

For the vertical line of circle dots at the depth of 0.438 inches, we note the SPL values are decreasing in general, i.e., the colors change from orange to blue or green. The SPL output for the width of 10 inches is slightly higher than that of 9 inches by about 0.07 dBA, and the SPL output for the width of 6 inches is slightly lower than that of 7 inches by about 0.03 dBA. For the vertical line of triangle dots at the depth of 0.5 inches, the SPL decreases as the width increases except slightly increasing when the width is at both 5 and 6 inches. Again, these slight discrepancies are likely due to insufficient sampling for the narrow grooves in our current schemes.

In addition, we observe that the differences in SPLs for the truck tire over the dimensions are lower than those for the passenger car tire (Figure 5.3). The SPL difference range for the truck tire is [0.0, 1.89] dBA while it is [0.0, 3.28] dBA for the passenger car tire. We conjecture the reason is due to the higher rigidity of the truck tires, which contain more steel cords, and the features from the rumble strip patterns become less effective on the truck tires.

5.2 SPL COMPARISON OF DIFFERENT DIMENSIONS FOR SINUSOIDAL DESIGNS

In this subsection, we focus on sinusoidal designs. Each circle dot is a variation of the reference ones in ODOT/SPR800, and each triangle dot is a variation of the reference ones in ODOT/TLM as described in Table 5.2. We compare in Figure 5.5 the passenger car tire SPL responses over 21 sinusoidal designs with different wavelengths and depths.

For the horizontal line of circle dots for the wavelength at 16 inches, we note the SPL increases with the depth increasing. The color of the dots changes from blue to green. A similar trend is noted for the horizontal line of triangle dots that indicate the variations from ODOT/TLM for the wavelength at 12 inches. The color changes from yellow to orange. There is one slight exception at depth of 0.4 inches for the speed of 65 mph.

For the vertical line of circle dots for the depth of 0.375 inches, we note the SPL decreases as the wavelength increases. The color of the dots changes from yellow to dark blue. For the vertical line of triangle dots that indicate variations from those dimensions used in ODOT/ TLM for the depth at 0.5 inches, the trend is the same. The color of the dots changes from dark red to blue.

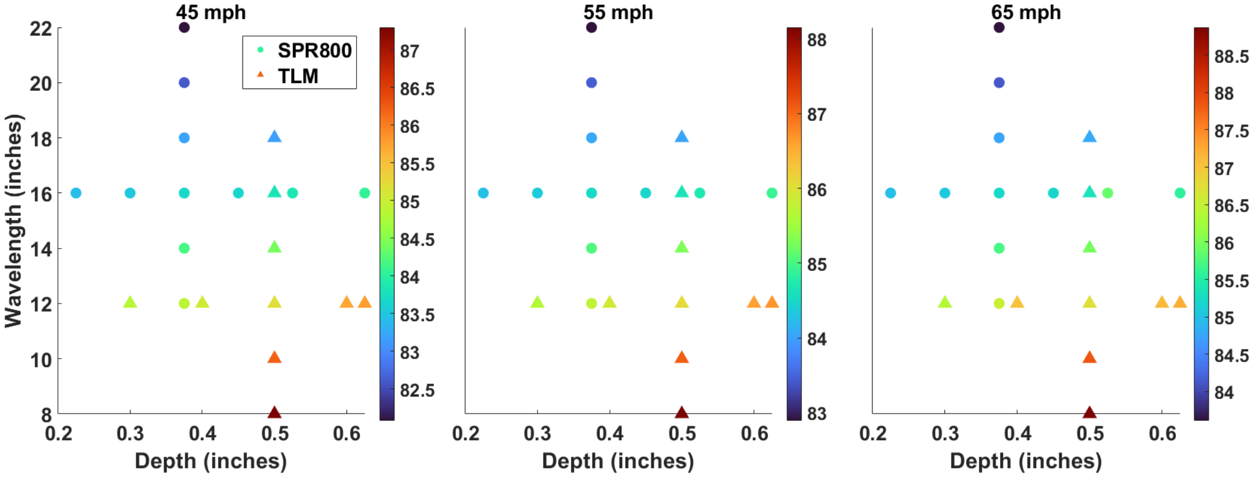

Figure 5.5: SPL comparison of sinusoidal designs for the passenger car tire. For each speed 45 mph (left), 55 mph (middle), and 65 mph (right), the horizontal axis shows the depth variation, and the vertical axis shows the wavelength variation.

Similarly, we compare in Figure 5.6 the truck SPL responses. For the horizontal line of circle dots for the wavelength at 16 inches, we note the SPL slightly increases as the depth increases. The color of the dots is almost the same color (cyan). A similar observation is noted for the horizontal line of triangle dots for the wavelength is 12 inches (yellow), which indicates little sensitivity to the depth change for the truck tire. Along the vertical lines, the SPL decreases as the wavelength increases.

As for conventional designs, the above plots in general indicate that as the depth increases the SPL values become larger (darker red colors), and as the wavelength increases the SPL values become smaller (darker blue colors). Furthermore, we observe that the differences in SPLs are smaller than those for the passenger car tire, similar to our observations for conventional designs. This implies that the tire size and material matter. For designs at different depths, the range of minimum and maximum differences in SPL responses for the passenger car tire is [0.01, 1.91] dBA compared to [0, 0.11] dBA for the truck tire. Overall, we see more consistent trends for sinusoidal designs than for conventional designs.

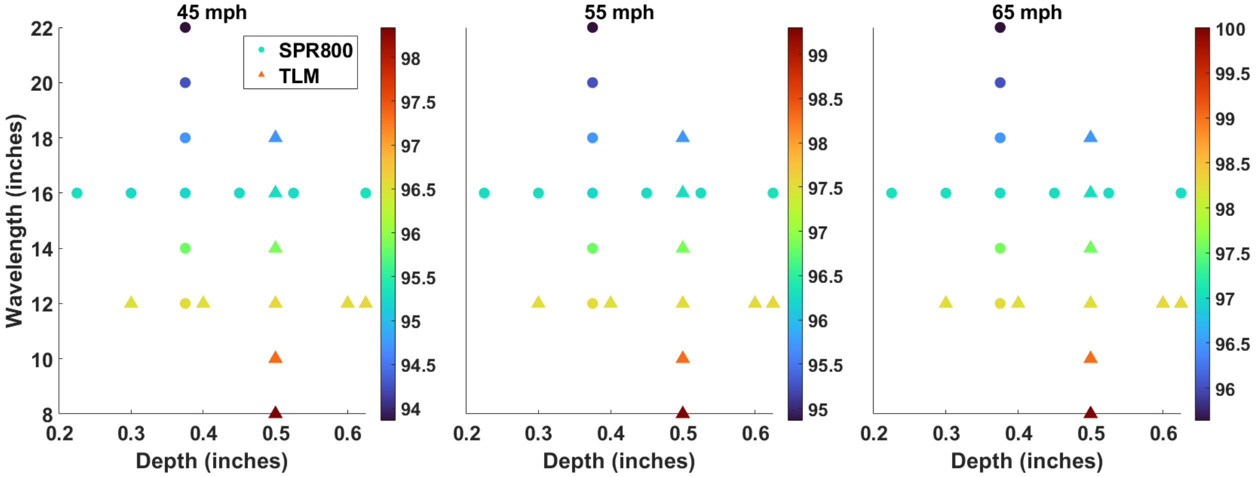

Figure 5.6: SPL comparison of sinusoidal designs for the truck tire. For each speed 45 mph (left), 55 mph (middle), and 65 mph (right), the horizontal axis shows the depth variation, and the vertical axis shows the wavelength variation.

5.3 SPL COMPARISON OF CONVENTIONAL AND SINUSOIDAL DESIGNS

To further contrast conventional and sinusoidal designs, we only select the 55-mph speed. In Figure 5.7**,** we present the passenger car tire and truck tire SPL outputs over the range of frequencies [0 250] Hz. The top row compares conventional (gray) and sinusoidal (dark blue) for the passenger car tire, and the bottom row compares for the truck tire. The conventional design has a depth of 0.2628 inches, a width of 8 inches, and a spacing of 12 inches with 84.90 dBA for the passenger car tire and 97.61 dBA for the truck tire. The sinusoidal design dimension has a depth of 0.375 inches, and a wavelength of 22 inches with 82.89 dBA for the passenger car tire and 94.86 dBA for the truck tire. These SPL values are the lowest among our simulations for each tire type and each rumble strip design, respectively.

We note that the differences between the two designs are more pronounced over relatively higher frequencies for the passenger car tire and over both low and high frequencies for the truck tire. The maximum difference is higher for the passenger car tire than the truck tire. These SPL responses over the frequencies indicate that tire noises vary with respect to the geometry of the rumble strips and the tire types.

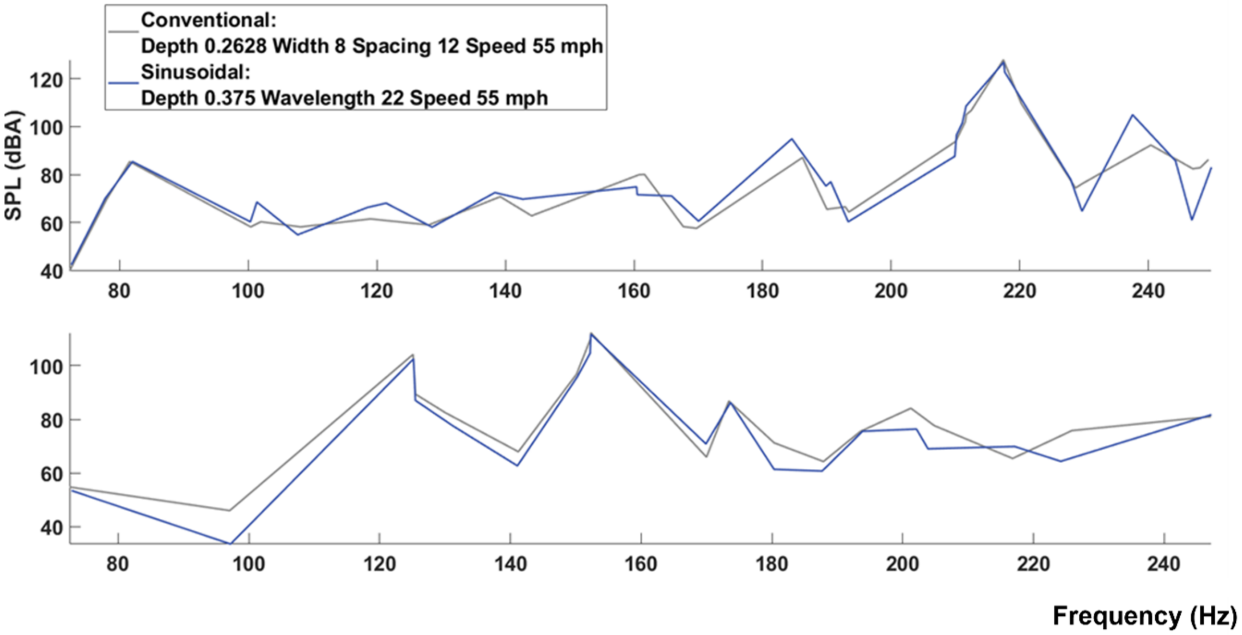

Figure 5.7: SPL comparison between conventional and sinusoidal designs. Over the frequency range [0, 250] Hz, the SPL outputs at 55 mph are shown for the passenger car tire (top) and truck tire (bottom).

5.4 SPL COMPARISON OF SAWTOOTH AND SINUSOIDAL DESIGNS

As the rumble strips are both aural and tactile devices to alert the drivers, we have considered a sawtooth design that has an asymmetric profile. We project drivers would feel climbing and falling differently due to the different lengths of these two segments. In addition, if the falling is short, then it can potentially be strong tactile feedback. Conventional and sinusoidal designs are currently the most common rumble strips used in practice. Both conventional and sinusoidal designs have symmetric profiles with respect to the centers of the grooves.

We have developed 2 sawtooth designs: the sawtooth-long-climb-quick-drop scenario (Figure 5.1), and the sawtooth-short-climb-slow-drop scenario (Figure 5.2). In this section, we examine the SPL differences between the sawtooth designs and the reference sinusoidal design from ODOT/SPR800. We have chosen the same depth, 0.375 inches for all designs, and varied the wavelengths among three values: 16 inches, 20 inches, and 25 inches for the sawtooth designs to contrast to the sinusoidal design at 16 inches only. We have observed that the same depth but a longer wavelength of the sawtooth can be quieter than the reference sinusoidal.

The contact areas between the tires and the rumble strips directly influence the SPL output levels. In this subsection, we visualize the mechanical stress values, the contact areas, and the displacements for the sawtooth and the reference sinusoidal design. We first present comparisons between the sawtooth-long-climb-quick-drop scenario and the sinusoidal design over Von Mises stresses for the tread and sidewall, and the displacements in three directions: rolling, lateral, and loading for the air elements. We then show comparisons between the sawtooth-short-climb-slow-drop scenario and the sinusoidal design. These different visualizations provide a comprehensive understanding of the distribution of the deformation in the tire elements and the air elements caused by the rumble strip geometries.

In Figure 5.8, we show Von Mises stresses in the tread and the sidewall. Both designs have a depth of 0.375 inches and a wavelength of 16 inches. We note that the stresses are higher in sawtooth-long-climb-quick-drop at the peaks of this design than in sinusoidal. Also, the sinusoidal smooth design has a stress distribution that is uniform in the contract area while the sawtooth design has isolated high points.

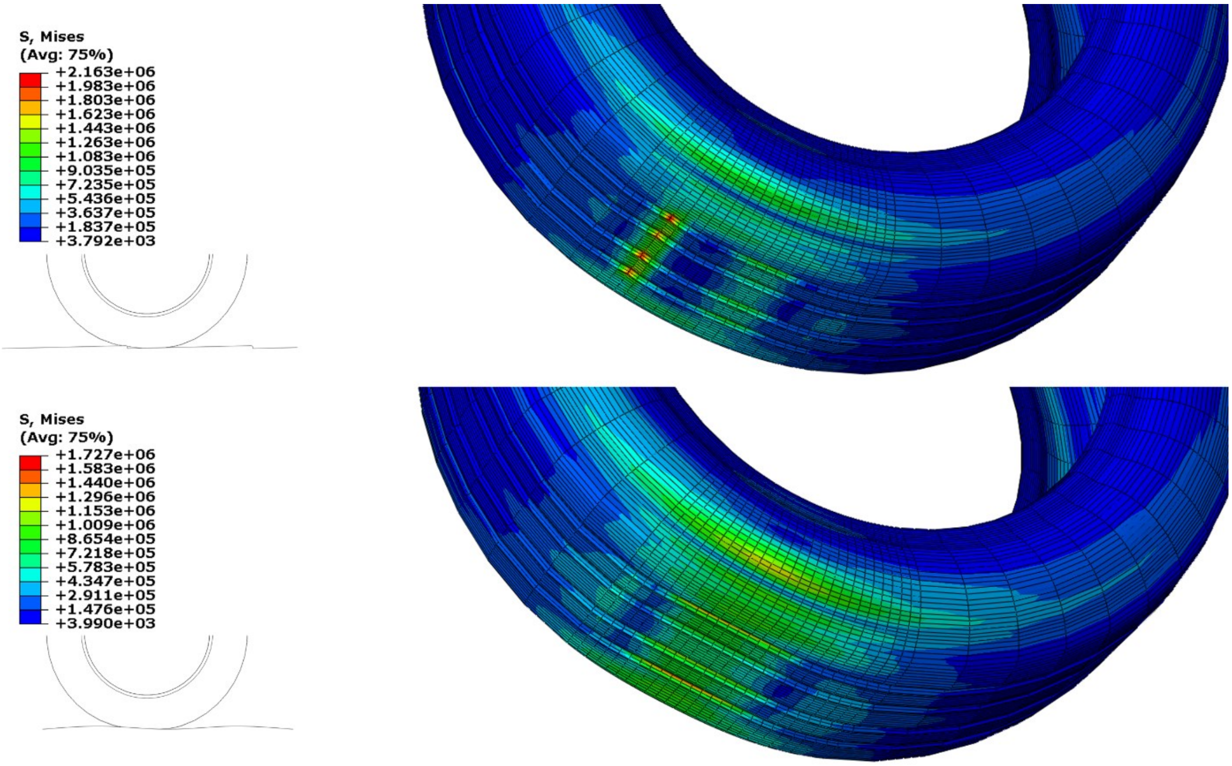

Figure 5.8: Von Mises Stress comparison. For the passenger car tire tread and sidewall, the Von Mises Stresses are shown for the sawtooth-long-climb-quick-drop design in the top image, and the reference sinusoidal design dimension in the bottom image.

Next, we show the displacement of the air elements for the rolling, lateral, and loading directions respectively in Figure 5.9, Figure 5.10, and Figure 5.11.

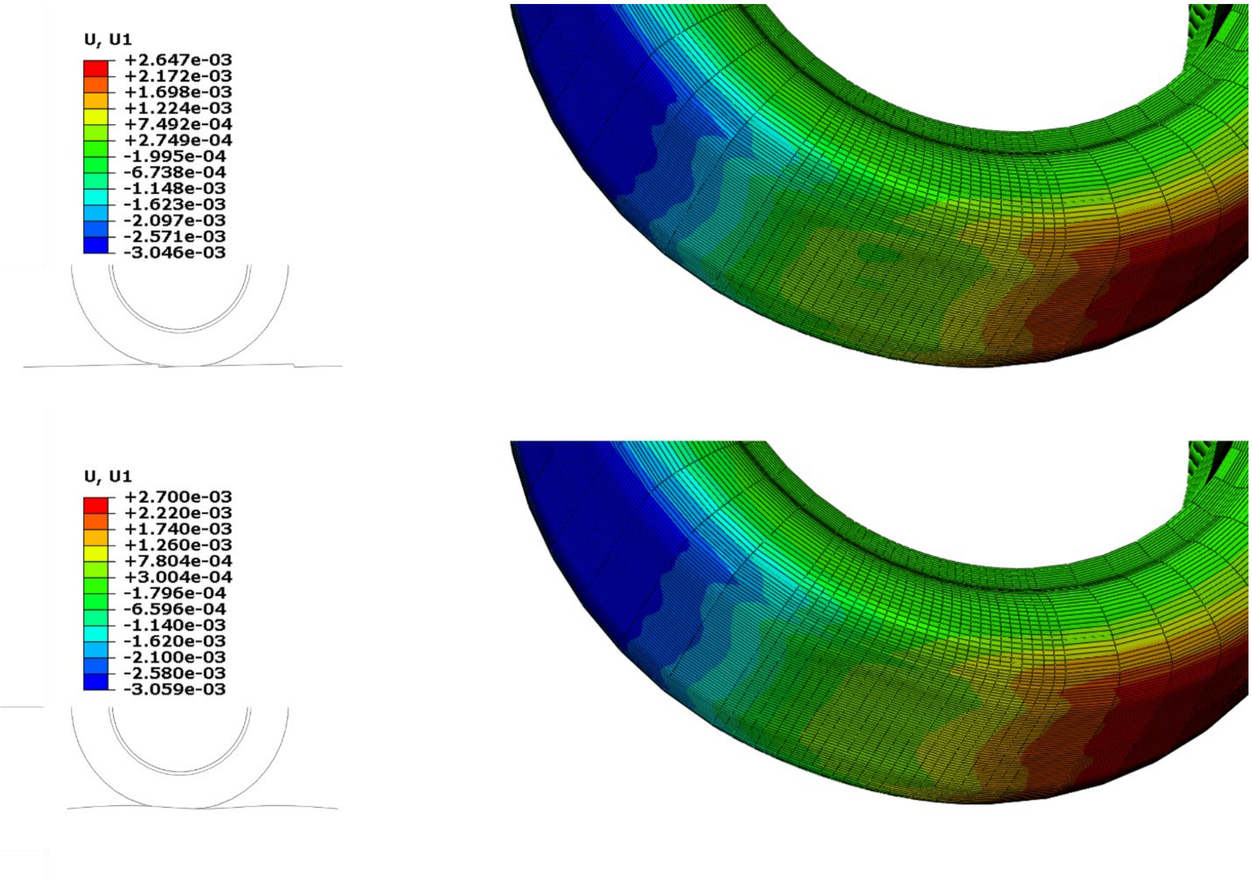

Figure 5.9: Displacement magnitude comparison in the rolling direction for the air cavity inside the passenger car tire. The sawtooth-long-climb-quick-drop design (top), and the reference sinusoidal design dimension (bottom).

We note that in the rolling direction, both designs have a similar distribution of high (red) and low (blue) values. The location of the medium (yellow) values at the contact area (the flattened portion of the tire) correspond to the peaks of the two designs. The sawtooth-long-climb-quick-drop design, the top image of Figure 5.9, has this location to the left in the contact area while the reference sinusoidal design has it at the center of the contact area as expected. Due to the different distributions of high displacement air elements, these two designs produce different tire SPL responses. Furthermore, this visualization again confirms that the tire treads transmit the forces from the rumble strips to the air inside the tire.

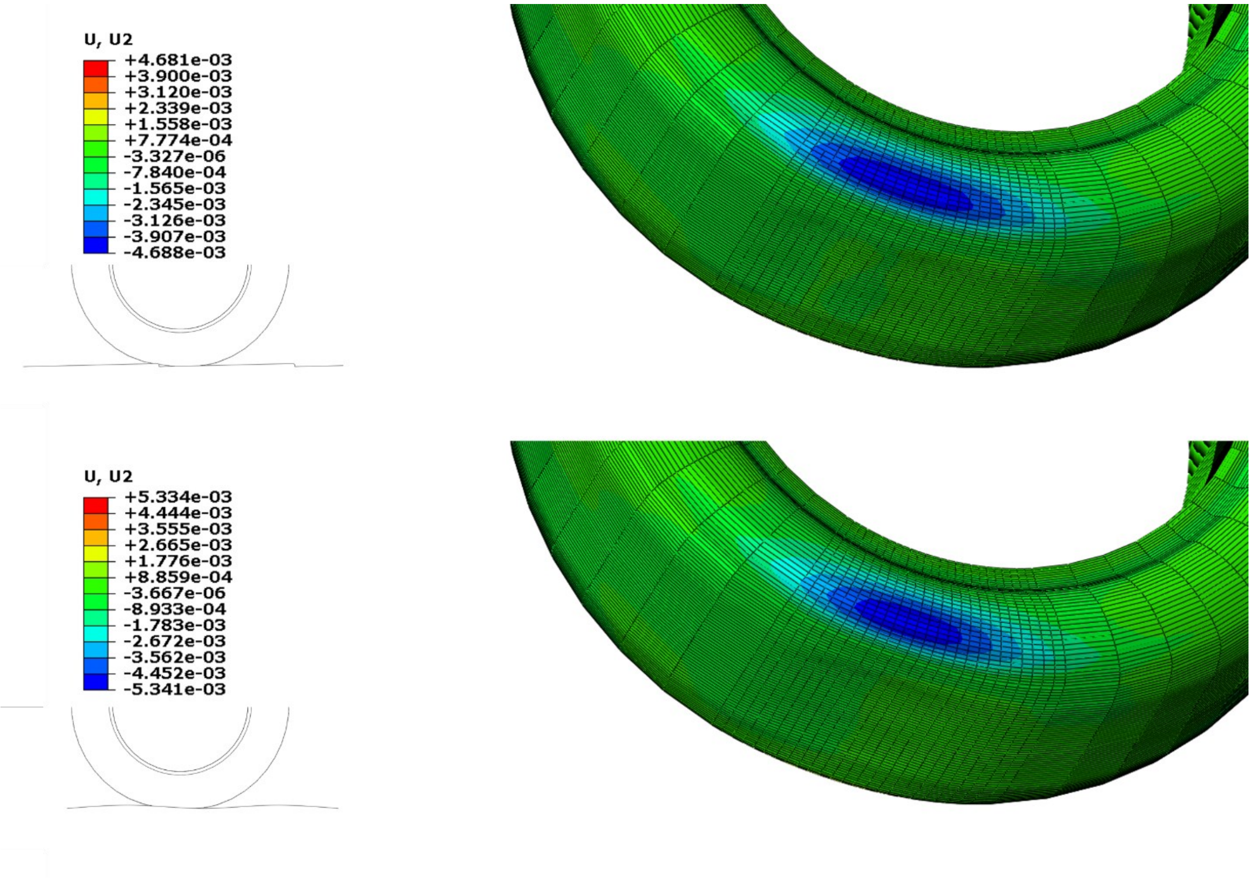

Figure 5.10: Displacement magnitude comparison in the lateral direction for the air cavity inside the passenger car tire. The sawtooth-long-climb-quick-drop design (top) and the reference sinusoidal design dimension (bottom).

For this lateral direction, we note that both designs have regions that are caving inward (blue color). The sawtooth design has a larger region but at a smaller value than the sinusoidal design. This visualization shows that the air volume inside the tires is not expanding uniformly during rolling.

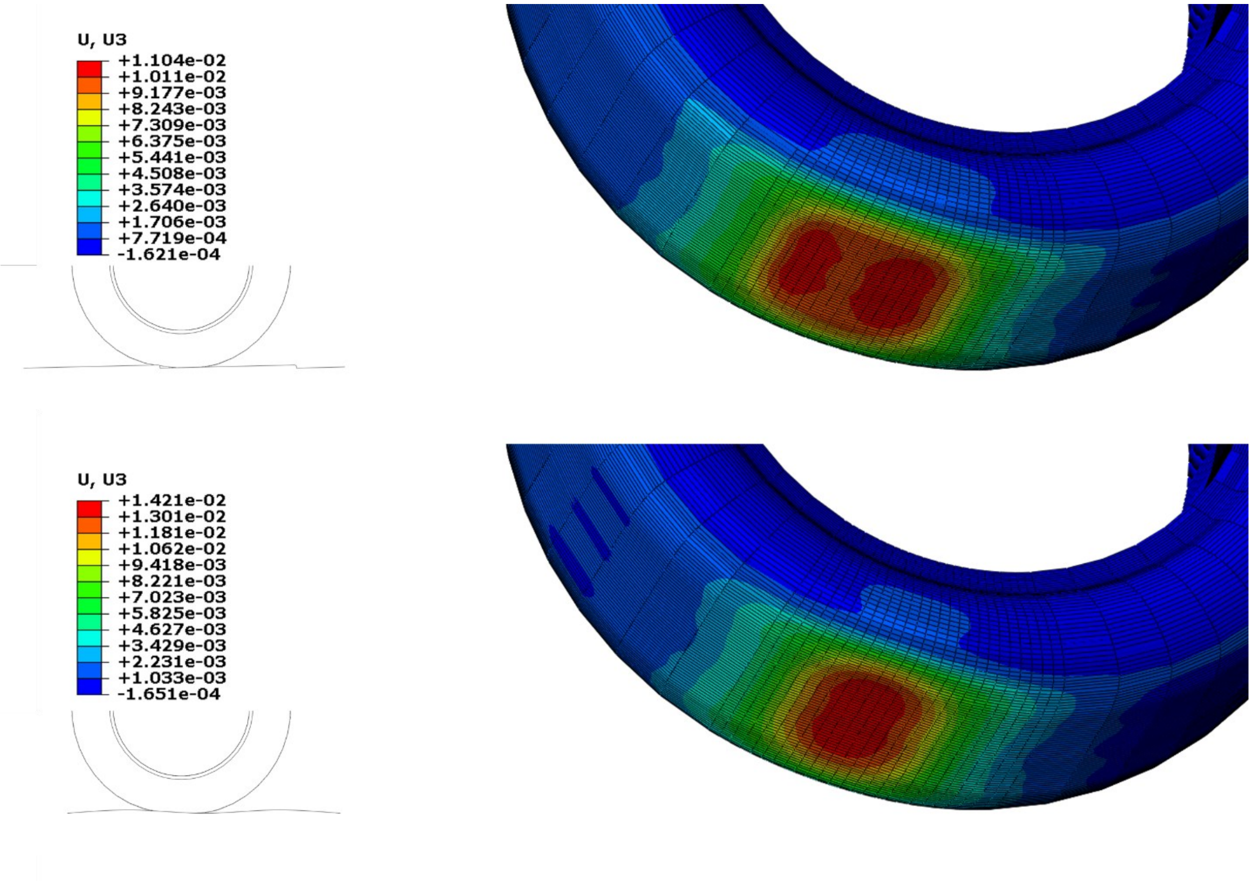

Figure 5.11: Displacement magnitude comparison in the loading direction for the air cavity inside the passenger car tire. The sawtooth-long-climb-quick-drop design (top), and the reference sinusoidal design dimension (bottom).

In the loading direction, it is obvious that the sawtooth design has a larger high displacement (red) region but at a slightly lower magnitude than the sinusoidal design. This larger area is due to the sharp peak in the sawtooth design.

Next, we quantify the differences in the acoustic outputs between these two designs. We use the same scheme in our verification against the CalTrans/CTHWANP-RT-18-365.01.2, 2018 report, i.e., we accumulate the SPL levels over 0.1 seconds. For the sawtooth design, we use three wavelengths: 16 inches, 20 inches, and 25 inches, and just 16 inches for the reference sinusoidal design.

In the top image of Figure 5.12, we compare for the passenger car tire, and in the bottom image the truck tire. The reference sinusoidal design with a depth of 0.375 inches and a wavelength of 16 inches is in purple at the far right for each speed. The other three bars are the sawtooth-long-climb-quick-drop at wavelengths of 16, 20, and 25 inches, respectively. We observe that 1) The SPL decreases with increasing wavelength for the sawtooth design and 2) The SPL of the sawtooth design is lower than that of the sinusoidal design.

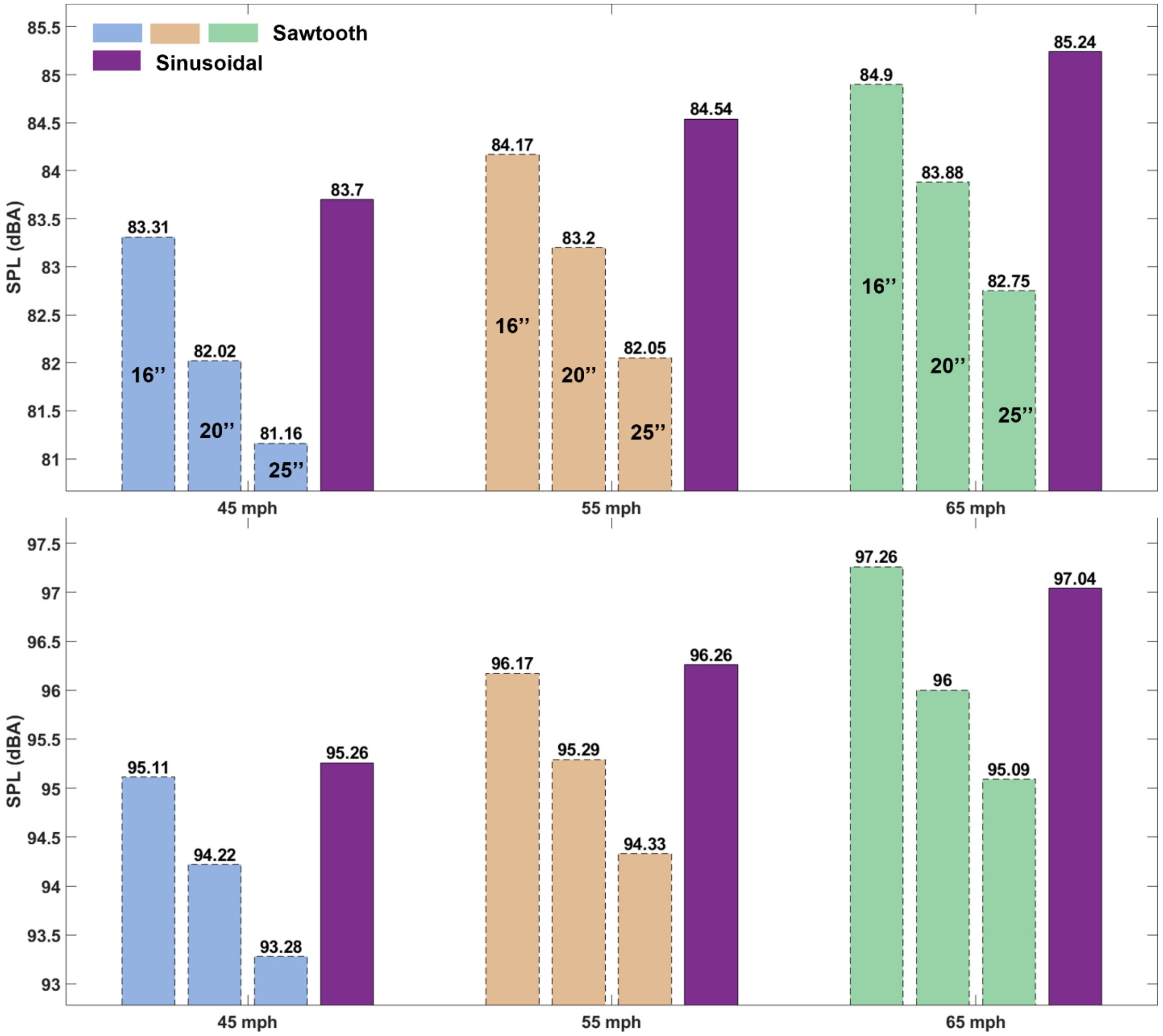

Figure 5.12: SPL comparisons for sawtooth-long-climb-quick-drop and sinusoidal designs. The SPLs are shown for the sawtooth-long-climb-quick-drop designs and the reference sinusoidal design dimension for the passenger car tire (top) and truck tire (bottom).

We observe that for both passenger car and truck tires, the sawtooth-long-climb-quick-drop design can have comparable SPL values at the same depth and the same wavelength. When the wavelength of the sawtooth design increases to 20 inches and 25 inches, these dimensions produce lower SPLs than the sinusoidal design at a wavelength of 16 inches.

Next, we make similar comparisons for the sawtooth-short-climb-slow-drop scenario with a depth of 0.375 inches and a wavelength of 25 inches and the reference sinusoidal design at the same depth and a wavelength of 16 inches. In Figure 5.13 we show the stress in the loading direction instead of the Von Mises stress and we analyze the tire tread rather than the air element. On these treads, we show in Figure 5.14 the air displacement in the rolling direction (top), the lateral direction (middle), and the loading direction (bottom).

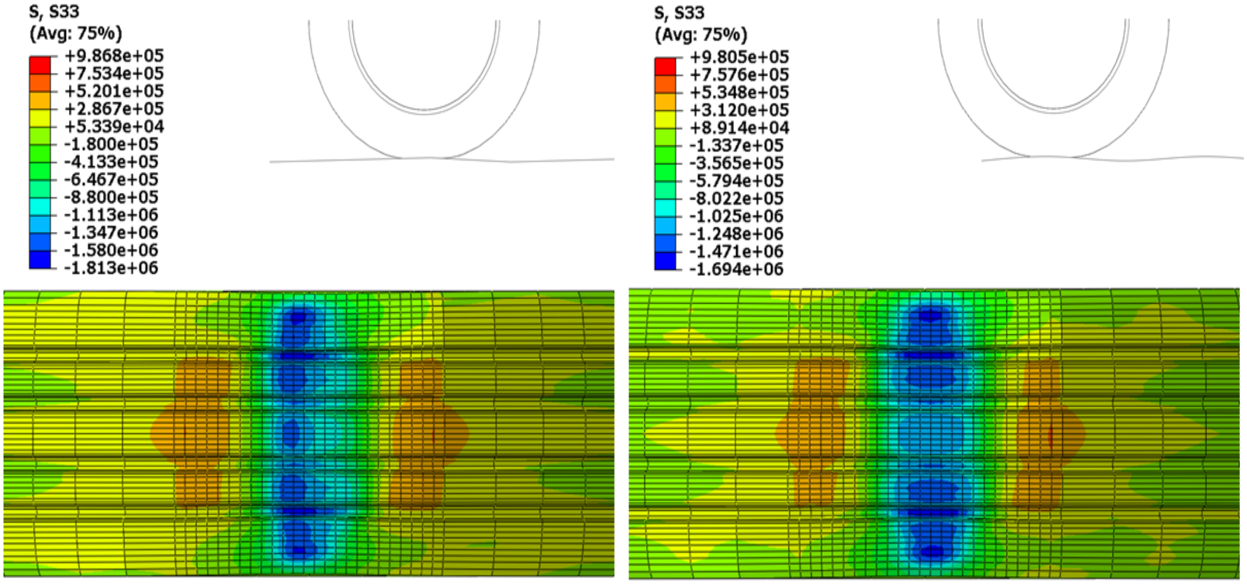

Figure 5.13: Stress in the loading direction. For the passenger car tire tread, stresses in the tread are shown for the sawtooth-short-climb-slow-drop design (left) and the reference sinusoidal design dimension (right).

We note that the distributions of the high (orange) and low (blue) values are different for these two designs. The sinusoidal design has a more symmetric distribution than the sawtooth design as expected.

Similarly, the difference between the two designs is visible in the air displacement along with the rolling, lateral, and loading directions (Figure 5.14). We note that the sawtooth design has a smaller value than the sinusoidal design in all three directions. Especially, in the loading directions, the sawtooth design has a larger region (red) but at a smaller value than the sinusoidal design.

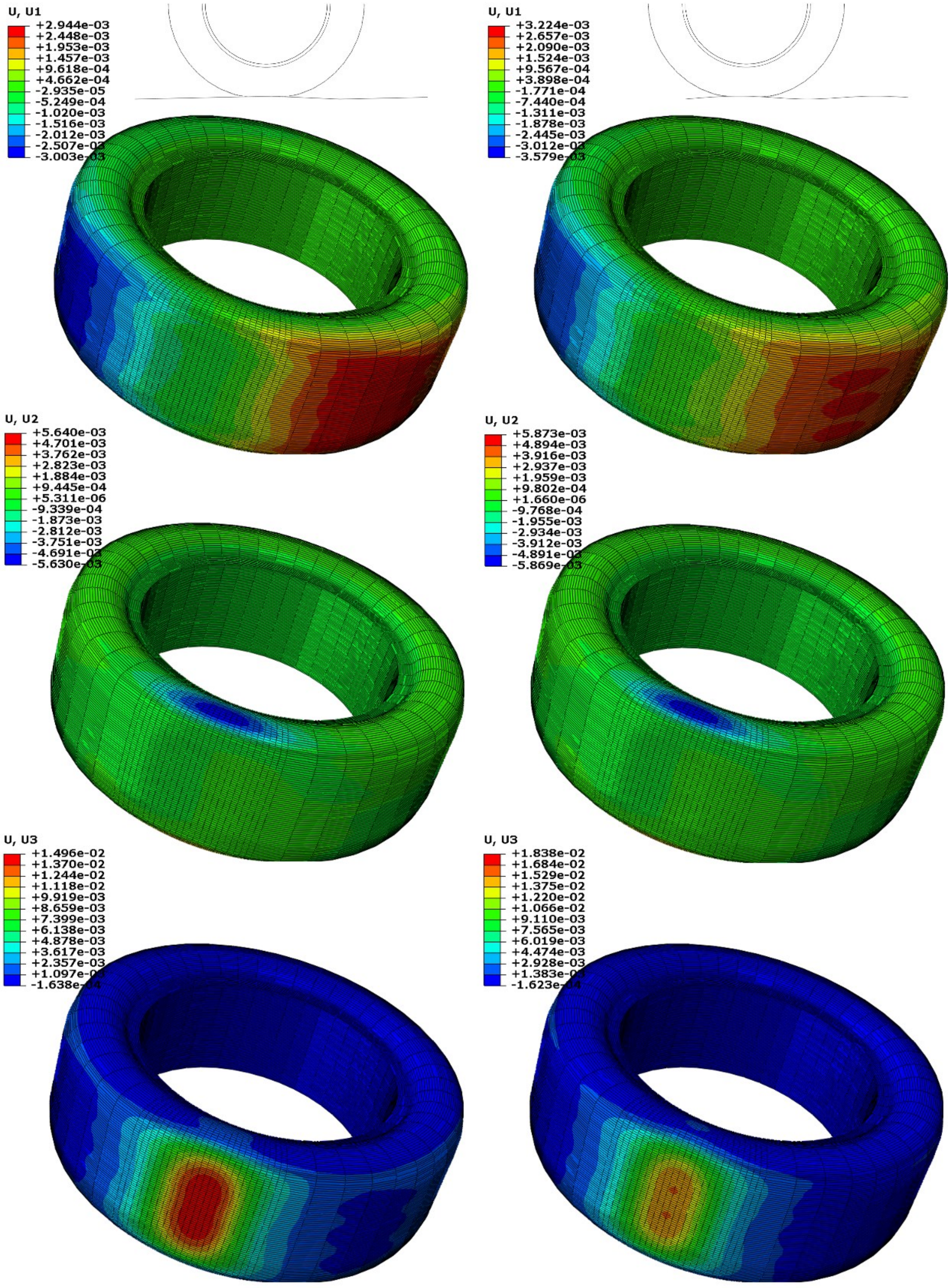

Figure 5.14: The displacement in rolling, lateral, and loading directions. The displacement in rolling (top), lateral (middle), and loading (bottom) directions for the air cavity in the passenger car tire are shown for the sawtooth-short-climb-slow-drop design (left) and the reference sinusoidal design dimension (right).

In Figure 5.15, we compare for the passenger car tire (top) and for the truck tire (bottom). The reference sinusoidal design with a depth of 0.375 inches and a wavelength of 16 inches is in purple at the far right for each speed. The other three bars are the sawtooth-short-climb-slow-drop at wavelengths of 16, 20, and 25 inches, respectively. We have observed that the SPL decreases with increasing wavelength and that the SPL of the sawtooth design at the wavelength of 20 or 25 inches is lower than the sinusoidal design.

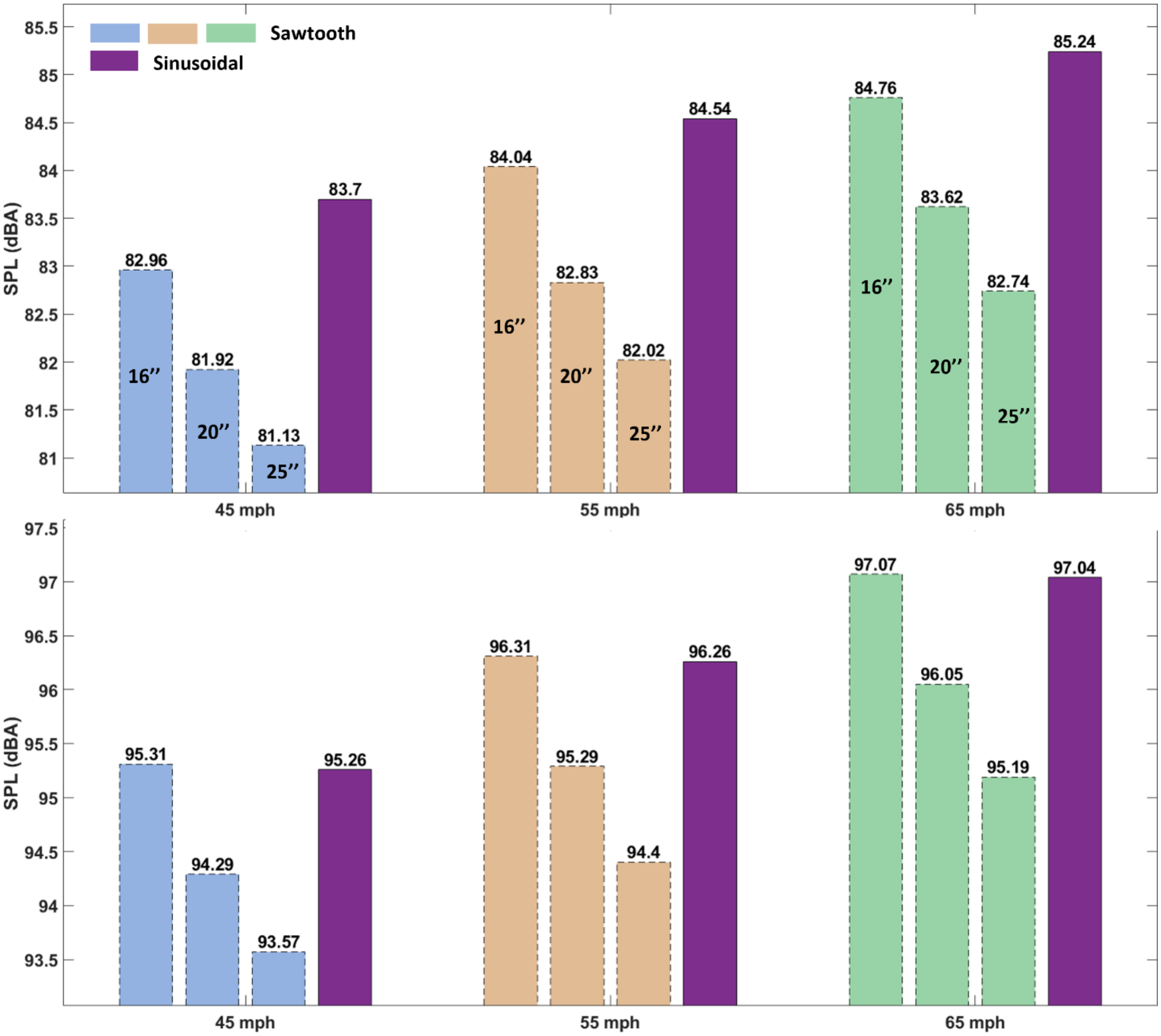

Figure 5.15: SPL comparisons for sawtooth-short-climb-slow-drop and sinusoidal designs. The SPLs are shown for the sawtooth-short-climb-slow-drop designs and the reference sinusoidal design dimension for the passenger car tire (top) and truck tire (bottom).

Furthermore, we note that the two sawtooth designs have comparable performances when compared to the reference sinusoidal design. At 20 inches wavelength, both designs are about 1 dBA lower than the sinusoidal design at 16 inches for all three speeds. We conjecture using the 20 inches as the wavelength can potentially incur less road change during construction. Furthermore, between the two sawtooth designs, the long-climb-quick-drop has a higher SPL output of about 0.3 dBA than the short-climb-slow-drop for the passenger car, but a lower output of about 0.2 dBA for the truck tire. When traffic volume distributions of the car and truck tires are included in future work, these two designs can be further customized to meet the required noise levels.

5.5 VISUALIZATION FOR SPL RANKING OVER RUMBLE STRIP DIMENSIONS

Finally in this subsection, we focus on presenting the designs along with their simulated SPLs so that a selection of a particular rumble strip dimension can be easily made in practice. We present two visualizations, heatmap and tree, to facilitate the selection of a rumble strip dimension that has a required SPL level. We use color to indicate high (red) and low (blue) values. In the heatmap visualization, each block contains the SPL (dBA), depth (D), spacing (S), width (W), and speed; and in the tree visualization, these numbers are written next to the tree nodes and the speed is omitted as the 3 speeds are averaged. Furthermore, in the tree visualization, the width of the edges increases with the SPL differences. In the heatmap visualization, we present all the dimensions that we have simulated and mark the geometric dimensions in the report of ODOT/TLM and ODOT/SPR800 with dashed red boxes. In the tree visualization, we only show the dimensions that have lower SPLs than those used in ODOT/TLM and ODOT/SPR800. The colored nodes represent the SPL values, and from light to dark color, the SPL value decreases.

The heatmap visualization is a global look-up table while the tree visualization is to enable local search. These visualizations when enlarged can be read easily to select a rumble strip dimension at some required SPL dBA levels.

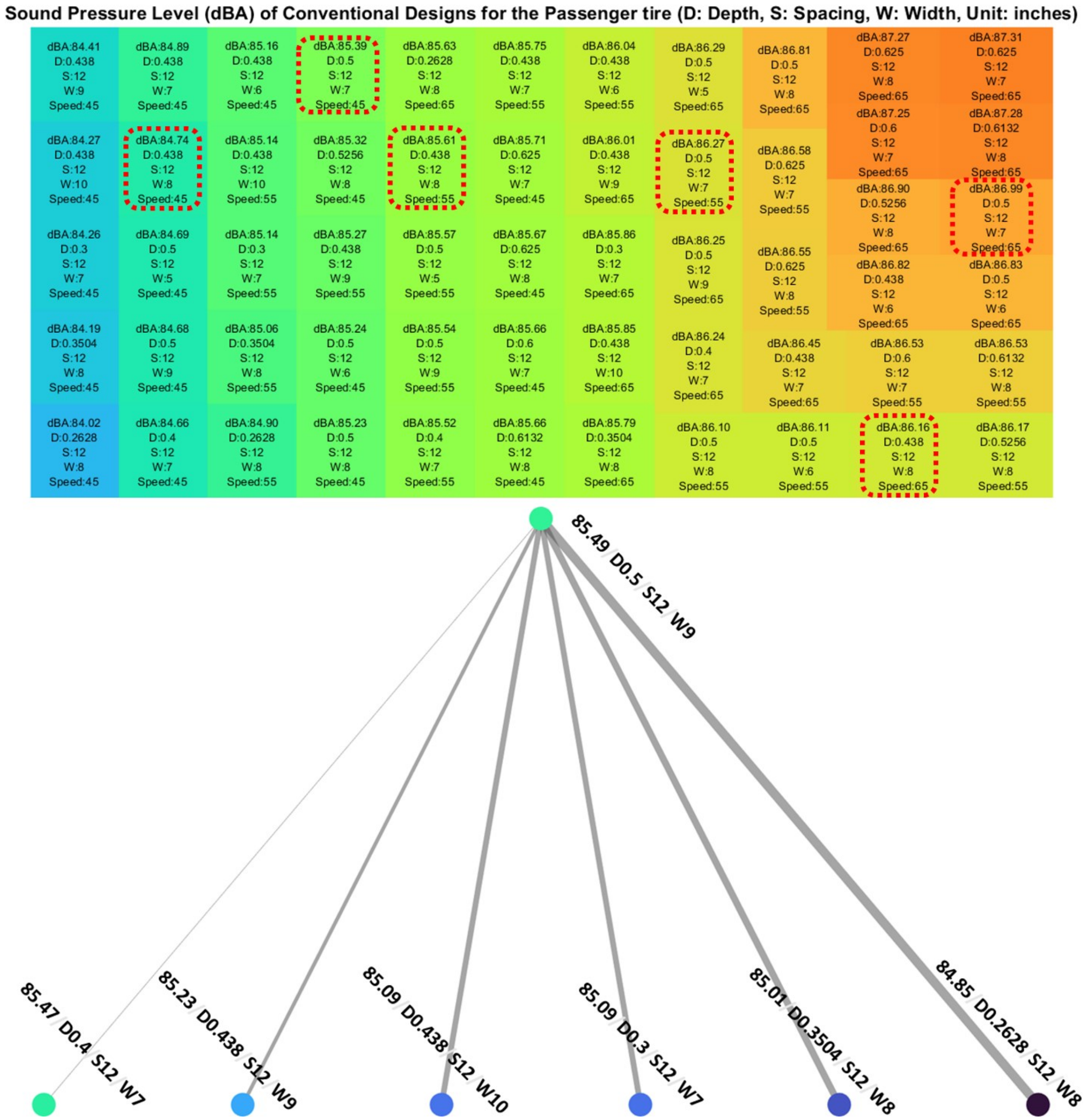

Figure 5.16: Heatmap visualization and tree visualization in passenger car tire over the chosen set of conventional designs for the dimensions listed in Table 5.2.

Next, we show the same visualizations for the truck tire.

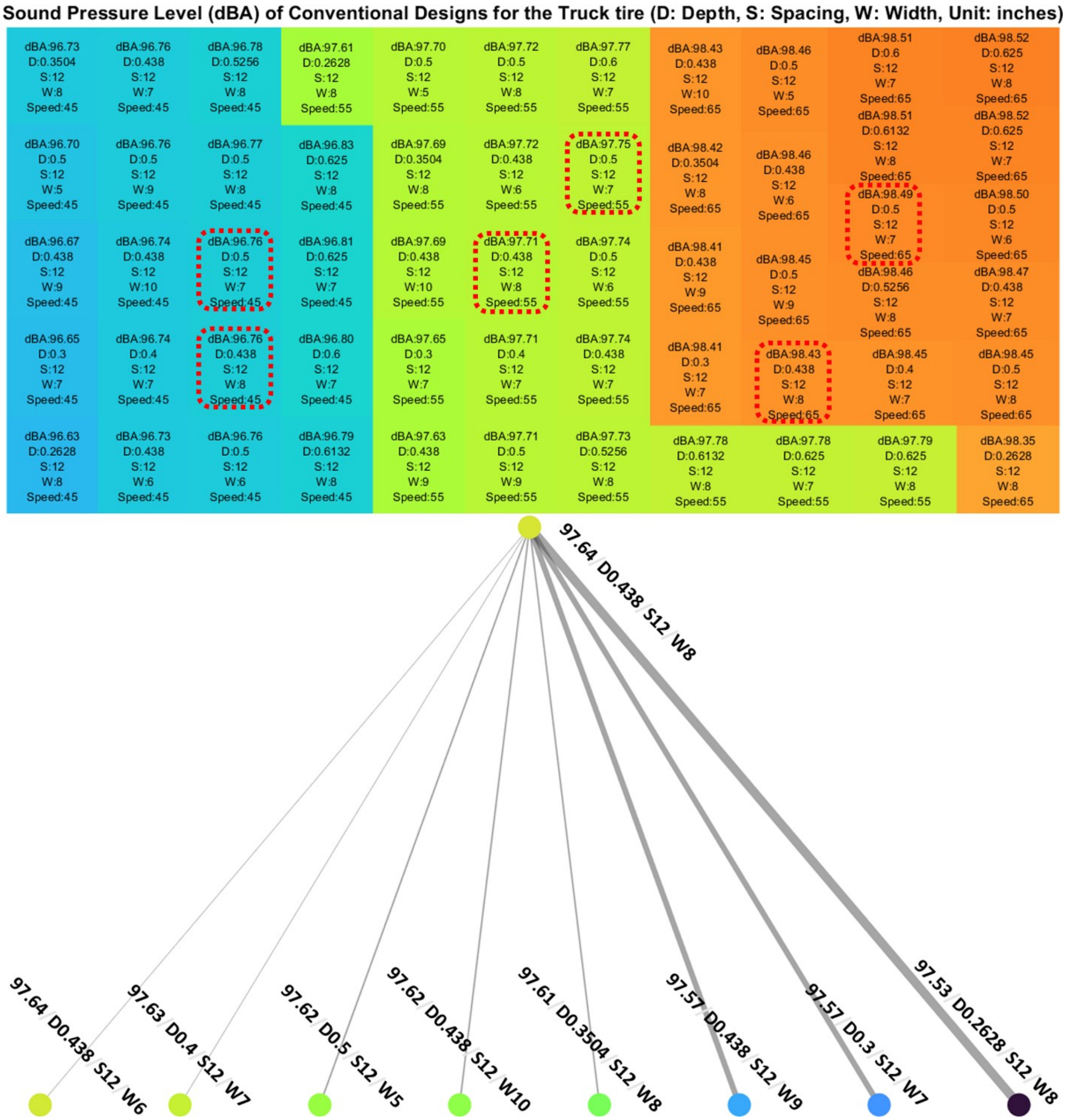

Figure 5.17: Heatmap visualization and tree visualization in truck tire over the chosen set of conventional designs for the dimensions listed in Table 5.2.

In this tree visualization, the leftmost node is slightly lower, by 0.01dBA, than the top node.

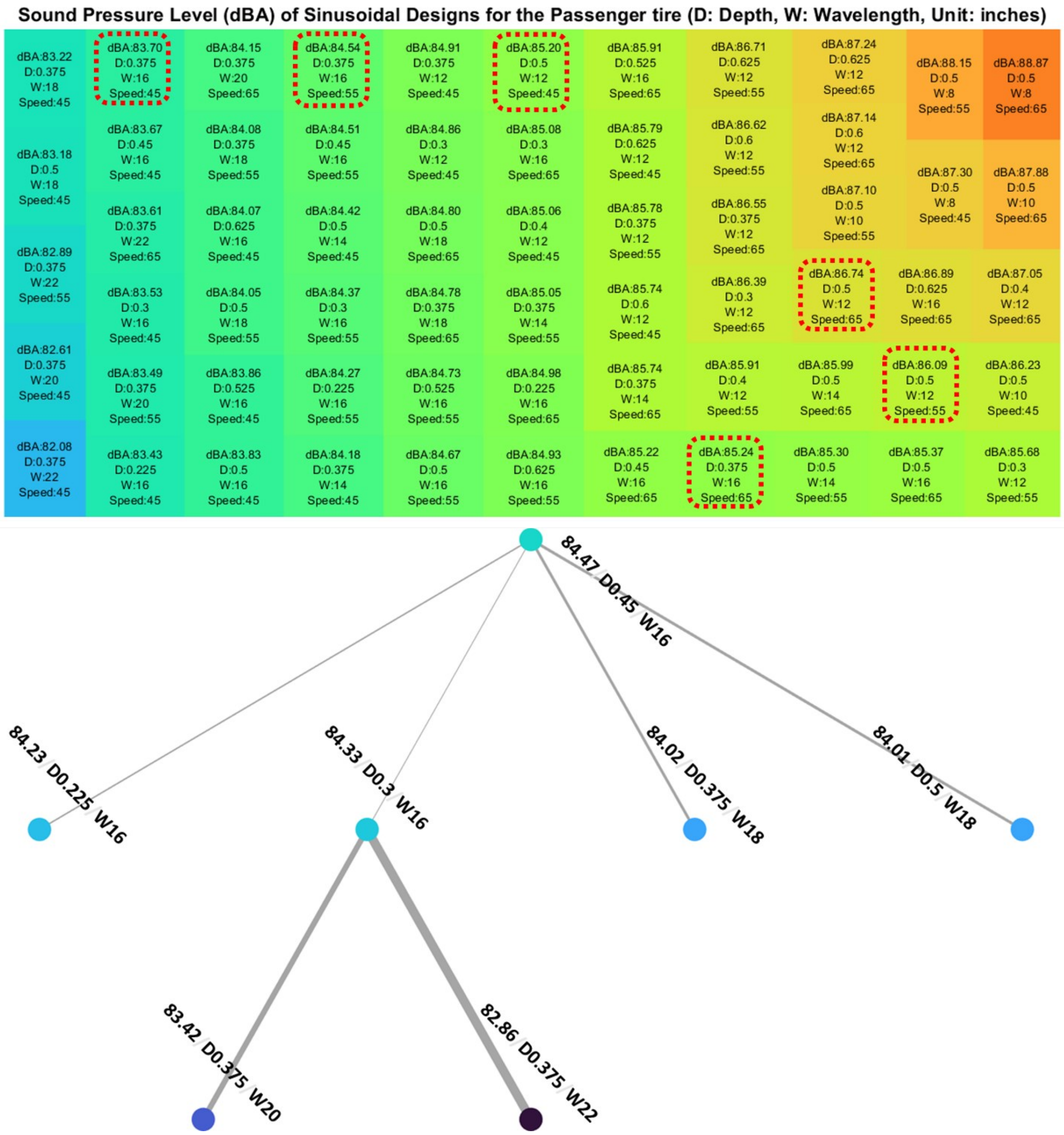

Figure 5.18: Heatmap visualization and tree visualization in passenger car tire over the chosen set of sinusoidal designs for the dimensions listed in Table 5.2.

Next, we show the same visualizations for the truck tire.

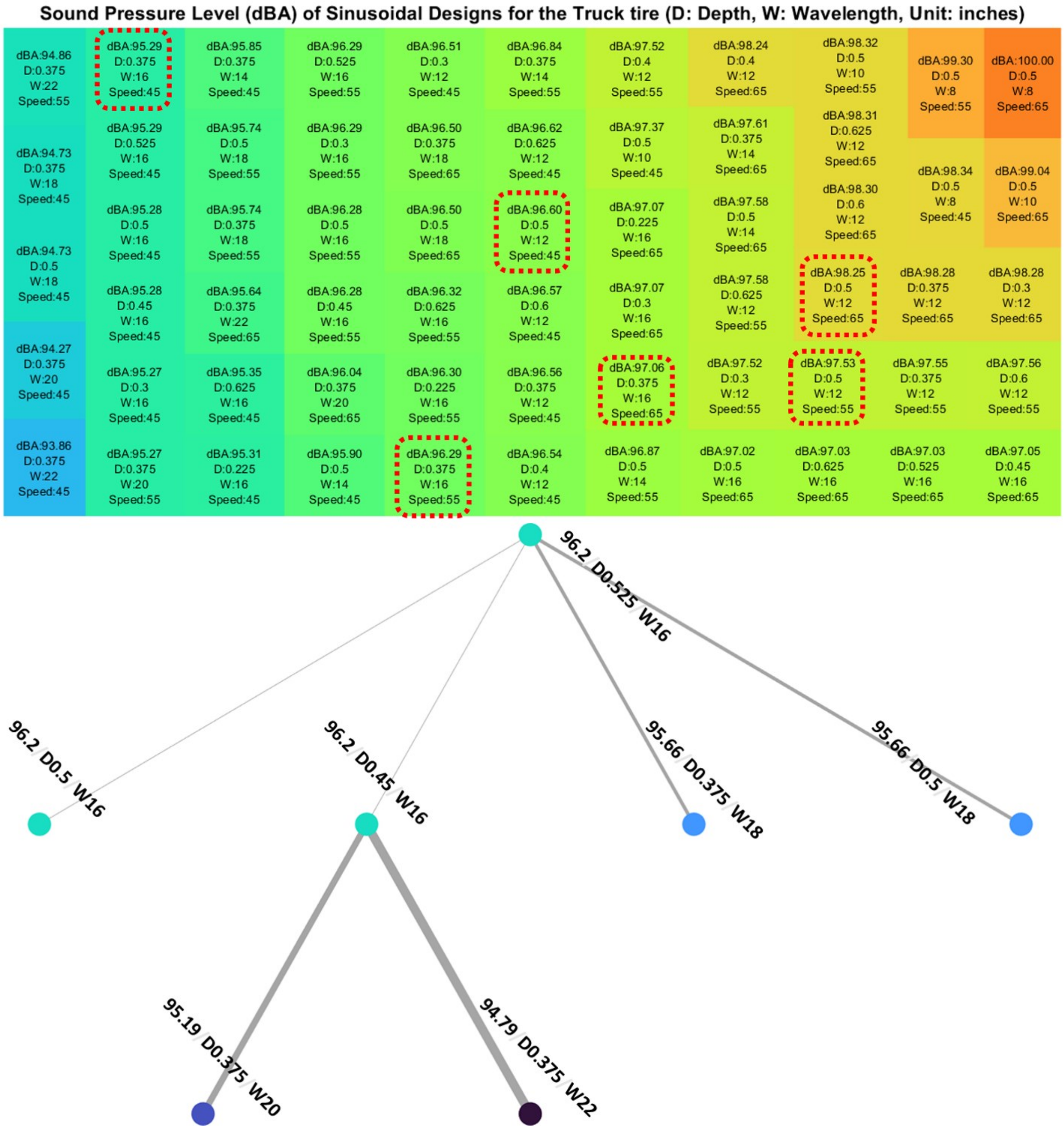

Figure 5.19: Heatmap visualization and tree visualization in truck tire over the chosen set of sinusoidal designs for the dimensions listed in Table 5.2.

We note that for conventional designs, the tree visualization shows two levels. The maximum SPL difference is around 0.64 dBA for the passenger car tire, and 0.11 dBA for the truck tire. Over our simulated sinusoidal designs, the tree visualization shows three levels of the SPL differences, and the maximum SPL difference is around 1.61 dBA for the passenger car tire, and 1.41 dBA for the truck tire. The different number of levels for the two designs demonstrates that choices over conventional dimensions will likely produce similar noise levels but different noise levels for the sinusoidal dimensions.

6.0 ADDITIONAL RESULTS: SPL COMPARISON FOR ZERO-DEGREE AND 10 DEGREES ANGLE OF LANDING

In this section, we examine the influence of rumble strips on the SPL outputs when the tire is rolling along the rumble strip at an angle. We have conducted simulations where the rumble strip has a 10 degrees angle of landing. In Section 5.0, we created the set of variations of the dimensions defined in ODOT/SPR800 and ODOT/TLM and we defined these variations in Table 5.2. Some of the dimensions have the lowest and highest depth, width/wavelength that can be implemented in practice. These dimensions are of interest in this section to contrast how the 10 degrees angle of landing differs from the zero-degree. We have selected the 4 cases that have the lowest and highest depth and width/wavelength from the variations to ODOT/SPR800 and similarly 4 cases from the variations to ODOT/TLM for each rumble strip design, i.e., conventional, and sinusoidal. For each case, we have simulated both passenger car and truck tires and included all three speeds: 45 mph, 55 mph, and 65 mph. Overall, we have simulated 96 scenarios. We only present visualizations for some of the simulated cases in the following sections.

In the next subsection, Section 6.1, we will show the displacement magnitude in the treads of the passenger car tire and the truck tire. In Figure 6.1 and Figure 6.2, we demonstrate how the landing at a non-zero angle creates asymmetric displacement distribution in the tire treads. After that, we will focus on demonstrating the contribution of the 10 degrees angle of landing on one single rumble strip dimension at a time for the passenger car tire and then for the truck tire, respectively. Through our simulations, we observe that the 10 degrees angle of landing influences the SPL outputs differently with respect to the dimensions of the rumble strip design, e.g., shallow vs. deep depth, in addition to the tire type. In Section 6.2, we focus on the passenger car tire as the changes to the truck tire are similar but less noticeable. In Section 6.2.1, we contrast a shallow and a deep groove for both the conventional and sinusoidal designs. In Section 6.2.2, we show a low width and a high width comparison for one conventional design dimension, which is one of the 4 cases selected for this section. In Section 6.2.3, we show a low wavelength and a high wavelength comparison for one sinusoidal design dimension. In Section 6.3, we evaluate the differences between the zero-degree and the 10 degrees angle of landing in the SPL outputs for the 96 scenarios for both the passenger car tire and the truck tire. The displacement in the tire is evaluated in the following three directions: rolling, lateral, and loading. We show how the air cavity is influenced by the 10 degrees angle of landing at the beginning of this section. We use just one rumble strip dimension, and one tire at one speed to illustrate the change incurred. The latter part of this section provides a summary over the chosen sets of highest and lowest depth and width/wavelength.

6.1 DISPLACEMENT MAGNITUDE COMPARISON IN THE TREADS OF THE PASSENGER CAR TIRE AND TRUCK TIRE

In Figure 6.1, we compare the zero-degree angle of landing (left) and the 10 degrees angle of landing (right) for the passenger car tire. The first row shows the tire contacting the rumble strips and the bottom row shows the displacement magnitude, i.e., a combination of the displacement in the rolling, lateral, and loading directions, of the tread. We note the high displacement regions, colored from yellow to red colors, have different sizes and shapes, and using this information we conclude that the contact areas are different for these two landings. In the subsequent sections, we term contact areas as the regions of the high displacements, i.e., the warm colored portions at the contact areas between the tires and the rumble strips.

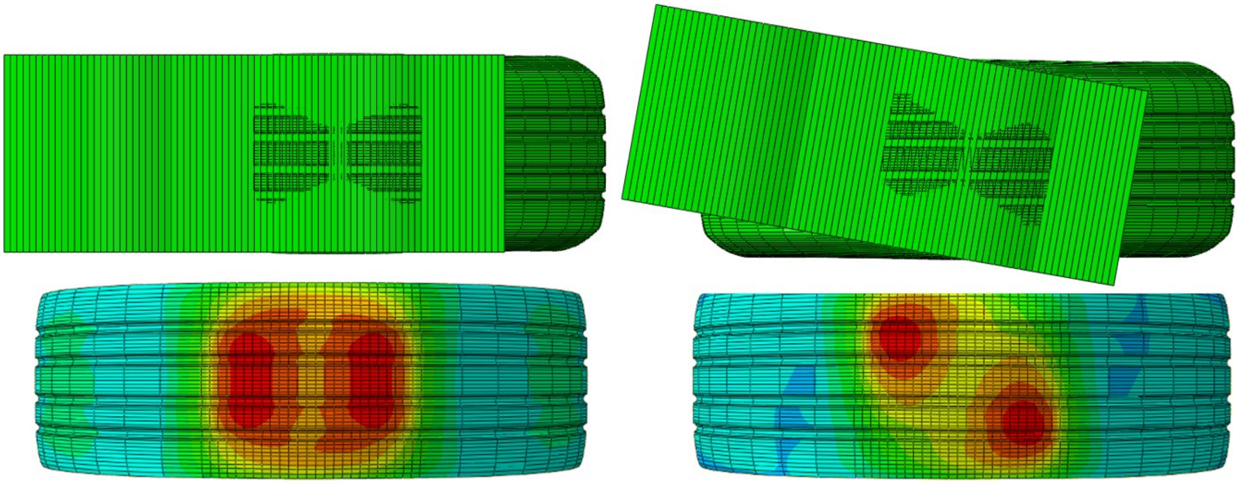

Figure 6.1: Displacement magnitude comparison for passenger car tire tread. Zero-degree (left) and 10 degrees (right).

We note that at the chosen rumble strip dimensions the high displacement regions can be disjointed. The 10 degrees angle of landing creates a more disjoint warm color region. We project the air displacements will be more non-uniform than that for the zero-degree angle of landing.

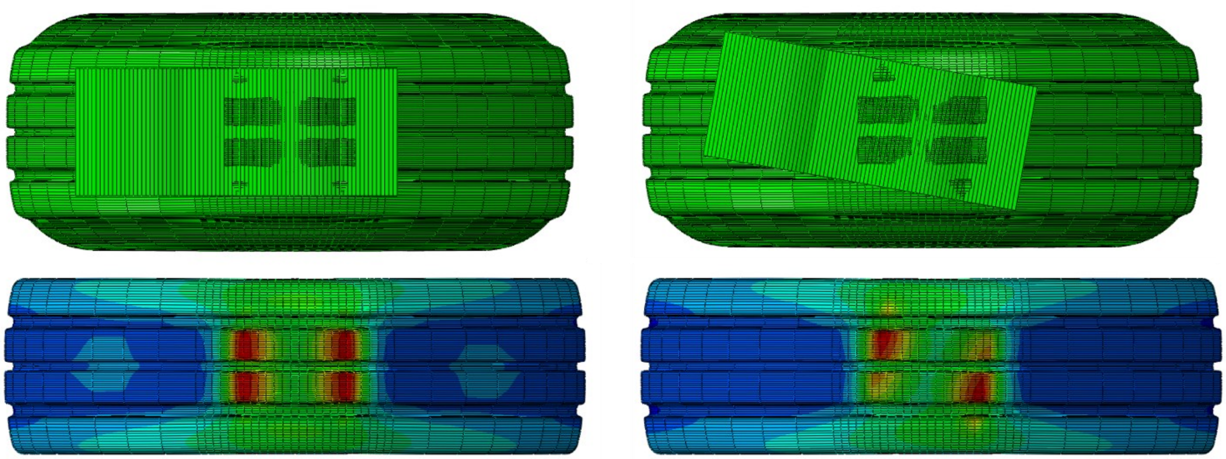

Figure 6.2: Displacement magnitude comparison for truck tire tread. Zero-degree (left) and 10 degrees (right).

In Figure 6.2, we show the zero-degree angle of landing (left), and the 10 degrees angle of landing (right) for the truck tire. We note the high displacement regions have different sizes and shapes, and at the chosen dimensions, the high displacement regions are also disconnected. The 10 degrees angle of landing creates an asymmetric distribution, i.e., the red regions are not symmetric about the shoulder-to-shoulder axis of the tread.

6.2 CONTACT AREA COMPARISON OF DIMENSIONS FOR 10 DEGREES ANGLE OF LANDING

In this subsection, we visualize the high displacement regions in the contact areas for the passenger car tire under 10 degrees angle of landing.

6.2.1 Shallow and deep grooves under 10 degrees angle of landing

Figure 6.3 presents two depths: 0.2826 inches (left) and 0.625 inches (right). This design dimension has a length of 9.5 inches and a width of 8 inches. We display the tire treads. Both contact areas, warm colored regions, are slanted with respect to the rolling direction as expected. The shallow groove (left) has a higher value and a larger connected region than the deep groove (right), which has two disconnected regions.

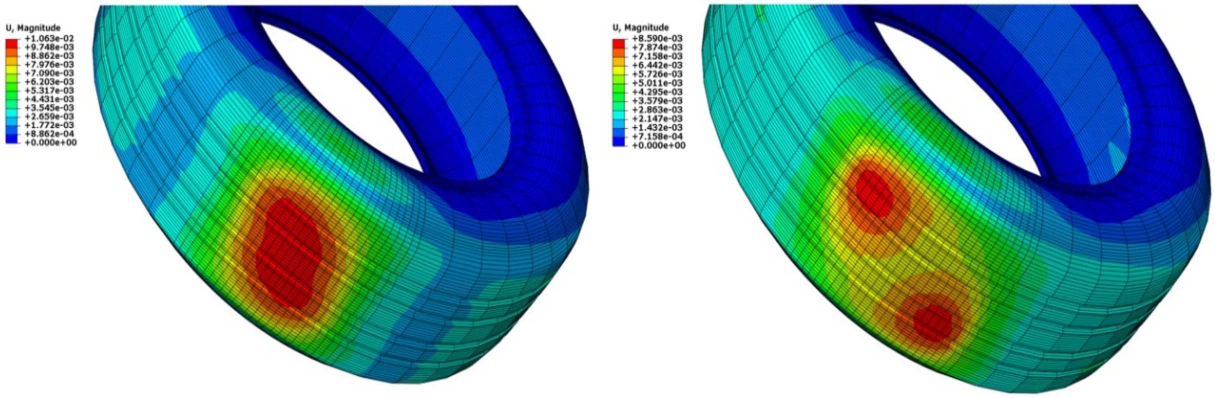

Figure 6.3: Displacement magnitude comparison of the passenger car tire for one conventional design at two different depths.

Next, we examine the tread deformation over sinusoidal designs. Figure 6.4 shows again for the same tire over one sinusoidal design dimension at depths of 0.225 inches (left) and 0.625 inches (right). This sinusoidal design dimension has a length of 14 inches and a wavelength of 16 inches. For this design, we note the shallow groove creates a smaller but with a higher value warm color region than the deep groove. Contrary to the conventional design in Figure 6.3, the high displacement regions are connected at the deep groove revealing the effect of the rounded wavy profile of the sinusoidal design.

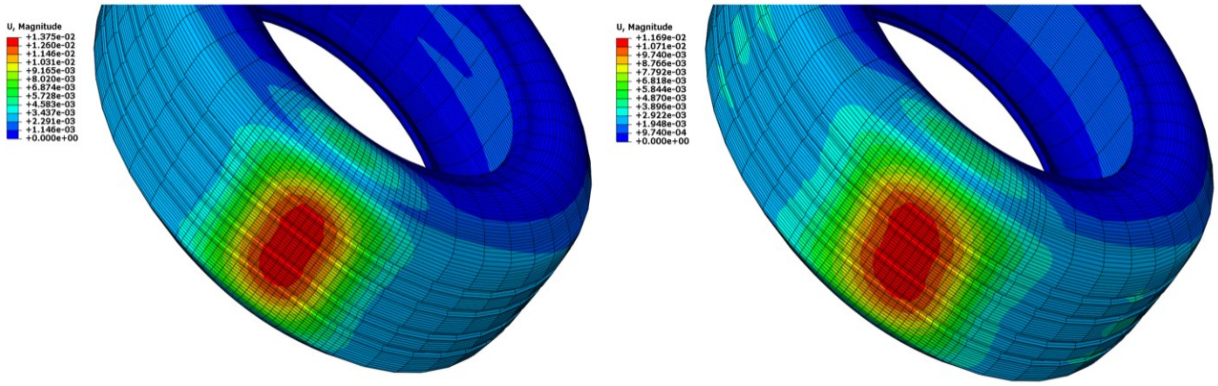

Figure 6.4: Displacement magnitude comparison of the passenger car tire for one sinusoidal design at two different depths.

6.2.2 Short and long widths of conventional design under 10 degrees angle of landing

In this subsection, we focus on conventional designs for the same passenger car tire. Figure 6.5 shows widths: 6 inches (left) and 10 inches (right). This conventional design dimension has a length of 9.5 inches and a depth of 0.438 inches. The short width has a similar effect as the deep groove in the previous subsection (Figure 6.3) and incurs two disjointed high displacement regions, i.e., warm color regions. The long width is in full contact with the tire and incurs a higher displacement magnitude.

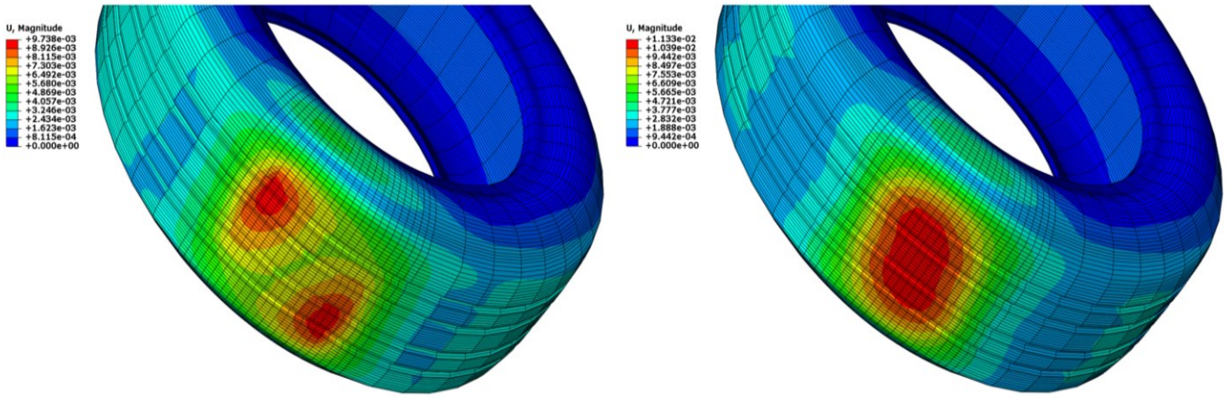

Figure 6.5: Displacement magnitude comparison of the passenger car tire for one conventional design at two different widths.

6.2.3 Short and long wavelengths of sinusoidal design under 10 degrees angle of landing

Next, we focus on sinusoidal designs for the same passenger car tire. Figure 6.6 presents two different wavelengths: 12 inches (left) and 22 inches (right). This sinusoidal design dimension has a length of 14 inches and a depth of 0.375 inches. Both displacement magnitudes have connected regions in the contact areas. The short wavelength has a smaller high displacement region at a slightly higher magnitude. The long wavelength is closer to being flat and incurs a larger high displacement region. There are no disconnected warm colored regions as seen from conventional designs.

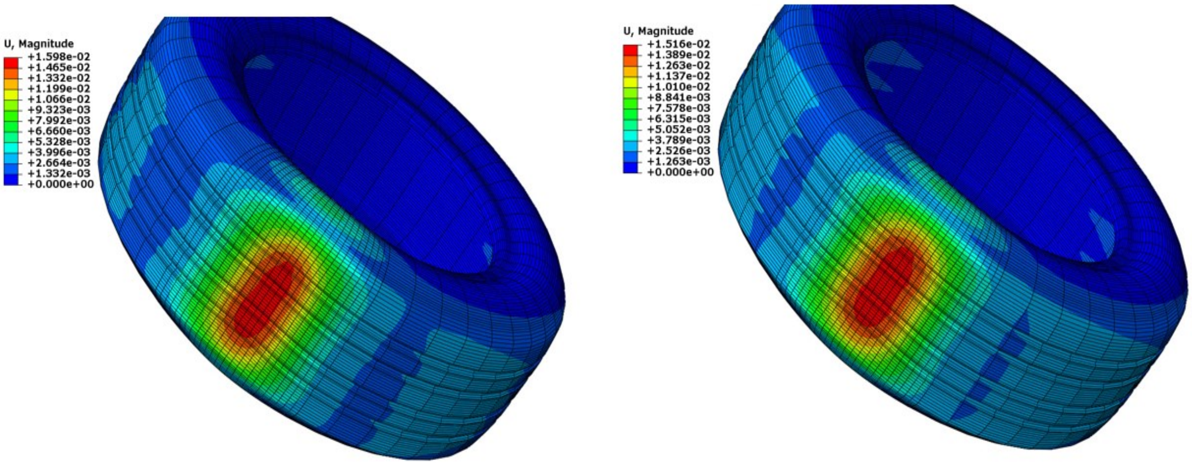

Figure 6.6: Displacement magnitude comparison of the passenger car tire for one sinusoidal design at two different wavelengths.

These displacement results indicate that the 10 degrees angle of landing is also sensitive to the depth, width, and wavelength variation in the rumble strip designs just like the zero-degree landing. In the next section, we examine the acoustic effects of the passenger car tire and truck tire caused by the contact areas of different depths, widths, and wavelengths for both conventional and sinusoidal designs. We continue to include the different speeds.

6.3 SPL COMPARISON OF DIMENSIONS FOR ZERO-DEGREE AND 10 DEGREES ANGLE OF LANDING

To determine whether the 10 degrees angle of landing produces a higher noise level, we compare it to the results from the zero-degree angle of landing. The geometric dimensions of the conventional and sinusoidal rumble strips are in Table 6.1 and Table 6.2, respectively.

Table 6.1: Geometric Dimensions of the Chosen set of Conventional Designs for the Angle of Landing Simulations.

L (inches)	W (inches)	D (inches)	S/W (inches)	Landing(degrees)	Type
9.5	8	0.2628	12	0, 10	Conventional
9.5	8	0.625	12	0, 10	Conventional
9.5	6	0.438	12	0, 10	Conventional
9.5	10	0.438	12	0, 10	Conventional
8	7	0.3	12	0, 10	Conventional
8	7	0.625	12	0, 10	Conventional
8	5	0.5	12	0, 10	Conventional
8	9	0.5	12	0, 10	Conventional

Table 6.2: Geometric Dimensions of the Chosen set of Sinusoidal Designs for the Angle of Landing Simulations.

L (inches)	W (inches)	D (inches)	S/W (inches)	Landing(degrees)	Type
14	N/A	0.225	16	0, 10	Sinusoidal
14	N/A	0.625	16	0, 10	Sinusoidal
14	N/A	0.375	12	0, 10	Sinusoidal
14	N/A	0.375	22	0, 10	Sinusoidal
8	N/A	0.3	12	0, 10	Sinusoidal
8	N/A	0.625	12	0, 10	Sinusoidal
8	N/A	0.5	8	0, 10	Sinusoidal
8	N/A	0.5	18	0, 10	Sinusoidal

We have chosen one representative design from a set of simulations of different designs to visualize the air displacements in the rolling, lateral, and loading directions of the tires. We include zero-degree and 10 degrees angle of landing side by side in our figures. We summarize all the results in Table 6.3 for passenger car tires over conventional designs, Table 6.4 for truck tires over conventional designs, Table 6.5 for passenger car tires over sinusoidal designs, and Table 6.6 for truck tires over sinusoidal designs.

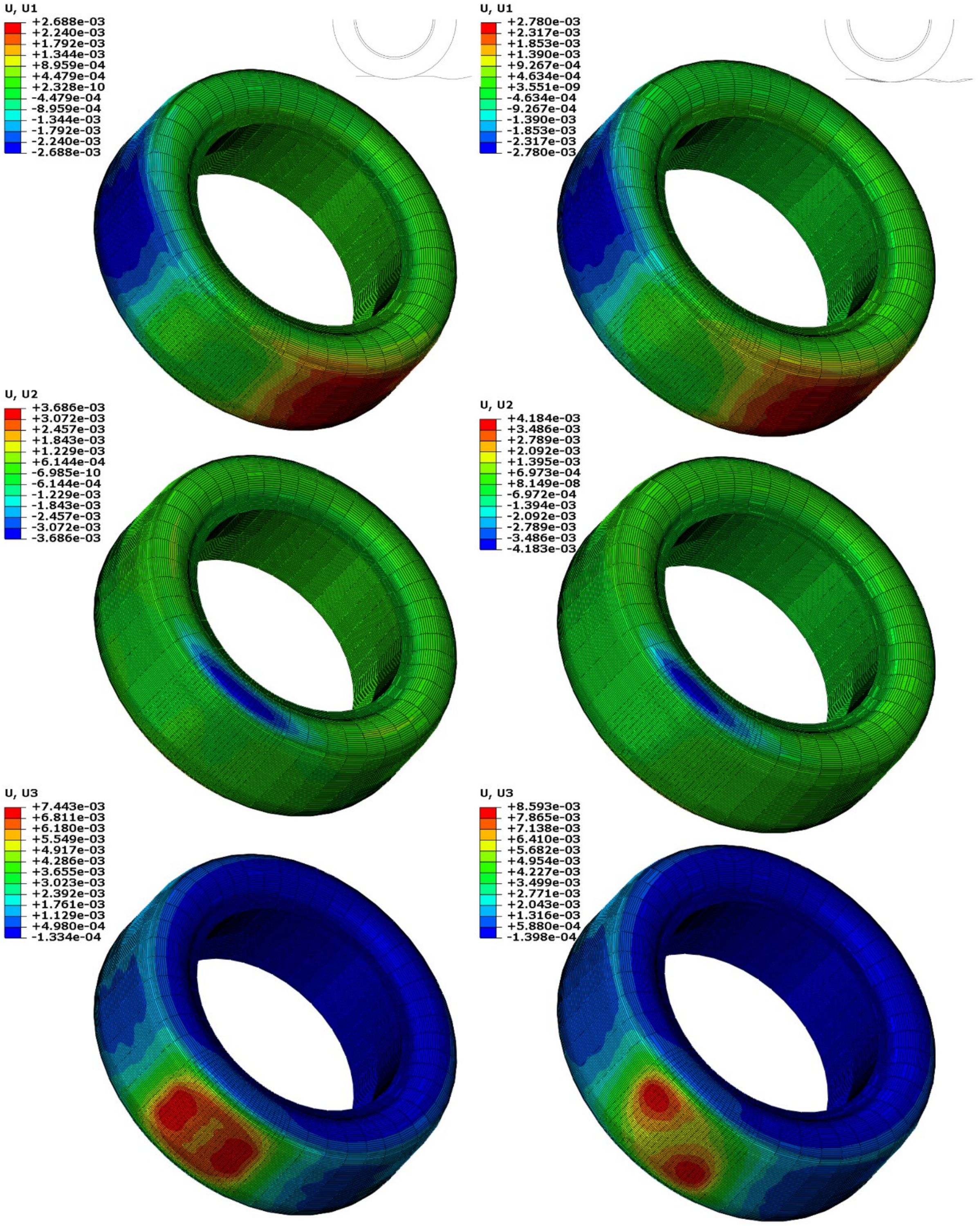

Figure 6.7: Air displacements in rolling, lateral, and loading directions for the passenger car. The top row shows the rolling direction, the middle row shows the lateral direction, and the bottom row shows the loading direction. Zero-degree (left) and 10 degrees (right) angle of landing.

In Figure 6.7, we show the displacements in the air cavity of the passenger car tire when rolling over the conventional design at 0.625 inches depth, 8 inches width, and 12 inches spacing. In the rolling direction, both zero-degree and 10 degrees have a similar distribution of high (red) and low (blue) values; however, the 10 degrees angle of landing has a higher value than the zero-degree. For this lateral direction, we note that both zero-degree and 10 degrees have regions that are caving inward (blue color). The zero-degree has a larger region but at a smaller value than the 10 degrees. In the loading direction, the displacement area of zero-degree is symmetric. However, the 10 degrees has a more disjointed displacement (red) region and higher magnitude than the zero-degree. The asymmetric disjointed displacement area is due to the tire contacting the rumble strip at a non-zero angle.

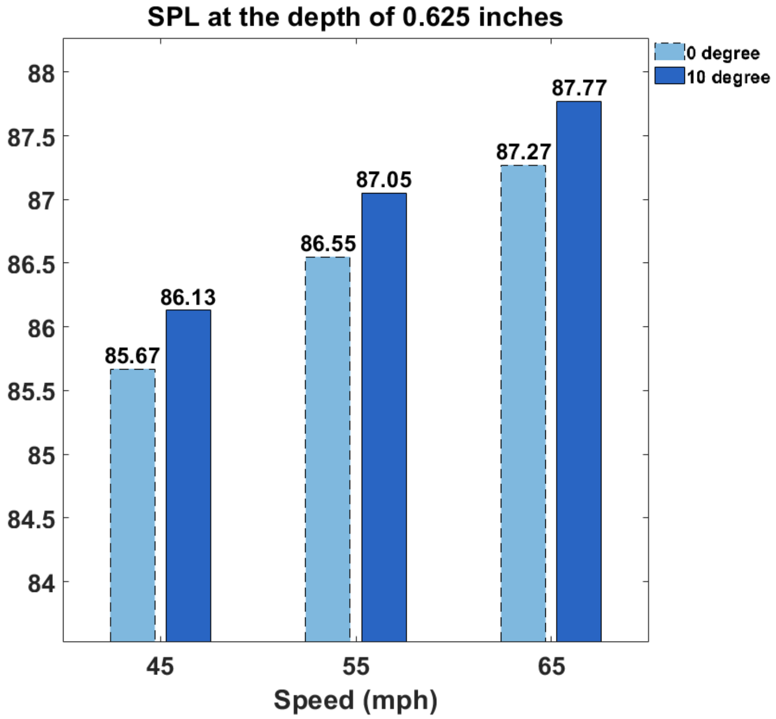

Figure 6.8: Passenger car tire SPL differences of the angle of landing for one conventional design dimension.

By comparing the SPL outputs in Figure 6.8, we observe that the 10 degrees angle of landing has a higher SPL than the zero-degree angle of landing at all speeds. The SPL of 10 degrees is also increasing with the increasing speed like the zero-degree angle of landing. The SPL difference at 55 mph and 65 mph is slightly higher than that at 45 mph. Thus, we conclude this difference is consistent over the speeds for this rumble strip dimension.

Next, we compare the same conventional design dimension for the truck tire. Figure 6.9 shows that in the rolling and lateral directions, both zero-degree and 10 degrees have a similar distribution of high (red) and low (blue) values, and the 10 degrees has a higher value than the zero-degree. In the loading direction, the 10 degrees has an asymmetric pattern (red) caused by the tire contacting the rumble strip at a non-zero angle and has a higher value than the zero-degree. The zero-degree also has a disjointed red region, and it is more connected than the 10 degrees.

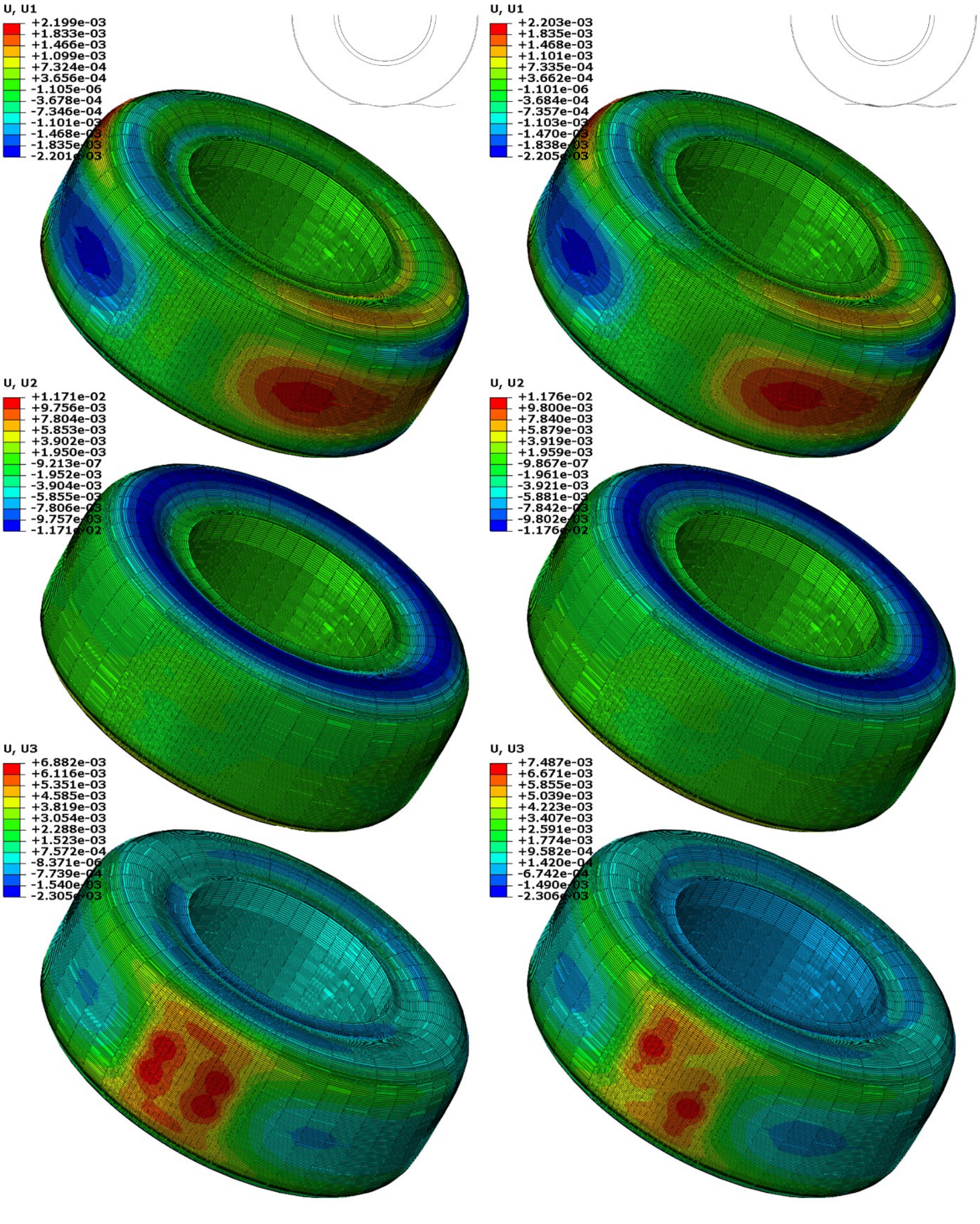

Figure 6.9: Air displacements in rolling, lateral, and loading directions for the truck tire. The top row shows the rolling direction, the middle row shows the lateral direction, and the bottom row shows the loading direction. Zero-degree (left) and 10 degrees (right) angle of landing.

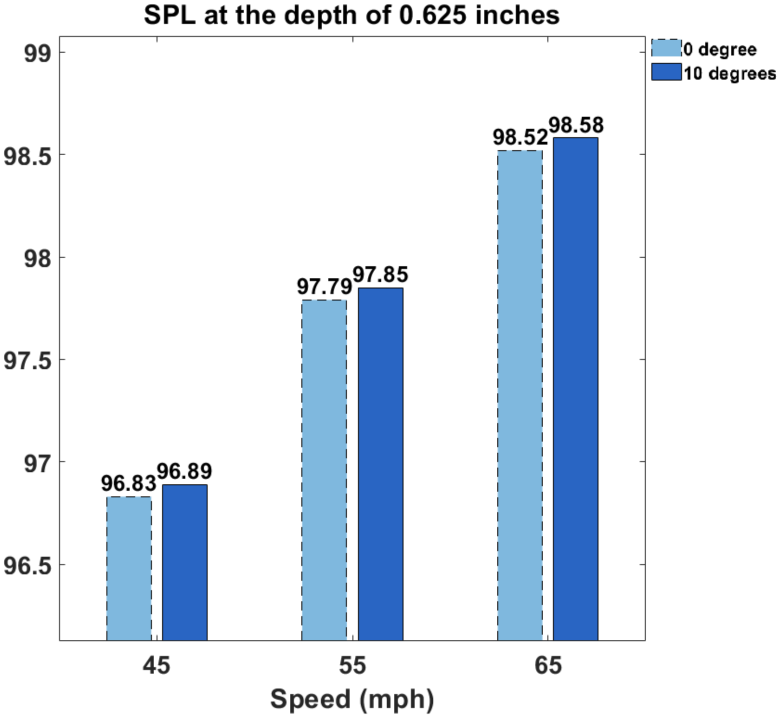

Figure 6.10: Truck tire SPL differences of the angle of landing for one conventional design dimension.

As we observe from Figure 6.8 for the passenger car tire, the 10 degrees angle of landing has a higher value in air displacements than the zero-degree, as shown in Figure 6.10. However, the differences between the zero-degree and 10 degrees are much smaller than the corresponding passenger car tire measurements shown in Figure 6.8. The SPL differences at 45 mph, 55 mph, and 65 mph are all 0.06 dBA. This is expected due to the truck tire being more rigid and conforming to the rumble strips less than the car tire. Furthermore, the rumble strips at the given lengths from ODOT/TLM and ODOT/SPR800 are partially covered by the truck tire that we have purchased.

Next, we examine the sinusoidal design at a depth of 0.625 inches, and a wavelength of 16 inches. Figure 6.11 shows the passenger car tire SPL differences between the zero-degree and 10 degrees angle of landing. By comparing the magnitude of air displacement, we note that the zero-degree has a smaller value than the 10 degrees in the rolling and loading directions but has a higher value in the lateral direction. There are no disconnected high displacement regions, i.e., disconnected red regions, again revealing the effect of smooth and wavy sinusoidal designs.

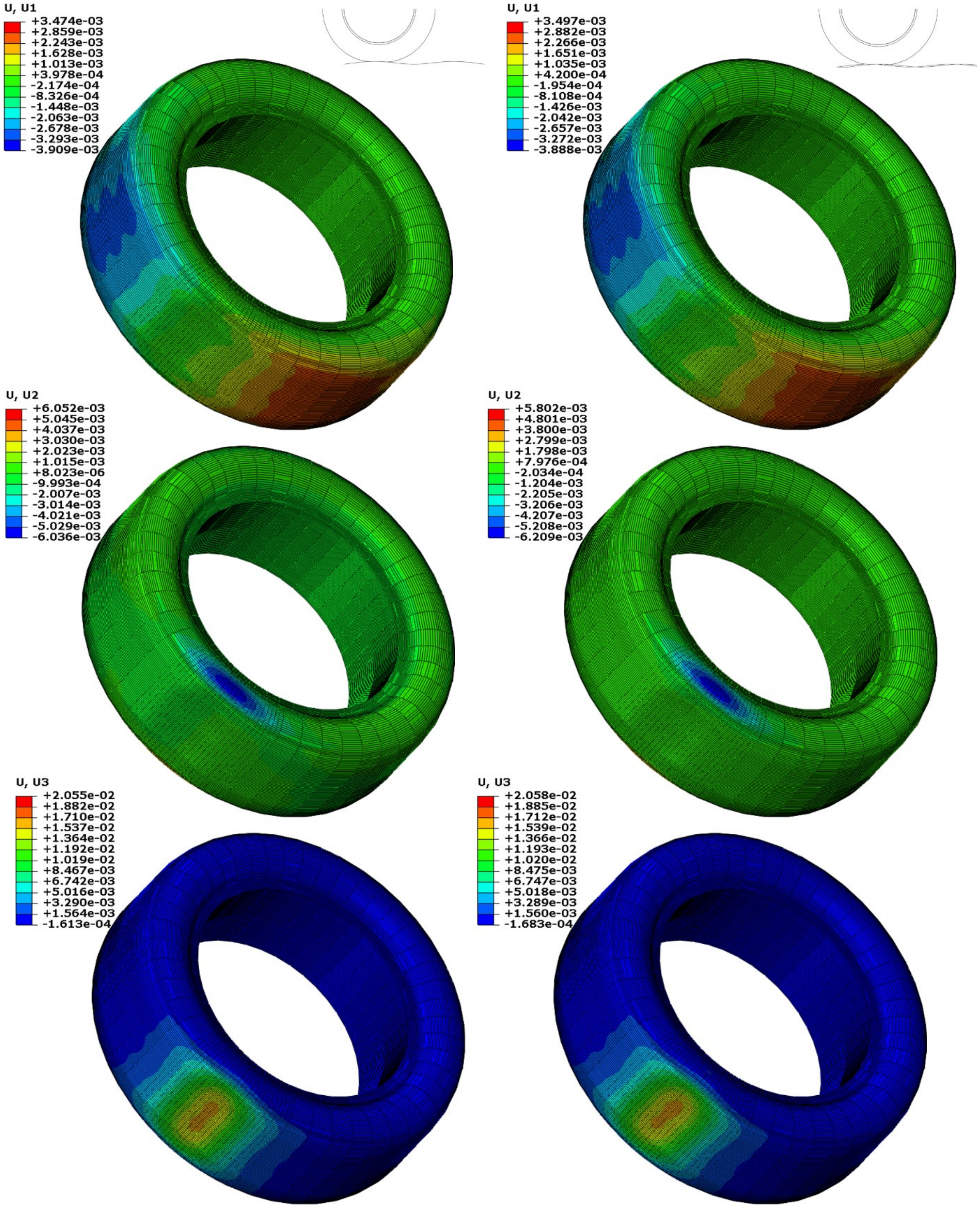

Figure 6.11: Air displacements in rolling, lateral, and loading directions for the passenger car tire. The top row shows the rolling direction, the middle row shows the lateral direction and the bottom row shows the loading direction. Zero-degree (left) and 10 degrees (right) angle of landing.

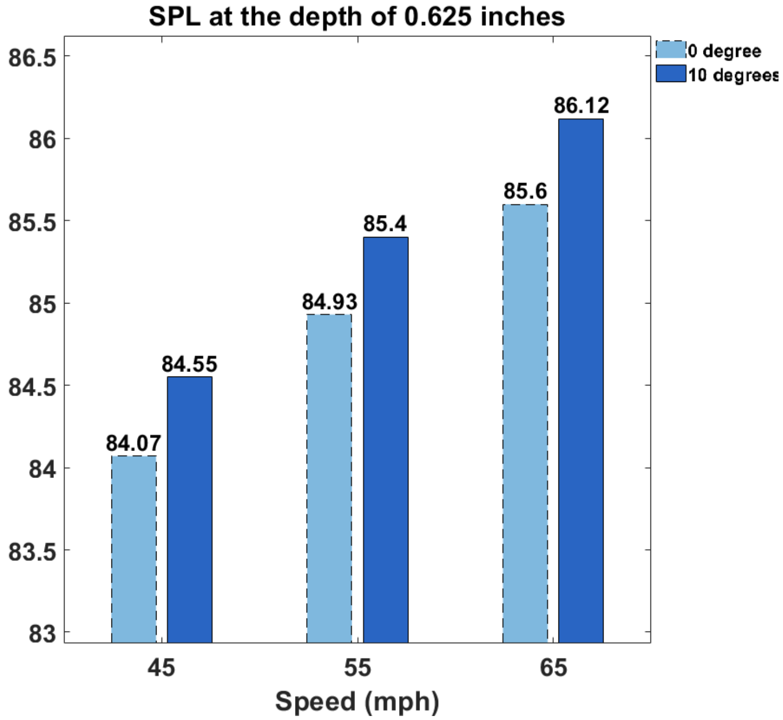

Figure 6.12: Passenger car tire SPL differences of the angle of the landing for one sinusoidal design dimension.

From the SPL outputs in Figure 6.12, we observe that the 10 degrees angle of landing has a higher SPL than the zero-degree angle of landing at all speeds. The SPL of 10 degrees is also increasing with the increasing speed like the zero-degree angle of landing. The SPL differences are around 0.5 dBA for all three speeds.

We examine the same sinusoidal design dimension for the truck tire. In the rolling and lateral direction, the zero-degree has a slightly higher value than the 10 degrees but is lower in the loading direction. Both zero-degree and 10 degrees have a similar distribution of high (red) and low (blue) values in all directions.

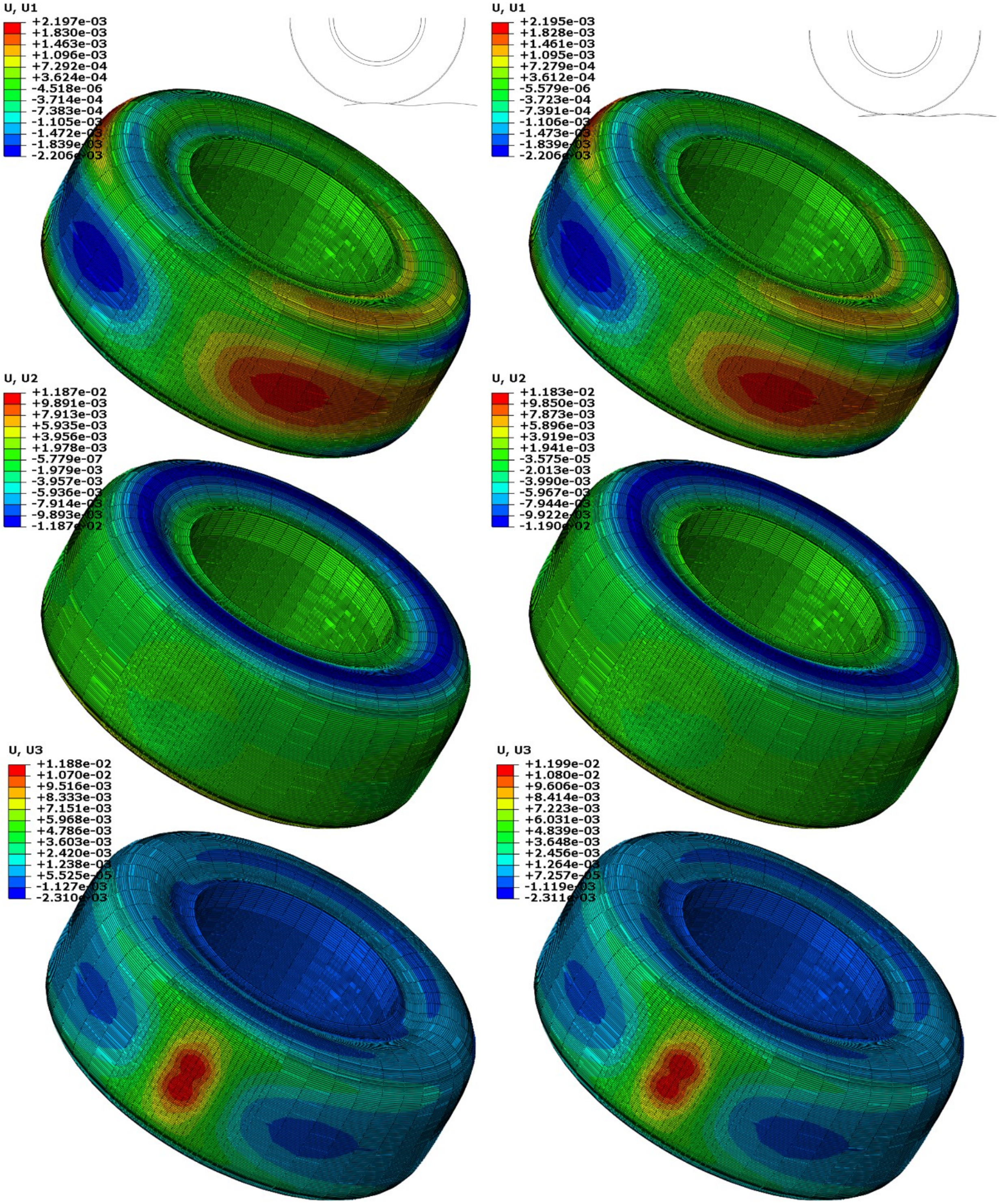

Figure 6.13: Air displacements in rolling, lateral, and loading directions for the truck tire. The top row shows the rolling direction, the middle row shows the lateral direction, and the bottom row shows the loading direction. Zero-degree (left) and 10 degrees (right) angle of landing.

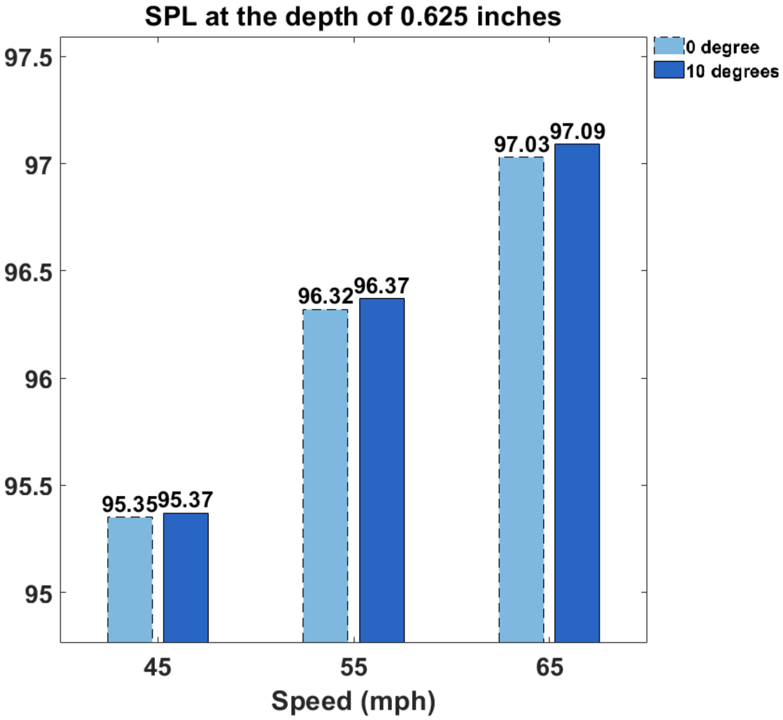

Figure 6.14: Truck tire SPL differences of the angle of the landing for one sinusoidal design dimension.

In Figure 6.14, we show that the 10 degrees angle of landing has a slightly higher SPL than the zero-degree angle of landing at all speeds. More specifically, the SPL difference at 45 mph is 0.02 dBA, at 55 mph is 0.05 and at 65 mph is 0.06 dBA, which is one magnitude lower than the SPL difference for the passenger car tire.

Next, we summarize all the cases that we have simulated to evaluate the 10 degrees angle of landing. We organize the cases over rumble strip designs and tires. The cases that have been visualized in earlier subsections have been marked with a dashed boundary. We first show the SPL differences for conventional designs at speeds of 45 mph, 55 mph, and 65 mph: Table 6.3 for passenger car tires and Table 6.4 for truck tires. Next, we show the SPL differences for the sinusoidal design at the same speeds: Table 6.5 for the passenger car tire and Table 6.6 for the truck tire.

Table 6.3: Passenger Car Tire SPL Differences for the chosen set of Conventional Designs

Dimension	45 mph	55 mph	65 mph
D: 0.2628 W: 8 S: 12 L: 9.5	0.40	0.41	0.43
D: 0.625 W: 8 S: 12 L: 9.5	0.46	0.50	0.50
D: 0.3 W: 7 S: 12 L: 8	0.05	0.03	0.02
D: 0.625 W: 7 S: 12 L: 8	0.36	0.39	0.40
D: 0.438 W: 6 S: 12 L: 9.5	0.33	0.32	0.33
D: 0.438 W: 10 S: 12 L: 9.5	0.21	0.22	0.29
D: 0.5 W: 5 S: 12 L: 8	0.21	0.23	0.25
D: 0.5 W: 9 S: 12 L: 8	0.46	0.48	0.51

Note: For the three vehicle speeds, the SPL differences (dBA) between zero-degree and 10 degrees angle of landing are calculated for the dimensions listed here and also in Table 6.1.

Table 6.4: Truck Tire SPL Differences for the chosen set of Conventional Designs

Dimension	45 mph	55 mph	65 mph
D: 0.2628 W: 8 S: 12 L: 9.5	0.14	0.13	0.12
D: 0.625 W: 8 S: 12 L: 9.5	0.06	0.06	0.06
D: 0.3 W: 7 S: 12 L: 8	0.07	0.04	0.02
D: 0.625 W: 7 S: 12 L: 8	0.06	0.07	0.06
D: 0.438 W: 6 S: 12 L: 9.5	0.03	0.04	0.06
D: 0.438 W: 10 S: 12 L: 9.5	0.03	0.01	0.02
D: 0.5 W: 5 S: 12 L: 8	0.10	0.07	0.08
D: 0.5 W: 9 S: 12 L: 8	0.04	0.06	0.05

Note: For the three vehicle speeds, the SPL differences (dBA) between zero-degree and 10 degrees angle of landing are calculated for the dimensions listed here and also in Table 6.1.

Table 6.5 Passenger Car Tire SPL Differences for the chosen set of Sinusoidal Designs

Dimension	45 mph	55 mph	65 mph
D: 0.225 W: 16 L: 14	0.21	0.26	0.28
D: 0.625 W: 16 L: 14	0.48	0.47	0.52
D: 0.3 W: 12 L: 8	0.20	0.23	0.23
D: 0.625 W: 12 L: 8	0.38	0.38	0.54
D: 0.375 W: 12 L: 14	0.14	0.16	0.15
D: 0.375 W: 22 L: 14	0.32	0.36	0.36
D: 0.5 W: 8 L: 8	0.08	0.13	1.64
D: 0.5 W: 18 L: 8	0.49	0.46	0.44

Note: For the three vehicle speeds, the SPL differences (dBA) between zero-degree and 10 degrees angle of landing are calculated for the dimensions listed here and also in Table 6.2.

Table 6.6 Truck Tire SPL Differences for the chosen set of Sinusoidal Designs

Dimension	45 mph	55 mph	65 mph
D: 0.225 W: 16 L: 14	0.05	0.00	0.00
D: 0.625 W: 16 L: 14	0.02	0.05	0.06
D: 0.3 W: 12 L: 8	0.14	0.11	0.08
D: 0.625 W: 12 L: 8	0.14	0.04	0.01
D: 0.375 W: 12 L: 14	0.00	0.03	0.04
D: 0.375 W: 22 L: 14	0.02	0.01	0.01
D: 0.5 W: 8 L: 8	0.11	0.11	0.07
D: 0.5 W: 18 L: 8	0.08	0.05	0.02

Note: For the three vehicle speeds, the SPL differences (dBA) between zero-degree and 10 degrees angle of landing are calculated for the dimensions listed here and also in Table 6.2.

From these tables, we observe that in general, the SPL responses under the 10 degrees angle of landing are higher than those under zero-degree. There are 10 exceptions among that 96 cases simulated, except for the 10 cases shown in Table 6.3, Table 6.4, and Table 6.6. For these 10 cases, seven of them are for the truck tire, and the average SPL difference is 0.025 dBA. In addition, the truck tire SPL difference is lower than the passenger car tire SPL difference.

Among the chosen set of conventional designs, the average SPL difference for the shallow groove (0.17 dBA) is lower than that for the deep groove (0.25 dBA). The average SPL difference for the short width (0.16 dBA) is also lower than the long width (0.20 dBA). This implies that the deep groove and long width can be slightly more sensitive to the 10 degrees angle of landing.

Among the chosen set of sinusoidal designs, the average SPL difference for the shallow groove (0.15 dBA) is lower than that for the deep groove (0.26 dBA). This implies that the deep groove can be slightly more sensitive to the 10 degrees angle of landing.

7.0 CONCLUSIONS AND LIMITATIONS

In this report, we utilized finite element simulations to estimate the tire noise produced by the interaction between the tires and rumble strips. Our results can facilitate finding a geometric design of rumble strip that meets a desired sound pressure level (SPL) numerically. Through our experiments and analyses, we observe trends known from existing literature regarding the depth and width/wavelength change in the rumble strips. We have examined three families of rumble strip designs: conventional, sinusoidal, and sawtooth. We have tested two tires: passenger car tire and truck tire at three speeds: 45 mph, 55 mph, and 65 mph. We have conducted over 276 experiments to ensure successful simulations and to examine different rumble strip designs. Among our experiments, there are 114 simulations on conventional designs, 126 on sinusoidal designs, and 36 on sawtooth designs.

Our simulated results agree in general with roadside measurements from the CalTrans/CTHWANP-RT-18-365.01.2 report and ODOT/SPR800 report for the dimensions used in our verification study. For conventional designs, we observe low SPLs for shallow designs. In particular, the dimension with a depth of 0.2628 inches and a spacing of 12 inches produces the lowest SPL among the 19 conventional design dimensions that we have simulated. For sinusoidal designs, we observe low SPLs when the wavelength is long, or the depth is low as expected. In particular, for the dimension with a wavelength of 22 inches and a depth of 0.375 inches, the SPL is the lowest among the 21 sinusoidal dimensions that we have simulated. Using the depth and wavelength values of the sinusoidal dimension from ODOT/SPR800 report (a wavelength of 16 inches and a depth of 0.375 inches), sawtooth groove designs at wavelength of 20 inches can produce similar levels of SPL responses.

In addition, we have investigated the angle of landing to present differences between driving along the rumble strip and at an angle to the rumble strip as the latter is more realistic. Our results show that the different depths, spacings, and wavelengths can cause different SPL outputs when the angle of landing is non-zero. Overall, the SPL responses from 10 degrees angle of landing are higher than zero-degree angle of landing. We tested 96 cases, and 89.6% of the results show this trend.

As our method depends on the numerical accuracy of the digitized model, when the resolution of the digitization is not fine enough, the computation can stop. In our simulation, there are two stops (5% of the total simulated cases) that cause us to refine our digitization or manually adjust the initial contact between the tire and the rumble strip. Our adjustment is small, i.e., up to 1% of the wavelength. We made this adjustment for 2.2% of the total simulated cases. Also, at the free rolling stage, the angular velocity of the tire is an important factor in successfully extracting the frequencies. We adjust this velocity up to 5% of the theoretical value to better approximate the tire radius under the loading. We made this adjustment for 2.8% of the total simulated cases.

We conclude that our simulations can differentiate the performances of the three families of rumble strip designs, our simulations can analyze the non-zero angle of landing for which the roadside measurement is hard to replicate, and our visualization of the simulation results can indicate the increase and decrease of SPL as the rumble strip dimensions change.

8.0 REFERENCES

An, D. S., Kwon, S. A., Lee, J., & Suh, Y. C. (2017). Investigation of exterior noise generated by vehicles traveling over transverse rumble strips. *Journal of Performance of Constructed Facilities*, *31*(2). https://doi.org/10.1061/(asce)cf.1943-5509.0000951

Bahar, G., & Parkhill, M. (2005). Synthesis of practices for the implementation of centerline rumble strips. In *2005 Annual Conference of the Transportation Association of Canada Transportation Association of Canada*. Retrieved from http://conf.tac-atc.ca/english/resourcecentre/readingroom/conference/conf2005/docs/s18/bahar.pdf

Bahar, G., Wales, J., & Longtin-Nobel, L. (2001). *Synthesis of best practices for the implementation of shoulder and centerline rumble strips* (Project No. 9132). Ottawa, ON: Transportation Association of Canada. Retrieved from https://tac-atc.ca/sites/tac-atc.ca/files/site/pts-rumble.pdf

Bedsole, L. K., Johnson, K. E., & Satterfield, C. (2017). Did you hear that. *Public Roads*, *80*(4). Retrieved from https://highways.dot.gov/public-roads/januaryfebruary-2017/did-you-hear

Beniguel, J., Gaudin, A., Abbadi, Z., & Le Pen, D. (2012). Tire-wheel-cavity dynamic model for structure-borne road noise simulation. In *Proceedings of the acoustics 2012 nantes conference: 11th congrès français d'acoustique: 2012 IOA annual meeting: 23-27 April 2012 Nantes, France: Congress programme and Abstracts*. Retrieved from //hal.archives-ouvertes.fr/hal-00811233/document

Brinkmeier, M., Nackenhorst, U., Petersen, S., & von Estorff, O. (2008). A finite element approach for the simulation of tire rolling noise. *Journal of Sound and Vibration*, *309*(1–2), 20–39. https://doi.org/10.1016/j.jsv.2006.11.040

Brinkmeier, M., Nackenhorst, U., & Volk, H. (2007). A finite element approach to the transient dynamics of rolling tires with emphasis on rolling noise simulation. *Tire Science and Technology*, *35*(3), 165–182. https://doi.org/10.2346/1.2768975

Bucko, T., & Khorashadi, A. (2001). *Evaluation of milled-in rumble strips, rolled-in rumble strips and audible edge stripe*. Sacramento, CA: CalTrans. Retrieved from https://trid.trb.org/view/585100

Caltrans Division of Research and Innovation. (2012). *Traffic noise generated by rumble strips*. Madison, WI: CTC and Associates LLC. Retrieved from https://dot.ca.gov/-/media/dot-media/programs/research-innovation-system-information/documents/preliminary-investigations/rumble-strip-noise-pi-3-5-12-a11y.pdf

Carlson, P. J., & Miles, J. D. (2003). *Effectiveness of rumble strips on Texas highways: First year report* (Report No. FHWA/TX-05/0-4472-1). Austin, TX: Texas Department of

Transportation. Retrieved from https://static.tti.tamu.edu/tti.tamu.edu/documents/0-4472-1.pdf.

Carlson, P. J., Miles, J. D., Pratt, M. P., & Pike, A. M. (2005). *Evaluation of wet-weather pavement markings: First year report*. (Report No. FHWA/TX-06/0-5008-1). Austin, TX: Texas Department of Transportation. Retrieved from https://static.tti.tamu.edu/tti.tamu.edu/documents/0-5008-1.pdf

Chae, S. (2006). *Nonlinear finite element modeling and analysis of a truck tire* (Master's thesis). Pennsylvania State University. Retrieved from https://etda.libraries.psu.edu/files/final_submissions/5920

Chung, T. J. (2002). *Computational fluid dynamics* (1st ed.). Cambridge, United Kingdom: Cambridge University Press. https://doi.org/10.1017/CBO9780511606205

Crocker, M. J. (2007). *Handbook of noise and vibration control* (1st ed.). New York, NY: Wiley.

Dare, T. P. (2012). *Generation mechanisms of tire-pavement noise* (Doctoral dissertation). Purdue University. Retrieved from https://docs.lib.purdue.edu/dissertations/AAI3544123/

De Roo, F., & Gerretsen, E. (2000). TRIAS-tyre road interaction acoustic simulation model. In *29th International Congress on Noise Control Engineering: Nice, France, August 27-31*. Retrieved from http://www.conforg.fr/internoise2000/cdrom/data/articles/000442.pdf

Donavan, P., & Buehler, D. (2018). *Design and acoustic evaluation of optimal sinusoidal rumble Strips versus conventional ground-in rumble strips* (Report. No. CTHWANP-RT18-365.01.2). Sacramento, CA: California Department of Transportation. Retrieved from https://dot.ca.gov/-/media/dot-media/programs/environmental-analysis/documents/env/noise-mumble-strip-report-a11y.pdf

Donavan, P. R., & Rymer, B. (2015). Comparison of vehicle responses to rumble strip inputs of varying design. *SAE International Journal of Passenger Cars - Mechanical Systems*, *8*(3), 964–972. https://doi.org/10.4271/2015-01-2274

Federal Highway Administration (FHWA). (2019). Rumble strips and stripes - safety. Retrieved from https://safety.fhwa.dot.gov/roadway_dept/pavement/rumble_strips/

Fitzpatrick, K. (2000). *Accident mitigation guide for congested rural two-lane highways*. Amsterdam, Netherlands: Amsterdam University Press.

Futamura, S., & Goldstein, A. (2004). A simple method of handling thermomechanical coupling for temperature computation in a rolling tire. *Tire Science and Technology*, *32*(2), 56–68. https://doi.org/10.2346/1.2186774

Ghoreishy, M. H. R. (2008). A state of the art review of the finite element modelling of rolling tyres. *Iranian Polymer Journal, 17*(8), 571-597.

Guidoum, A. C. (2015). *Kernel estimator and bandwidth selection for density and its derivatives* (The kedd package, version, 1). Retrieved from https://cran.microsoft.com/snapshot/2015-07-29/web/packages/kedd/vignettes/kedd.pdf

Han, Y. H., Becker, E. B., Fahrenthold, E. P., & Kim, D. M. (2004). Fatigue life prediction for cord-rubber composite tires using a global-local finite element method. *Tire Science and Technology*, *32*(1), 23–40. https://doi.org/10.2346/1.2186772

Hawkins, N., Smadi, O., Knickerbocker, S., & Carlson, P. (2016). *Rumble stripe: Evaluation of retroreflectivity and installation practices* (Report No. MN/RC 2016-13) St. Paul, MN: Minnesota Department of Transportation, Research Services Library. Retrieved from https://intrans.iastate.edu/app/uploads/2018/03/201613.pdf

Hernandez, J. A., & Al-Qadi, I. L. (2016). Tire–pavement interaction modelling: Hyperelastic tire and elastic pavement. *Road Materials and Pavement Design*, *18*(5), 1067–1083. https://doi.org/10.1080/14680629.2016.1206485

Hong, S. B., Vlahopoulos, N., Mantey, R., & Gorsich, D. (2005). *A computational approach for evaluating the acoustic detection of a military vehicle* (Report No. 2005-01-2337). Warren, MI: US Army TARDEC. Retrieved from https://apps.dtic.mil/sti/pdfs/ADA637003.pdf

Horne, D., Jashami, H., Hurwitz, D. S., Monsere, C. M., & Kothuri, S. (2019). Mitigating roadside noise pollution: A comparison between rounded and sinusoidal milled rumble strips. *Transportation Research Part D: Transport and Environment*, *77*, 37–49. https://doi.org/10.1016/j.trd.2019.10.006

Horne, D., Jashami, H., Monsere, C. M., Kothuri, S., & Hurwitz, D. S. (2020). Evaluating in-vehicle sound and vibration during incursions on sinusoidal rumble strips. *Transportation Research Record: Journal of the Transportation Research Board*, *2675*(3), 154–166. https://doi.org/10.1177/0361198120967947

Hurwitz, D. S., Horne, D., Jashami, H., Monsere, C. M., & Kothuri, S. (2019). *Quantifying the performance of low-noise rumble strips* (Report No. FHWA-OR-RD-19-07). Salem, OR: Oregon Department of Transportation. Retrieved from https://www.oregon.gov/ODOT/Programs/ResearchDocuments/SPR800FinalReport.pdf

Kalathas, P., Hurwitz, D., Parrish, C., Cutter, K. M. G., & Zhang, Y. (2018). A survey on road noise prediction for milled shoulder rumble strip designs. *International Journal of Vehicle Noise and Vibration*, *14*(3), 251. https://doi.org/10.1504/ijvnv.2018.097211

Kamoulakos, A., & Kao, B. G. (1998). Transient dynamics of a tire rolling over small obstacles — A finite element approach with *PAM-SHOCK*. *Tire Science and Technology*, *26*(2), 84–108. https://doi.org/10.2346/1.2135964

Karkle, D. E. (2011). *Effects of centerline rumble strips on safety, exterior noise, and operational use of the travel lane* (Master's thesis, Kansas State University, 2011). Manhattan, Kan.: Kansas State University.

Kennedy, R., & Padovan, J. (1987). Finite element analysis of a steady-state rotating tire subjected to point load or ground contact. *Tire Science and Technology*, *15*(4), 243–260. https://doi.org/10.2346/1.2148792

Kim, Y.-R., You, T. S., & Rilett, L. (2017). *Design and evaluation of modified centerline rumble strips* (Report No. SPR-P1(16) M034). Lincoln, NE: Nebraska University of Nebraska-Department of Transportation Research Reports. Retrieved from https://rosap.ntl.bts.gov/view/dot/32114

Kruntcheva, M. R. (2006). Acoustic-structural resonances of thin-walled structure-gas systems. *Journal of Vibration and Acoustics*, *128*(6), 722–731. https://doi.org/10.1115/1.2345679

Kropp, W., Larsson, K., Wullens, F., Andersson, P., Becot, F. X., & Beckenbauer, T. (2001). The modelling of tyre/road noise-a quasi-three-dimensional model. *In Proceedings Inter-noise 200-abstracts from International Congress and Exhibition on Noise Control Engineering*.

Li, T. (2018). Literature review of tire-pavement interaction noise and reduction approaches. *Journal of Vibroengineering*, *20*(6), 2424–2452. https://doi.org/10.21595/jve.2018.19935

Lin, Y. J., & Hwang, S. J. (2004). Temperature prediction of rolling tires by computer simulation. *Mathematics and Computers in Simulation*, *67*(3), 235–249. https://doi.org/10.1016/j.matcom.2004.07.002

Lindly, J. K. & Narci, A. (2006). *Evaluation of rumble stripe markings*. University Transportation Center for Alabama.

Liu, H. H. (2003). Tread discontinuities as source of vibration/noise — Transient dynamics of rolling tire. *Tire Science and Technology*, *31*(4), 204–224. https://doi.org/10.2346/1.2135269

Liu, H. H. (2007). Load and inflation effects on force and moment of passenger tires using explicit transient dynamics. *Tire Science and Technology*, *35*(1), 41–55. https://doi.org/10.2346/1.2710447

Makarla, R. (2009). *Evaluation of external noise produced by vehicles crossing over centerline rumble strips on undivided highways in Kansas* (Master's thesis, Kansas State University, 2009). Manhattan, Kan.: Kansas State University.

Mathew, J. K., Balmos, A. D., Plattner, D., Wells, T., Krogmeier, J. V., & Bullock, D. M. (2018). *Assessment of alternative sinusoidal rumble stripe construction* (Report No. FHWA/IN/JTRP-2018/05). West Lafayette, IN: Purdue University. https://doi.org/10.5703/1288284316648

Miles, J. D., & Finley, M. D. (2007). Factors that influence the effectiveness of rumble strip design. *Transportation Research Record: Journal of the Transportation Research Board*, *2030*(1), 1–9. https://doi.org/10.3141/2030-01

Moazami, D., Muniandy, R., Hamid, H., & Yusoff, Z. M. (2011). Effect of tire footprint area in pavement response studies. *International Journal of Physical Sciences, 6*(21), 5040-5047. https://doi.org/10.5897/IJPS11.1085

Mohamed, Z., & Wang, X. (2015). A study of tyre cavity resonance and noise reduction using inner trim. *Mechanical Systems and Signal Processing*, *50–51*, 498–509. https://doi.org/10.1016/j.ymssp.2014.05.044

Molisani, L., Burdisso, R., & Tsihlas, D. (2003). A coupled tire structure/acoustic cavity model. *International Journal of Solids and Structures*, *40*(19), 5125–5138. https://doi.org/10.1016/s0020-7683(03)00259-2

Muggleton, J., Mace, B., & Brennan, M. (2003). Vibrational response prediction of a pneumatic tyre using an orthotropic two-plate wave model. *Journal of Sound and Vibration*, *264*(4), 929–950. https://doi.org/10.1016/s0022-460x(02)01190-2

Nadeau, G. G. (2009). National standards for traffic control devices; the manual on uniform traffic control devices for streets and highways; maintaining pavement marking retroreflectivity. *Federal Register, 82*(2), 770-780.

Ning, D., Du, H., Sun, S., Li, W., & Zhang, B. (2018). An innovative two-layer multiple-DOF seat suspension for vehicle whole body vibration control. *IEEE/ASME Transactions on Mechatronics*, *23*(4), 1787–1799. https://doi.org/10.1109/tmech.2018.2837155

Oregon Department of Transportation (ODOT) (2018). *Traffic line manual (TLM)*. Salem, OR: Oregon Department of Transportation, Engineering & Technical Services Branch. Retrieved from https://www.oregon.gov/ODOT/Engineering/Documents_TrafficStandards/Traffic-Line-Manual.pdf.

Parker, N. A., & Meja, M. S. J. (2003). Evaluation of performance of permanent pavement markings. *Transportation Research Record: Journal of the Transportation Research Board*, *1824*(1), 123–132. https://doi.org/10.3141/1824-14

Pinnington, R., & Briscoe, A. (2002). A wave model for a pneumatic tyre belt. *Journal of Sound and Vibration*, *253*(5), 941–959. https://doi.org/10.1006/jsvi.2001.3944

Rasmussen, R. O., Bernhard, R. J., Sandberg, U., & Mun, E. P. (2007). *The little book of quieter pavements.* (Report No. FHWA-IF-08-004). Washington, D.C.: Federal Highway Administration. Retrieved from https://rosap.ntl.bts.gov/view/dot/41905

Richards, T. (1991). Finite element analysis of structural-acoustic coupling in tyres. *Journal of Sound and Vibration*, *149*(2), 235–243. https://doi.org/10.1016/0022-460x(91)90633-u

Rys, M. J., Karkle, D. E., Vijayakumar, A., Makarla, R., & Russell, E. (2010). *Promoting centerline rumble strips to increase rural, two-lane highway safety* (Report No. K-TRAN: KSU-08-3). Topeka, KS: Kansas Department of Transportation. Retrieved from https://engg.k-state.edu/files/transport/imported/Reports/2008/KSU083_Final.pdf

Society of Automotive Engineers (SAE). (2000). *Measurement of interior sound levels of light vehicles* (Report No. SAE J1477). Warrendale, PA: SAE International.

Seo, J. H., Moon, Y. J., & Shin, B. R. (2008). Prediction of cavitating flow noise by direct numerical simulation. *Journal of Computational Physics*, *227*(13), 6511–6531. https://doi.org/10.1016/j.jcp.2008.03.016

Smets, M. P., Eger, T. R., & Grenier, S. G. (2010). Whole-body vibration experienced by haulage truck operators in surface mining operations: A comparison of various analysis methods utilized in the prediction of health risks. *Applied Ergonomics*, *41*(6), 763–770. https://doi.org/10.1016/j.apergo.2010.01.002

Smith, M. (2016). *SMITH, M/Standard user's manual*. Providence, RI: Dassault Systèmes Simulia Corp.

Soares, F., Freitas, E., Cunha, C., Silva, C., Lamas, J., Mouta, S., & Santos, J. (2017). Traffic noise: Annoyance assessment of real and virtual sounds based on close proximity measurements. *Transportation Research Part D: Transport and Environment*, *52*, 399–407. https://doi.org/10.1016/j.trd.2017.03.019

Takagi, R., & Takanari, S. (1991). Tire structural parameter analysis for road noise using an accurate FEM model. *SAE Technical Paper Series, 100*, 987-996. doi:10.4271/911873

Terhaar, E. & Braslau, D. (2015). *Rumble strip noise evaluation* (Report No. MN/RC 2015-07). St. Paul, MN: Technical Report Minnesota Department of Transportation, Research Services Library. Retrieved from http://www.dot.state.mn.us/research/TS/2015/201507.pdf

Terhaar, E., Braslau, D., & Fleming, K. (2016). *Sinusoidal rumble strip design optimization study* (Report No. MN/RC 2016-23). St. Paul, MN: Technical Report Minnesota Department of Transportation, Research Services Library. Retrieved from https://www.dot.state.mn.us/trafficeng/safety/docs/sinusoidalrumblestripdesignoptimizationstudy.pdf

Tong, G., Wang, Q., Yang, K., & Wang, X. C. (2013). An experiment investigation to the radial tire noise. *Advanced Materials Research*, *694–697*, 361–365. https://doi.org/10.4028/www.scientific.net/amr.694-697.361

Torbic, D. J. (2009). *Guidance for the design and application of shoulder and centerline rumble strips* (Report 641). Washington, D.C.: Transportation Research Board. https://doi.org/10.17226/14323

Tufuor, E. O. A., Rilett, L. R., & TenHulzen, P. (2017). In-vehicle evaluation of milled rumble strips in pre– and post–chip seal maintenance periods. *Transportation Research Record: Journal of the Transportation Research Board*, *2612*(1), 47–59. https://doi.org/10.3141/2612-06

Wang, G. (2009). *Effects of truck tire type and tire-pavement interaction on top-down cracking and instability rutting* (Dissertation, University of Florida, 2009). Ann Arbor, MI: ProQuest LLC. Retrieved from https://www.proquest.com/openview/c26bfe7905fbd93f48706d2daa58b25b/1.pdf?pq-origsite=gscholar&cbl=18750&diss=y

Wang, H. (2011). *Analysis of tire-pavement interaction and pavement responses using a decoupled modeling approach* (Doctoral dissertation, University of Illinois at Urbana-Champaign, 2011). Urbana, IL: University of Illinois. Retrieved from https://www.ideals.illinois.edu/items/25037

Wang, H., Al-Qadi, I.L., & Stanciulescu, I. (2010). *Effect of friction on rolling tire-pavement interaction* (Project No. 049IY02). West Lafayette, IN: NEXTRANS. Retrieved from https://www.purdue.edu/discoverypark/cav/nextrans/completed-projects/docs/Final%20Report%20049.pdf

Wang, G., & Roque, R. (2011a). Impact of wide-based tires on the near-surface pavement stress states based on three-dimensional tire-pavement interaction model. *Road Materials and Pavement Design*, *12*(3), 639–662. https://doi.org/10.1080/14680629.2011.9695264

Wang, G., & Roque, R. (2011b). Evaluation of truck tire types on near-surface pavement response based on finite element analysis. *International Journal of Pavement Research Technology*, *4*(4), 203-211.

Wei, Y., Feng, X., Fuqiang, Z., & Xiang, D. (2016). Simulation of rolling noise based on the mixed Lagrangian–Eulerian method. *Tire Science and Technology*, *44*(1), 36–50. https://doi.org/10.2346/tire.16.440103

Wehbe, N. I., Jones, A., & Druyvestein, T. (2017). *Optimization of pavement marking performance* (Report No. MPC 17-341) Pierre, SD: South Dakota Department of Transportation. Retrieved from https://www.ugpti.org/resources/reports/downloads/mpc17-341.pdf

Wilcox, D. (1998). *Turbulence modeling for CFD* (2nd ed.). La Canada, CA: DCW Industries.

Wright, C., & Koopmann, G. H. (1986). A technique to predict the acoustic radiation characteristics of an automobile tire. *Tire Science and Technology*, *14*(2), 102–115. https://doi.org/10.2346/1.2148767

Yang, J. S., Fwa, T. F., Ong, G. P., & Chew, C. H. (2013). Finite-element analysis of effect of wide-base tire on tire-pavement noise. *Advanced Materials Research*, *723*, 105–112. https://doi.org/10.4028/www.scientific.net/amr.723.105

Yang, X., Olatunbosun, O., & Bolarinwa, E. (2010). Materials testing for finite element tire model. *SAE International Journal of Materials and Manufacturing*, *3*(1), 211–220. https://doi.org/10.4271/2010-01-0418

Yum, K., Hong, K., & Bolton, J. S. (2007). Influence of tire size and shape on sound radiation from a tire in the mid-frequency region. *SAE Technical Paper Series, 116*, 1801-1807. doi:10.4271/2007-01-2251

APPENDIX A

As rumble stripes and rumble strips are effective devices to enhance driving safety, there are published reports from different transportation agencies documenting on-vehicle or roadside measurements. We have collected 224 roadside measurement data on sound level differences (SLDs) from different reports created in the span of 2007 to 2019. Some of the reports studied multiple vehicles and multiple vehicle speeds to compare the performances of conventional and sinusoidal designs. In addition, we have surveyed over 97 retroreflectivity measurements from 2003 to 2018. In this appendix: Review of Published Reports on Roadside Measurements, we first analyze the retroreflectivity measurement on rumble stripes that use white and yellow markings. We compare the measurements over flat road, conventional rumble stripes and sinusoidal rumble stripes. Then we focus on rumble strips that alert the drivers with sound level outputs. We include the interior and exterior SLDs from roadside measurements on both conventional and sinusoidal rumble strips. The reference sound pressure in the air is 2×10^{-5}N/m2, or 0.00002 Pascal. The SLD defined in the reports that we have surveyed is the deviation from this reference value.

Retroreflectivity from Rumble Stripes

When the pavement marking is placed throughout the line of the rumble strip, it becomes a rumble stripe as shown in the right image of Figure A.1. The retroreflectivity is a particular functionality of the rumble stripes and provides driving guidance similar to flat pavement markings (Hawkins et al., 2016). When a vehicle is traveling along the rumble stripe, the amount of retroreflectivity is provided by the direction of travel along the marking. The marking is either with white or yellow paint.

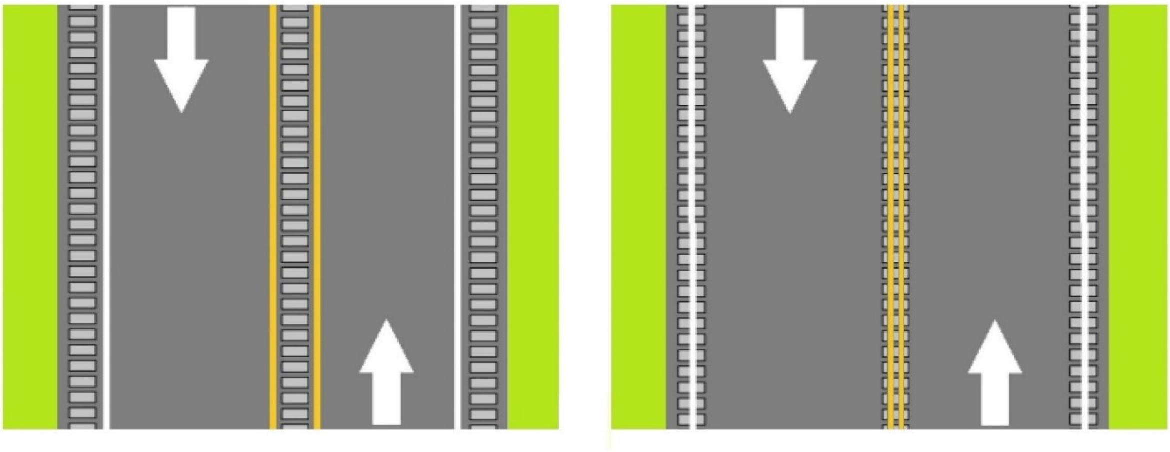

Figure A.1: Rumble strips (left); Rumble stripes (right).

To standardize the measurements of retroreflectivity from the rumble stripes, the Federal Highway Administration (FHWA) recommends using two retroreflectivity measurement methods: hand-held instruments and mobile instruments. In particular, mobile instruments are devices placed on vehicles, and on the vehicles that pass next to the pavement markings at specific speeds (Carlson et al., 2014; Mathew et al., 2018). As a standard, 30 m is the distance to measure retroreflectivity that is expressed in the units of millicandelas per square meter per lux (mcd/m2/lux). Depending on paint colors, placement locations and road speed limits, FHWA recommends minimum thresholds for pavement retroreflectivity (Carlson et al., 2005). From state to state, these thresholds are used as guides.

The retroreflectivity results for flat pavement, conventional and sinusoidal rumble stripes using white and yellow markings are presented in Figure A.2 for the measurements published in a number of references (Parker and Meja, 2003; Carlson et al., 2005; Lindly and Narci, 2006; Hawkins et al., 2016; Wehbe et al., 2017; Mathew et al., 2018). We derive a probability distribution for each pavement and visualize it using a violin plot that includes median and interquartile information. The boxes inside the violin plots denote the interquartile range of the retroreflectivity measurements. Moreover, the thick horizontal line in the boxes indicates the median values.

We note that the plot for the sinusoidal design shows that the upper quartile and lower quartile ranges are significantly higher than those of the conventional pattern and flat pavement for the white and yellow markings. This figure shows that yellow markings always have lower retroreflectivity levels than white markings regardless of the surface they are applied on. Lastly, we note that we have negative retroreflectivity results (gray shaded rectangular regions) as the probability density is calculated with a kernel density estimator, which is the Gaussian kernel (Guidoum, 2015).

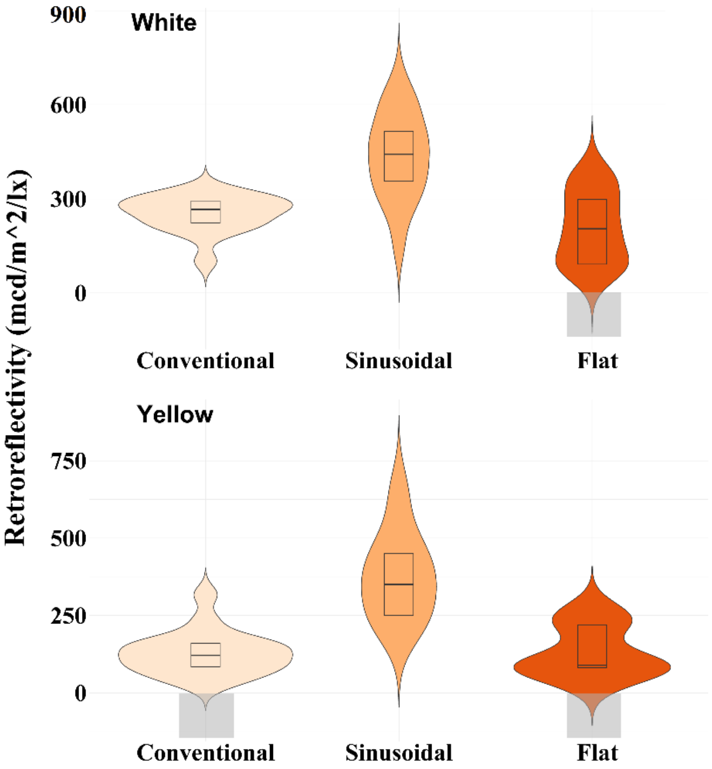

Figure A.2: Violin plots of retroreflectivity results from literature.

In addition, we note that the conventional rumble stripe can provide adequate retroreflectivity during wet and other inclement weather as the contour of rumble stripes drains the rainwater effectively and provide a reflective surface to maintain the retroreflectivity (Carlson and Miles, 2003). Similar quantification of how sinusoidal rumble stripes perform in wet and inclement weather was not found in our search.

Measurement Locations/Methods for SLDs from Rumble Strips

To obtain sound level measurements from vehicles driven over different rumble strips, each roadside measurement needs to respect driver safety; thus, the location of the measurement devices can vary. A report from the Society of Automotive Engineers International (SAE, 2000) recommends near the front seats for interior noise measurements. In studies where the test conditions allow, the position is selected to be close to the driver's ear to achieve the best agreement between the measurement and the sound that the drivers receive. We present the commonly used positions for microphones and sound level meters in Figure A.3 (Terhaar et al., 2016; Tufuor et al., 2017; Mathew et al., 2018; Donavan and Buehler, 2018).

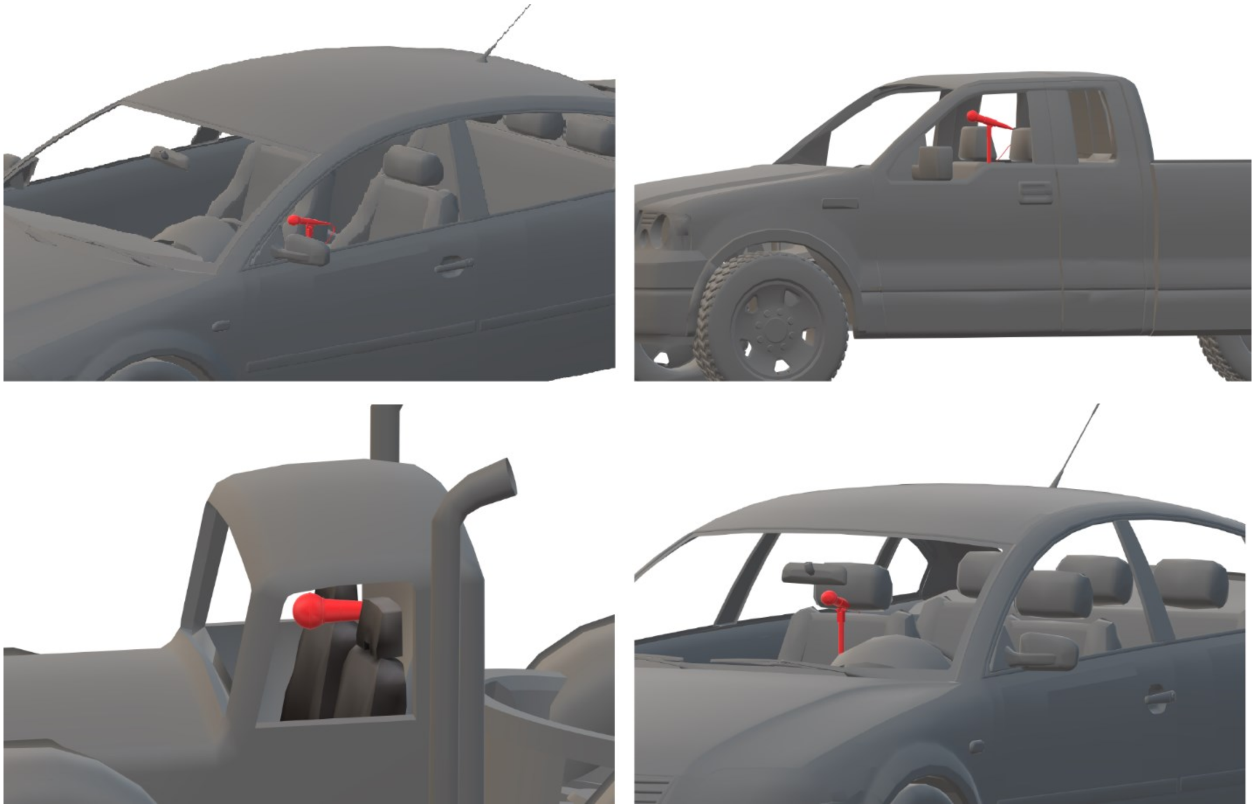

Figure A.3: Positions for microphones/sound level meters (colored in red) for interior sound level measurements.

For the measurement of the exterior noise, Donavan and Buehler (2018) apply two methods: on-board and pass-by. A schematic drawing is included in Figure A.4. The left image shows the on-board and the right image shows the pass-by. The on-board and the pass-by measurements include vehicle and environment noises. Likely, the pass-by measurements better approximate the noise level detected by the nearby residential neighborhoods.

Figure A.4: Positions for microphones/sound level meters (colored in red) for exterior sound level measurements.

In 2007, Danish researchers published a seminal study that suggested sinusoidal rumble strips/stripes could generate lower exterior noise. In 2009, sinusoidal rumble strips/stripes were tested in California (Bedsole et al., 2017). Since then, multiple studies have shown that the sinusoidal produces lower exterior SLD than the conventional rumble strips/stripes. To confidently replace conventional rumble strips with sinusoidal designs, sufficient number of roadside measurements and rigorous modeling analysis are needed to quantify the sound output levels to ensure a sufficient loudness is maintained for the drivers while unnoticeable disturbance is observed by the nearby neighborhoods and wildlife.

Interior SLD for Selected Reports

We first present results from a few selected reports that comprehensively studied multiple vehicles along with conventional and sinusoidal designs. We describe the exact rumble strip dimensions. The interior sound level differences from conventional and sinusoidal designs are contrasted against the recommended range from the National Cooperative Highway Research Program (NCHRP) 641 report published in 2009 (Torbic et al., 2009).

We display in Figure A.5 the interior SLD measurements collected in Donavan and Buehler for a sinusoidal pattern that is 0.314 inches in depth and 14 inches in wavelength and for a conventional pattern that is 0.314 inches in depth, 12 inches in spacing, 8 inches in length, and 4 inches in width.

The magenta boxes represent the urban/rural and freeway interior SLD range suggested by NCHRP report 641 (Torbic et al., 2009). There are three vehicle types studied: passenger, pick-up truck and semi-truck. We note that the measurements of pickup trucks and semi-trucks are missing as only results at 60 mph are given in the literature reviewed (Donavan and Buehler, 2018). When the passenger vehicles investigated are driven at 20 mph, the interior SLD measurement from the sinusoidal pattern is lower than that from the conventional pattern (Donavan and Buehler, 2018). Contrarily, when the passenger vehicles are driven over 40 mph, the sinusoidal pattern generates higher interior SLD than the conventional pattern does and much higher SLD than what NCHRP report 641 suggested. The high interior SLD can startle drivers and lead to undesirable results (Torbic et al., 2009).

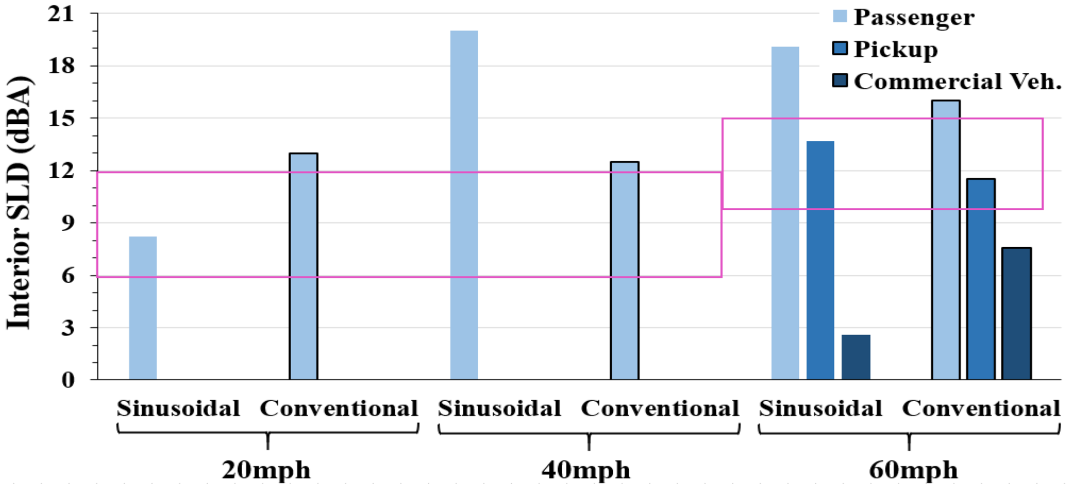

Figure A.5: The interior SLD measurements produced by conventional (dark border), and sinusoidal (no border) rumble strips have different trends (Donavan and Buehler, 2018). The interior SLD measurements are extracted from three types of vehicles driven at 20 mph, 40 mph and 60 mph.

As shown in Figure A.6, there are 9 interior SLD measurements for the sinusoidal patterns from Mathew et al. (2018). We note that the interior SLD measurements for the conventional pattern with 12 inches in spacing for semi-trucks are not reported in the literature. By reducing the wavelength, the interior SLD increases. We observe when the wavelength and spacing are 12 inches, both conventional and sinusoidal patterns can produce interior SLD in the suggested range for passenger vehicle at 50 mph, and the sinusoidal pattern generates higher interior SLD comparatively. We note there are negative interior SLD results, which could be caused by background traffic noise, radio sound and weather condition.

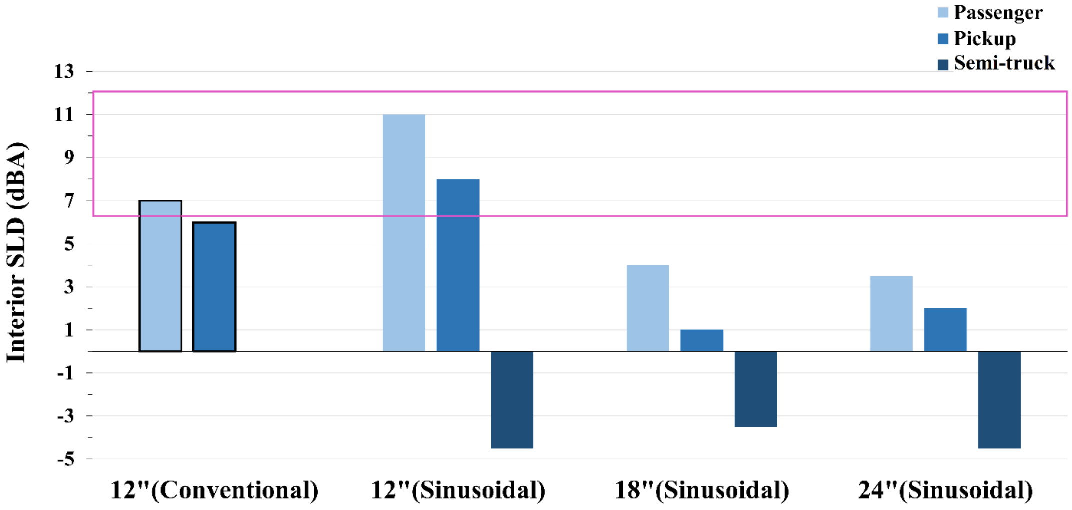

Figure A.6: The interior SLD measurements are collected from three types of vehicles driven at 50 mph (Mathew et al., 2018). Our X-axis denotes four different wavelength/spacing of rumble stripes. The magenta boxes represent the urban/rural and freeway interior SLD range suggested by NCHRP report 641 (Torbic et al., 2009).

Furthermore, for conventional designs, the depth of the rumble strip influences the interior SLD generated, i.e., increasing depth led to increasing of the interior SLD measurements is shown by Tufuor et al. (2017). Results from Tufuor et al. are shown in Figure A.7, the interior SLD measurements generated from conventional rumble strips are influenced by depth, when other dimensions are 6 inches in length, 6 inches in width and 12 inches in spacing. The X-axis denotes the depth of conventional rumble strips and the vehicle speeds. Moreover, interior SLD measurement increases as the testing speed increases from 55 mph to 65 mph. We note that for each depth, there is a different interior SLD for each speed level. This demonstrates the coupled effect of the vehicle speed and rumble depth. Lastly, the authors suggest that 0.124 inches reduction in depth of the milled rumble strips/stripes does not result in any lower practical effectiveness for adequate driver feedback.

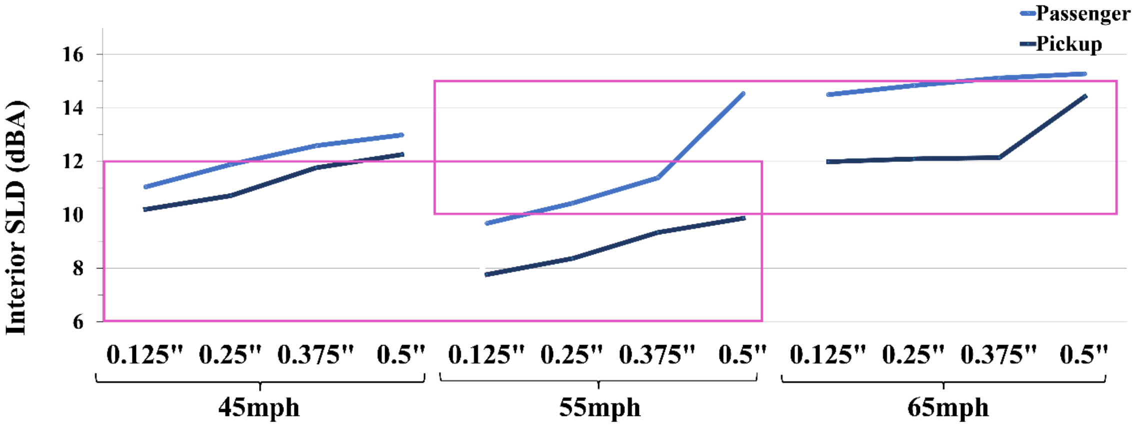

Figure A.7: The interior SLD measurements are based on two types of vehicles driven at 45 mph, 55 mph and 65 mph. The magenta boxes represent the urban/rural and freeway interior SLD range suggested by NCHRP report 641 (Torbic et al., 2009).

The above selected studies indicate that the vehicle speed and type affect the final sound output. For the selected vehicles, the conventional and sinusoidal designs produce different levels of sound outputs. Next, we analyze all the reports that we have collected on interior SLD to provide an overview of the probabilistic distribution for the rumble strip designs.

Interior SLD for All Reports

These reports contained different measurement methods; thus, analyzing the distribution of the noise levels is more appropriate than comparing over each vehicle or each rumble strip. Here we focus on the behavior from the aggregate data. Our analysis currently omits the difference between centerline and shoulder rumble strips/stripes as there is only a limited number of reports from 2007 to 2019. The level of refinement regarding pavement condition, driver information, rumble strip location and measurement methodology can be included once more studies are performed.

For measurements published in a number of references (Miles and Finley, 2007; Torbic et al., 2009; Donavan and Rymer, 2015; Terhaar and Braslau, 2015; Terhaar et al., 2016; Kim et al., 2017; Tufuor et al., 2017; Mathew et al., 2018; Donavan and Buehler, 2018; Donahue, 2018; Hurwitz et al., 2019), we present the probability density distribution for some of the SLDs such as those near the recommendations given by NCHRP 641. The violin plots of interior SLD measurements for passenger vehicles, pickup trucks and semi-trucks over conventional (light blue) and sinusoidal (dark blue) rumble strips/stripes are shown in Figure A.8.

The wider sections indicate higher probabilities, and the skinnier sections show lower probabilities, and for each type of vehicle, the extensive sections indicate the higher probability density of the interior SLD measurements at a particular value. The black boxes in the violin plots denote the interquartile range of interior SLD measurements. Moreover, the thick horizontal line in the boxes indicates the median values.

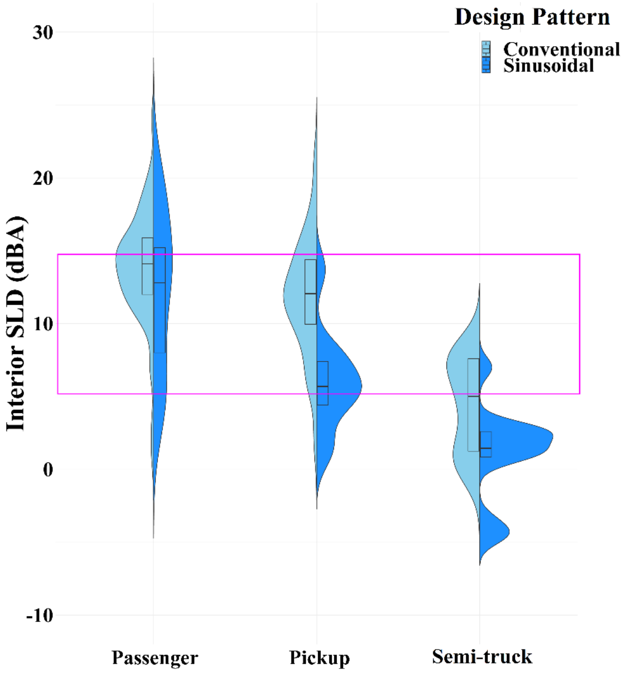

Figure A.8: Violin plots of interior SLD measurements. Testing speeds are from 20 to 65 mph. Our solid black curves enclosing the blue areas denote the probability density of the interior SLD measurements for conventional (light blue) and sinusoidal (dark blue) design patterns at different values. The magenta boxes represent the urban/rural and freeway interior SLD range suggested by NCHRP report 641 (Torbic et al., 2009).

For the passenger vehicles, the interquartile ranges and median values are similar for both design patterns around 15 dBA. As for the distribution density, the lower and upper quartile ranges of the sinusoidal rumble strips/stripes are slightly lower than that of the conventional rumble strips/stripes. For the pickup trucks, the higher probability density is around 10 to 13 dBA for the conventional, and from 5 to 7 dBA for the sinusoidal. Comparing the quartile ranges, the sinusoidal rumble strips/stripes have a lower range than that of the conventional rumble strips/stripes for all three types of vehicles. In addition, the median of the sinusoidal is much lower than that of the conventional. For both designs, inadequate interior SLD for the semi-trucks are noted. The higher probability density distribution from the conventional rumble strips/stripes is around 7.5 dBA, and in contrast, around 3dBA for sinusoidal. Note that all measurements have been taken in an ideal cabin with no ambient noise.

Recent studies examine the effects of noises from climate control fans and audio equipment and indicate that a 1-2 dBA background noise increment on average (Hurwitz et al., 2019). Consequently, this increment causes a further reduction in the interior SLD and fails the sinusoidal design on meeting the recommended ranges for semi-trucks and possibly also for some pickup trucks.

Exterior SLD for Selected Reports

We now focus on the exterior sound level differences. Exterior traffic sound emission creates a negative impact on human health (Soares et al., 2017). Rumble strips/stripes raise the exterior noise level while providing interior sound level to the drivers (Bahar and Parkhill, 2005; Terhaar and Braslau, 2015). Currently, there are limited numbers of studies focusing on the exterior sounds from rumble strips/stripes (Fitzpatrick, 2000; Bucko and Khorashadi, 2001; Torbic et al., 2009). Only 8 out of 34 rumble strips/stripes designs from 2007 to 2015 have been measured for their exterior sound levels (Kalathas et al., 2018).

As the traffic types and road conditions vary, different studies implement different exterior sound measurement methodologies. For instance, in some studies, measurements for centerline rumble strips/stripes are taken while the vehicles pass from the far lane, and while other studies take measurements having vehicles pass on both the far and the near lanes. Furthermore, the research from the Federal Highway Administration states that the exterior sound produced by rumble strips/stripes is challenging to measure and the sound produced by rumble strips/stripes is more intermittent than normal traffic noise. Consequently, only the peak sound level is considered (FHWA, 2015; Himes et al., 2017). Lastly, Horne et al. have concluded that the rumble strip/stripe SLD measurements from heavy vehicles were complicated because the tire width of the large vehicle could be larger than the width of the rumble strips/stripes (Horne et al., 2019).

We have collected 37 data sets of exterior SLD measurements created by seven agencies from 2007 to 2019. Multiple studies conclude that exterior SLD is related to the distance to nearby residential neighborhoods. Karkle has stated that exterior SLD generated by rumble strips/stripes were reduced to inconceivable levels after 61 m (200 feet) (Karkle, 2011). Parkhill has stated that in Canada rumble strips/stripes were illegal to be installed at a distance closer than 200 m (656 feet) from residential communities due to noise complaints. Additionally, the study states that SLD diminishes after 200 m (656 feet) and can be ignored after 500 m (1640 feet) (Bahar and Parkhill, 2005).

Terhaar and Braslau have presented the “detectability” level as a potential exterior SLD threshold. In the study, the authors stated that humans could detect an invasive sound if the sound level of any invasive frequency with the same frequency as the background sound is 7 dBA higher (Terhaar and Braslau, 2015). Applying this threshold to field measurements, the authors found that rumble strips/stripes sound could be detectable at distances more than 914.5 m (3000 feet). However, this is only true when drivers and passengers perform active listening, meaning that they actively focus on identifying sound differences, which allow higher thresholds regarding the exterior sound.

Furthermore, Terhaar and Braslau have compared exterior SLD measurements from two sinusoidal rumble strips/stripes to that of one conventional pattern. These rumble strips are in different dimensions: sinusoidal A is 0.624 inches in depth, 14 inches in wavelength, and 8 inches in length; sinusoidal B is 0.013 inches in depth, 24 inches in wavelength, and 8 inches in length; the conventional pattern is 16 inches in length, 0.013 inches in depth, and 12 inches in spacing. In Figure A.9, our X-axis denotes the design pattern grouped by speed range: conventional, sinusoidal A (Sin A), and sinusoidal B (Sin B). The magenta line represents the "detectability" level given in (Terhaar and Braslau, 2015). There are 13 out of the 18 SLDs that are in the suggested range for the sinusoidal rumble strips/stripes, and 1 out of the 6 results is in the suggested range for the conventional pattern. The SLD for the sinusoidal B at 45 mph is 0 dBA for semi-trucks. At 30 mph, sinusoidal A and B have negative SLD for semi-trucks which means not noticeable. We note that the exterior SLD measurements for the conventional rumble strips/stripes at 45 mph and 60 mph are missing as they are not reported in the literature.

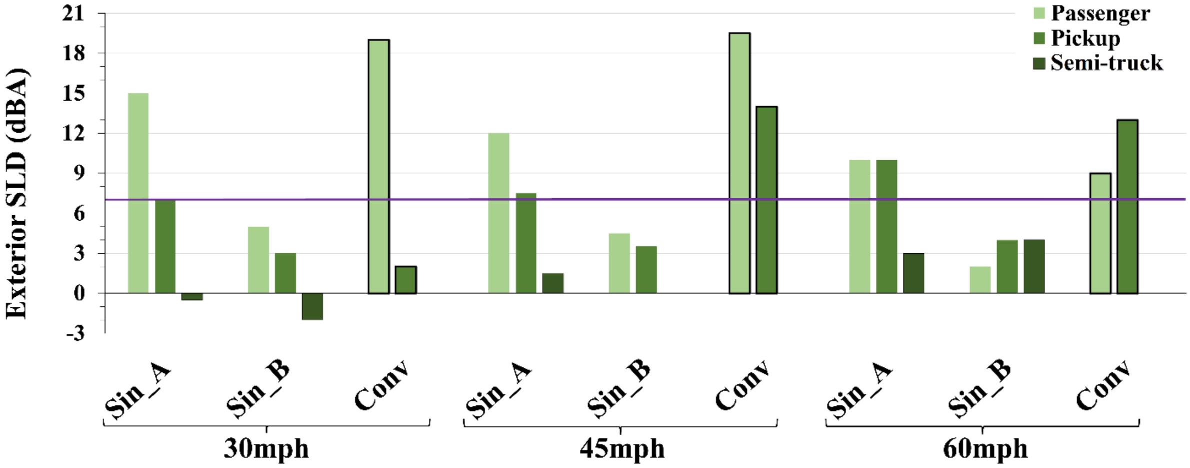

Figure A.9: The exterior SLD are affected by rumble strip design pattern at different speed levels for three types of vehicles.

Comparing the two sinusoidal designs, the sinusoidal B strip has less depth and longer wavelength resulting in lower exterior SLD at 30 mph, 45 mph, and 60 mph. Data collected in Donavan and Buehler are shown Figure A.10 for 3 types of vehicles driven at 20 mph, 40 mph and 60 mph (Donavan and Buehler, 2018). The sinusoidal pattern is 0.314 inches in depth and 14 inches in wavelength, and the conventional pattern is 0.314 inches in depth, 12 inches in spacing, 8 inches in length, and 4 inches in width. The magenta boxes represent the urban/rural and freeway interior SLD range suggested by NCHRP report 641 (Torbic et al., 2009). Three vehicle types: passenger, pick-up trucks and semi-trucks were considered. We note that results at 60 mph are the only data given for pickup trucks and semi-trucks (Donavan and Buehler, 2018). Overall, the sinusoidal pattern produces lower exterior SLD for all vehicle types at different testing speed levels than the conventional pattern does in the study.

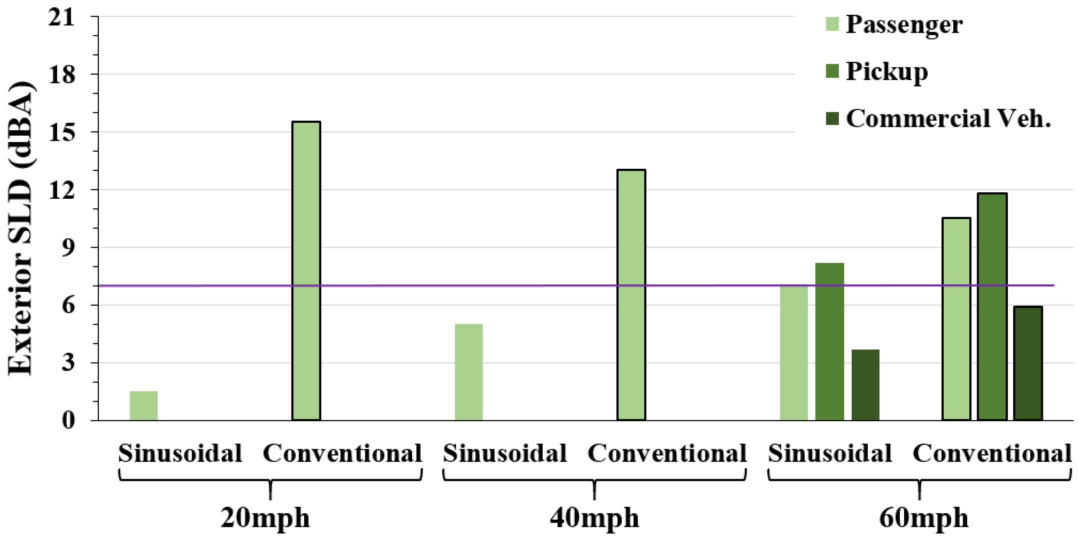

Figure A.10: The exterior SLD measurements produced by conventional and sinusoidal rumble strips have different trends. The SLD results are extracted from three types of vehicles driven at 20 mph, 40 mph and 60 mph.

The exterior SLD measurements from Mathew et al. are based on three different wavelength/spacing dimensions: 12 inches, 18 inches, and 24 inches. The experiment speed was 50 mph (Mathew et al., 2018). As shown in Figure A.11, the SLD generated by the conventional pattern are higher than those from the sinusoidal patterns. Our X-axis denotes four different wavelength/spacing dimensions. We note that the exterior SLD measurements on semi-truck from the conventional pattern with 12 inches in spacing are missing as they are not reported in the literature. These three sinusoidal patterns can produce SLD within the suggested range. Furthermore, as the wavelength increases, the SLD decreases for the sinusoidal pattern.

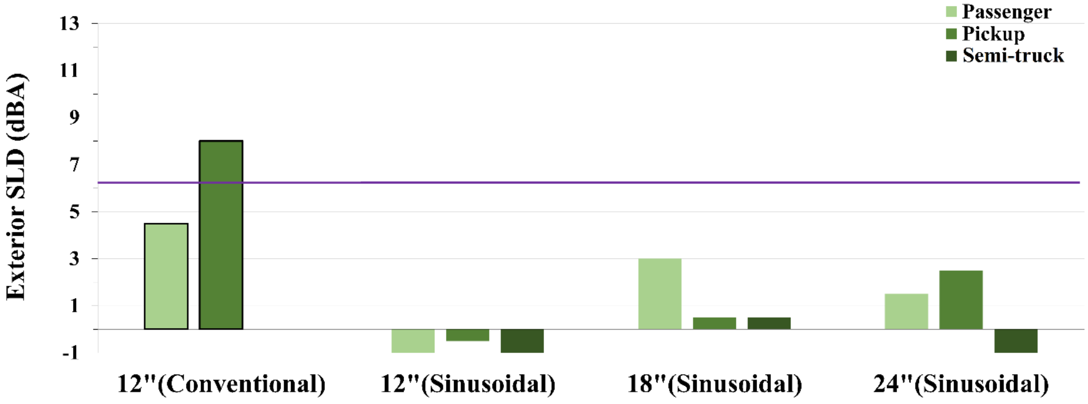

Figure A.11: The exterior SLD measurements are affected by the magnitude of the wavelength/spacing. The SLD results are collected from three types of vehicles driven at 50 mph.

Figure A.12 indicates that when the length is 14 inches, rumble strips/stripes with shallower depths generate lower exterior SLD for all types of vehicles (Terhaar et al., 2016). The exterior SLD generated by rumble stripes with 0.374 inches in depth is lower than that from the rumble stripes with 0.4 inches in depth for all testing vehicle types. When the depth is 1/2 inches, as the length increases from 14 inches to 20 inches, the SLD increases. On the other hand, when the depth is 3/8 inches, the SLD for the passenger decreases as the length increases from 14 inches to 20 inches.

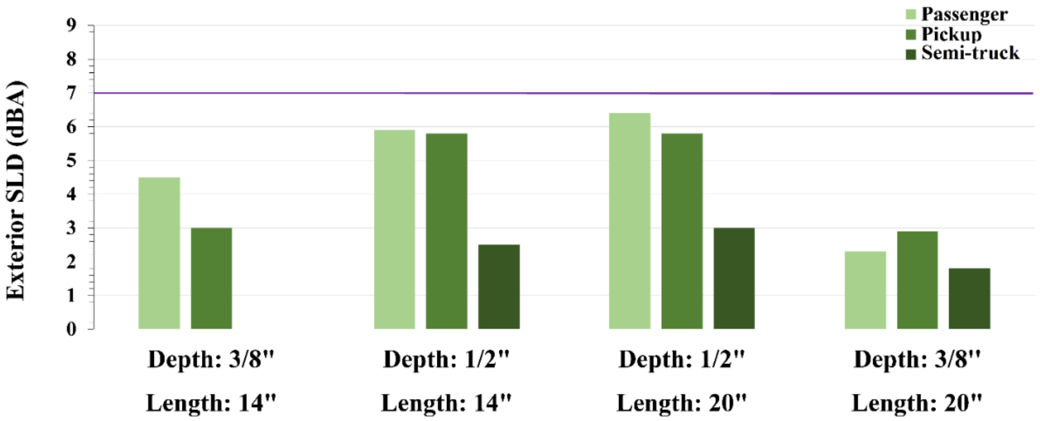

Figure A.12: The exterior SLD measurements for three types of vehicles driving at 50 mph are affected by the length and depth of the rumble stripes when their wavelengths are fixed at 14 inches.

Exterior SLD for All Reports

We now analyze all the reports that we have surveyed on the exterior SLD measurements for passenger vehicles, pickup trucks and semi-trucks over conventional (light green) and sinusoidal (dark green) rumble strips/stripes. As shown in Figure A.13, we include measurements from a number of references (Donavan and Rymer, 2015; Terhaar et al., 2016; Mathew et al., 2018; Donavan and Buehler, 2018; Donahue, 2018; Hurwitz et al., 2019). In the above figure, we have marked 7dBA with a purple line as it is recommended. The higher probability density distribution of exterior SLD measurements for the conventional is observed around 13 dBA, and around 5 dBA for the sinusoidal. For the interquartile ranges, the sinusoidal rumble strips/stripes have a lower range than the conventional rumble strips/stripes do. Moreover, the median value of the sinusoidal is significantly lower than that of the conventional rumble strips/stripes. For the pickup trucks, the highest probability density of SLD measurements is from 10 to 15 dBA for the conventional, and around 2.5 dBA for the sinusoidal. Comparing the interquartile range, the sinusoidal rumble strips/stripes have lower first and third quartile values than the conventional rumble strips/stripes do. For the semi-trucks, we observe the similar trend, but we note that the conventional does not have a regular quartile range due to insufficient data.

From the interior and exterior SLD measurements, we have found that as the depth increases where other parameters remain fixed, the interior SLD increase for the sinusoidal design. Also, as the wavelength of sinusoidal increases while keeping other parameters fixed, the interior and exterior SLD decrease. Similarly, for the conventional design, as the depth increases where other parameters remain fixed, the interior SLD increase; however, we do not have enough data points for the exterior SLD for the depth.

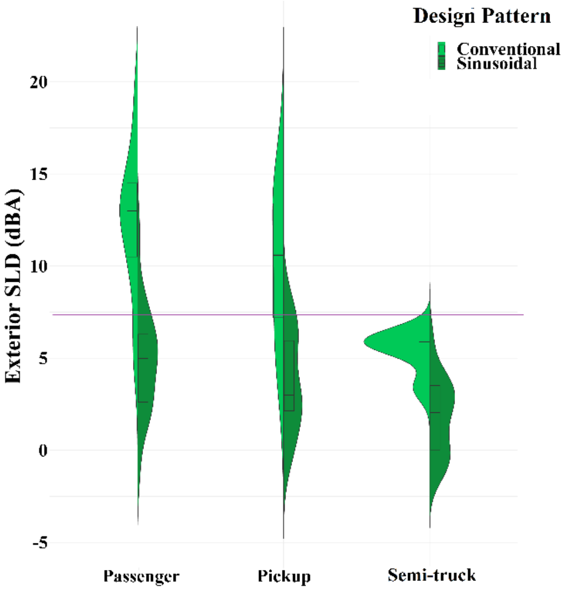

Figure A.13: Violin plots of exterior SLD measurements. The testing speeds are from 20 to 65 mph.

We have surveyed over 97 retroreflectivity and 224 sound output measurements. Yellow and white markings on rumble stripes outperform those on the flat road as a guiding device. Furthermore, some of the measurements indicate that sinusoidal rumble strips/stripes produce lower exterior noise levels than the conventional patterns do for passenger vehicles, pickup trucks and semi-trucks while inconclusive findings exist for the interior acoustic signals.

In this appendix, to aid the search for optimal rumble designs and minimize trial-and-error during in-situ experimentation, we have presented analysis over existing roadside measurements along with recommendations from published national and state reports, international standards and third-party studies.

APPENDIX B

Vehicle sound is a significant contributor to traffic noise (Yang, 2010). Sounds such as those from the engines and aerodynamics are small when the driving speed is lower than 75 mph (Rasmussen et al., 2007). In this appendix: Review of Relevant Numerical Simulation Results, we review recent publications on quantifying the tire-pavement noise that is essential to determine the effectiveness of the rumble strip/stripe designs. Tire-pavement contact depends on the geometry, material and surface texture of the tire and the pavement. The Finite Element Method (FEM) has been used for tire-pavement noise modeling since the 1980s. The geometries of the objects are discretized into small unit elements and the material behaviors are described using linear and nonlinear models. Balance of energy and momentum for the structures under loading conditions is solved using high performance computing algorithms.

There are multiple components in tires including the interior air cavity, tire carcass, belt reinforcement and tire tread. Each contributes to the overall noise output when the tires are rolling over the rumble strips. Accurate descriptions of the tire components are crucial to valid FEM simulations (Kropp, 1989; Pinnington and Briscoe, 2002; Muggleton, Mace, and Brennan, 2003; Yum and Bolton, 2007). The noise from the tire-pavement contact can be classified into two categories: structural and aerodynamic (Dare, 2012). Capturing both types requires the consideration of how the tire structure vibrates during rolling and how the tire interior air cavity resonates with this vibration. In addition, sound propagation is a complex process that involves not only the source but the environment and the distance to the neighborhood. Correct modeling of the tire-pavement interaction depends on the correct modeling of the tire deformation which involves calculating the distribution of displacement and stress among the multiple materials and interfaces in the tire.

FEM has found wide use in the automotive industry. Product design, analysis and prototyping are increasingly done with this method. In this appendix, we first discuss some relevant work on the modeling of tire deformation and tire-pavement mechanical interaction. Then we review several selected publications that include the tire interior air cavity in the noise generation. Lastly, we review some publications on the coupled structural-acoustic modeling for the tire-pavement interaction and on sound propagation in the exterior field of the tire.

Tire Deformation

As the tire material is not just linear elastic, which means that the stiffness of the material is not a constant with respect to the level of loading, the tire behavior can be linear or nonlinear under different boundary conditions.

First, we introduce two studies that used linear elastic models for the tire and the pavement. In the first study, how the loading is applied to the tire was investigated. A predefined vertical load was gradually applied from the tire axle then to the rim (Wang and Roque, 2011a;2011b). Observations on the contact stress distribution at the pavement was made. The second study included tire tread patterns and improved the prediction of the tire footprint on the pavement (Moazami et al., 2011). In addition, in this study, the pavement was modeled as layers of linear elastic materials.

There are other studies that attempted to confirm the influence of the thickness of the pavement on the contact area between the tire and the pavement. One such study is (Hernandez et al., 2016), in which the authors defined thin and thick pavements as three layers: asphalt concrete, granular base, and subgrade. As linear models for the tire might not be sensitive enough to the pavement thickness, the authors used hyperelastic models which is a common nonlinear elastic family for the tire. To model the pavement, they used linear models and added linear elastic springs on its bottom and side faces. Between the thin and thick pavement that they tested; their results showed that the highest change was around 3% of the contact area when the elastic moduli for these pavements were given at their lowest values.

Truck tires are also a focus in the literature due to their complexity and economic value. To overcome the computation cost, some research adopted the strategy of sub-modeling which assumes symmetric or periodic boundary conditions. A quarter-vehicle model was created to anticipate not only the tire responses but also the sprung mass responses to the irregular road surface input (Chae, 2006). In their modeling, the vertical displacement of the tire spindle was measured. There are the longitudinal, lateral and vertical contact forces; vertical moment and overturning moment applied at the spindle during rolling and the ditch runs (Figure B.1).

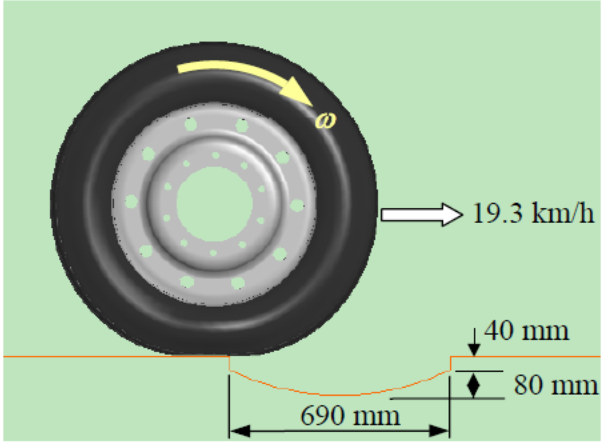

Figure B.1: Initial tire position and ditch dimension (Figure created by Chae, S. (2006). Nonlinear finite element modeling and analysis of a truck tire, page 125).

Tire-pavement Interaction

The modeling of the tire-pavement interaction using FEM over the past decades is comprehensively surveyed in (Ghoreishy, 2008). The report focused on the different techniques of FEM for a rolling tire in contact with the pavement. The pavement is modeled as either a rigid surface or a deformable body. The typical framework, Arbitrary Lagrangian and Eulerian, that enables the coupling of solids and fluids is reviewed in this survey. The Lagrangian formulation is for solid deformation (tire and pavement) and the Eulerian formulation is for fluid flow (air). Some of the publications surveyed focus on steady-state rolling (Kennedy et al., 1987; Futamura et al., 2004; Lin et al., 2004; Han et al., 2004) and some on transient dynamic responses (Kamoulakos et al., 1998; Liu et al., 2003, 2007; Brinkmeier et al., 2007). Characterizing the tire footprint on the pavement was achieved in six articles that were included in the survey. Discussing the roughness of the pavement surface was seen in five articles. Furthermore, the author documented successful commercial FEM packages such as SMITH, M, ANSYS and MSC that have been used for reliable tire-pavement simulations.

In particular, a static three-solid-truck-rib-tire model was constructed in (Wang, 2009). The author applied the Lagrangian formulation and used a commercial finite element software to evaluate the stress distribution of the contacting surface on the pavement. The work was restricted to radial truck tire models and static loading condition. In this report, the induced stresses in the tires by the pavement are studied. These stresses describe the normal and shearing directions. Analyzing each type of stress enables the understanding of the different tire motions in the rolling, lateral and loading directions. Furthermore, an air-inflated 3-D tire model was constructed with the structure of polymers and reinforcements in (Wang, 2011). The author applied the Arbitrary Lagrangian-Eulerian formulation to simulate the steady-state rolling and demonstrated the capability of their modeling to differentiate stress distributions in the tread of the tire while varying the loading conditions.

Tire Interior Air Cavity

The tire interior air cavity is an important component of the tire. The tire cavity noise is generated by the phenomenon of vibrating air inside the tire. In this section, we have reviewed the papers (Richards 1991; Molisani et al., 2003; Mohamed and Wang 2015), which analyzed the mode and mode shapes of the tire with the interior air cavity to evaluate the acoustic response of this cavity. These studies applied FEM and conducted experiments to verify that the air cavity inside the tires also influenced the creation of tire-pavement noise.

Furthermore, both FEM modeling and laboratory experiments were conducted to evaluate the impact of the interior air cavity structure (Mohamed and Wang, 2015). The authors implemented a cavity model with a tread plate that was assumed to be flexible and an additional sidewall that was assumed to be rigid. Then the resonating effect by the tire interior air cavity was added to the wave equation that solved for the modal responses of the tire. By comparing the numerical results with a moving impact test on a tire, the study showed that the rim material could be adjusted to reduce the sound pressure level of structure-borne noise, which was caused by resonating with the tire cavity.

Lastly, a half of the tire was simulated in the finite element model to save the computational cost and to analyze the structural-acoustic coupling effect (Richards, 1991). The acoustic resonance of the tire interior air cavity was noted to be important (Molisani et al., 2003). The authors found the analytical solution of the modal analysis for both the tire structure and the tire interior air cavity. The tire was modeled as an annular cylindrical shell where only the outside shell was flexible. The tire sidewalls and wheel were set as rigid. The study then compared the simulated mode (frequency) and amplitude of the mode shape response with and without acoustic coupling of the tire interior air cavity. These authors also concluded that the acoustic resonance of the tire interior air cavity needs to be included in the analysis of tire-pavement noise.

Coupled Structural-acoustic Modeling for Tire-pavement Noise

We have reviewed twenty three papers on the coupled structural-acoustic modeling for the tire-pavement noise. Some research results focus on the novel models to capture nonlinear behavior in the tire-pavement interaction and some on the sound field generated around the tire. Not all research results include validations against experimental measurements. Only a few studies focus on the influence of the geometry of the pavement surface, e.g., Li (2018).

Sound propagation away from the tire is also a topic that we have surveyed, and those research results are summarized in the next section. In particular, consideration of both the structural-acoustic modeling of the interior air cavity and the tire structure, and the propagation of the tire noise in the exterior field was achieved in (Kruntcheva, 2006).

One of the earlier modeling efforts included estimating sound intensity level and pressure for a stationary tire under a point force excitation. This study first generated the velocity field on the tire. Modal analysis was conducted on the FEM results of the excited tire on the pavement. Using the modes and mode shapes of the vibrating tire, a sound field around the tire was created using a mathematical formulation, i.e., Helmholtz-Kirchhoff formulation. This study further demonstrated that the far field sound pressure levels were in close agreement with experimental measurement taken in an anechoic chamber (Wright and Koopmann, 1986).

Advances in the theoretical development for the finite element method solidified the use of Arbitrary Lagrangian-Eulerian formulation that originated in the 1970s on coupled physics analysis on solids and fluids. The decrease in the computation cost from using this method is also noted. Consequently, this method has been incorporated into commercial tools such as SIMULIA (SMITH, M, 2016). We list here two research products that have used this method. In the first one, 3-D tread patterns were first added to a rolling tire that was modeled as in steady-state in FEM. Then a sound field was modeled as an ideal homogeneous fluid medium with small-amplitude waves. This study also verified the modeling results against a modal measurement test and found small differences (Tong et al., 2013). The second research product also modeled the rolling tire and transferred the tire vibration data to the Eulerian mesh of the tire. Comparison between the measurements and simulation results showed that their approach provided reasonable predications of the noise of the rolling tire (Wei et al., 2016).

Lastly, we note that including the tire interior cavity has an effect on the frequency range detected near the tire. One research product reported that some tire modeling for simulating structure-borne noise was only valid up to 200Hz, which was limited by the lack of the interior air cavity modes, the wheel center area and the tire/rim interface (Beniguel et al., 2012). These researchers proposed a new model containing the mechanical behavior of the tire, the wheel, and the interior air cavity and found the structure-borne noise up to 400 Hz.

Sound Propagation in Exterior Field

As we mentioned earlier, some researchers concentrated on the sound propagation in the exterior field (Wright and Koopmann, 1986; De Roo and Gerretsen et al., 2000; Brinkmeier et al., 2004, 2008; Hong et al., 2005; Tong et al., 2013; Yang et al., 2013; Wei et al., 2016). Some of them noted the large Eddy flow near the vibrating tire during rolling.

For simulating the sound propagation in the exterior airfield of the tire, the modeling method can be grouped into three types: wave, energy, and geometric acoustic (Crocker, 2007). The wave approach uses FEM or finite difference method to solve the wave equation for a small simple enclosed space with well-defined boundary conditions (Richard, 1991; Takagi and Takanari, 1991; Brinkmeier et al., 2008; Wang, 2011). The energy method uses the statistical method based on the measured data to predict the noise intensity (Beckenbauer et al., 2008). Lastly, the geometric acoustic method applies the ray-tracing method to simulate the reflection and diffraction of the sound propagation (Chung, 2002; Wilcox, 2006; Seo et al., 2008; O'Boy and Dowling, 2009). Most of the current tire-pavement noise generation models use one or two of the models we have described above.

A method using FEM to simulate the tire rolling tire-pavement interaction and the Large eddy turbulence model for the near-field sound propagation was proposed in (Yang et al., 2013). A tire-pavement intersection sub-model and a noise propagation sub-model coupled with a fluid-structure interface were included (Figure B.2). For the tire-pavement interaction sub-model, the tire was smooth without the tread. The simulated result was validated against experimental data. For the noise transmission sub-model, the large eddy simulation was used to simulate the sound propagation in the airfield near the noise source, where the airfield was modeled by an Arbitrary Lagrangian-Eulerian formulation. Lastly, the equilibrium condition of displacement and stress was fulfilled to combine the sound generation and propagation.

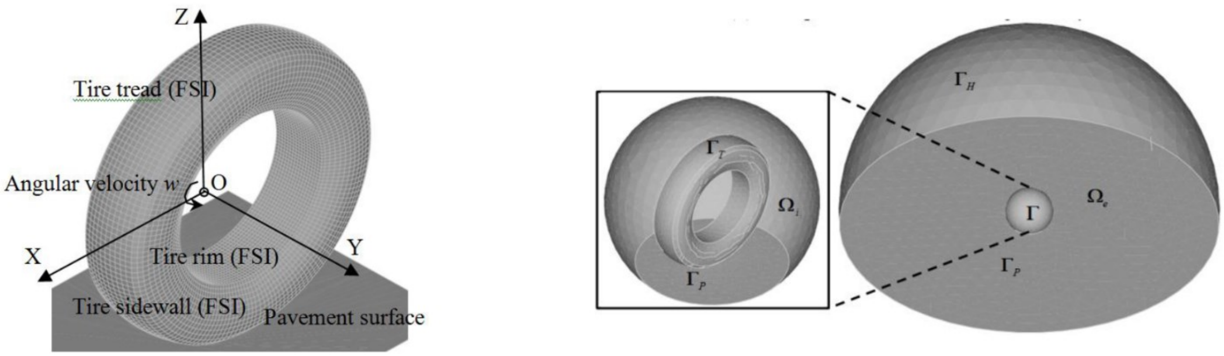

Figure B.2: Tire-pavement interaction sub-model and sound propagation sub-model (Figure created by Yang et al. (2013). In Advanced Materials Research (Vol. 723, pp. 105-112). Trans Tech Publications, page 2).

Recently, a novel method combined Boundary Element Analysis (BEA) and Energy Boundary Element Formulation (EBEF) to obtain the acoustic sound pressure of a vehicle (Hong et al., 2005). As the analytic frequency increased, the number of elements required in the model of the vehicle increased for BEA. Due to the limitation of the resolution for the model, BEA was applied for the computation in the 1/3 octave bands below 500 Hz and EBEF was applied for 500 Hz to 2000 HZ. They applied the acoustic detection range prediction model to evaluate the corresponding detectable distance between the vehicle and the location of the specific sound pressure level. As shown in Figure B.3, the left image shows the boundary element modeling, the middle image shows the field point surface applied for acoustic sound pressure computation and the right image shows the acoustic sound pressure level evaluation for 160 Hz in the 1/3 octave band.

Figure B.3: Acoustic result from one vehicle (Figure created by Hong et al. (2005). A Computational Approach for Evaluating the Acoustic Detection of a Military Vehicle (No. 2005-01-2337). SAE Technical Paper, page 4).

In conclusion, our review on recent advances of modeling tire-pavement interaction that includes both mechanical and acoustic behaviors using FEM indicates vast applications in research and industrialization. As the computation requires complex mathematical models and sophisticated numerical schemes, the cost can still be a limitation.